ΕΘΝΙΚΟ ΚΑΙ ΚΑΠΟΔΙΣΤΡΙΑΚΟ ΠΑΝΕΠΙΣΤΗΜΙΟ ΑΘΗΝΩΝ

ΣΧΟΛΗ ΘΕΤΙΚΩΝ ΕΠΙΣΤΗΜΩΝ

ΤΜΗΜΑ ΧΗΜΕΙΑΣ

ΔΙΔΑΚΤΟΡΙΚΗ ΔΙΑΤΡΙΒΗ

Development of nanocomposite materials for hydrogen storage

FILIPPO PERU
ΧΗΜΙΚΟΣ

ΑΘΗΝΑ

ΔΕΚΕΜΒΡΙΟΣ 2022

ΔΙΔΑΚΤΟΡΙΚΗ ΔΙΑΤΡΙΒΗ

Development of nanocomposite materials for hydrogen storage

FILIPPO PERU

Α.Μ.: 001415

ΕΠΙΒΛΕΠΩΝ ΚΑΘΗΓΗΤΗΣ:

ΠΑΝΑΓΙΩΤΗΣ ΚΥΡΙΤΣΗΣ, Καθηγητής ΕΚΠΑ

ΤΡΙΜΕΛΗΣ ΕΠΙΤΡΟΠΗ ΠΑΡΑΚΟΛΟΥΘΗΣΗΣ:

ΠΑΝΑΓΙΩΤΗΣ ΚΥΡΙΤΣΗΣ, Καθηγητής ΕΚΠΑ

ΧΡΙΣΤΙΑΝΑ ΜΗΤΣΟΠΟΥΛΟΥ, Καθηγήτρια ΕΚΠΑ

ΘΕΟΔΩΡΟΣ ΣΤΕΡΙΩΤΗΣ, Διευθυντής Ερευνών ΕΚΕΦΕ «Δημόκριτος»

ΕΠΤΑΜΕΛΗΣ ΕΞΕΤΑΣΤΙΚΗ ΕΠΙΤΡΟΠΗ

ΠΑΝΑΓΙΩΤΗΣ ΚΥΡΙΤΣΗΣ, Καθ. ΕΚΠΑ

ΧΡΙΣΤΙΑΝΑ ΜΗΤΣΟΠΟΥΛΟΥ, Καθ. ΕΚΠΑ

ΘΕΟΔΩΡΟΣ ΣΤΕΡΙΩΤΗΣ, Διευθ. Ερευνών ΕΚΕΦΕ «Δ»

ΙΩΑΝΝΗΣ ΠΑΠΑΕΥΣΤΑΘΙΟΥ, Καθ. ΕΚΠΑ

ΕΛΕΝΗ ΕΥΘΥΜΙΑΔΟΥ, Επικ. Καθ. ΕΚΠΑ

ΚΩΝΣΤΑΝΤΙΝΟΣ ΜΕΘΕΝΙΤΗΣ, Αναπλ. Καθ. ΕΚΠΑ

ΓΕΩΡΓΙΑ ΧΑΡΑΛΑΜΠΟΠΟΥΛΟΥ, Διευθ. Ερευνών ΕΚΕΦΕ «Δ»

ΗΜΕΡΟΜΗΝΙΑ ΕΞΕΤΑΣΗΣ 15/12/2022

ΠΕΡΙΛΗΨΗ

Τα βοροϋδρίδια παρουσιάζουν ιδιαίτερο ενδιαφέρον για διεργασίες αποθήκευσης υδρογόνου σε χαμηλές πιέσεις, λόγω της πολύ υψηλής περιεκτικότητας σε υδρογόνο. Ωστόσο, η ιδιαίτερη σταθερότητά τους και οι υψηλές θερμοκρασίες που απαιτούνται για την διάσπασή τους δεν ευνοούν την πρακτική τους εφαρμογή. Μια ενδιαφέρουσα προσέγγιση για την κατάλληλη τροποποίηση των θερμοδυναμικών ιδιοτήτων τους σχετίζεται με την μορφοποίησή τους σε σωματίδια νανοκλίμακας μέσω περιορισμού σε νανοπόρους. Στόχος της παρούσας διατριβής ήταν η μελέτη των ιδιοτήτων αποθήκευσης-αποδέσμευσης υδρογόνου ευτηκτικών μιγμάτων βοροϋδριδίων, όπως $LiBH_4$ – $NaBH_4$ (LiNa) και $LiBH_4$ – KBH_4 (LiK), μετά την εισαγωγή τους (μέσω διήθησης τήγματος) στους πόρους μεσοπορωδών υλικών ανθρακικής βάσης. Παρατηρήθηκε ότι και για τα δύο ευτηκτικά μίγματα, η εισαγωγή τους στους πόρους άνθρακα τύπου CMK-3 και αερογέλης άνθρακα (CA-20) με διάμετρο 5 και 25 nm, αντίστοιχα, βελτιώνει την κινητική ενώ επιτρέπει και τη μερική αντιστρεψιμότητα της αντίδρασης αφυδρογόνωσης / υδρογόνωσης μετά από 5 κύκλους. Ενώ οι αντιδράσεις αφυδρογόνωσης των σύμπλοκων υδριδίων είναι μη αναστρέψιμες, τα σύνθετα συστήματα άνθρακα/βοροϋδριδίων παρουσιάζουν σταθερή αναστρέψιμη πρόσληψη H_2 περίπου 3.5-4 wt% για τα σύνθετα LiNa / CMK-3 και CA-20 και περίπου 3 wt% H_2 για τα αντίστοιχα υλικά με LiK. Η αντίστοιχη μελέτη σύνθετων υλικών με μη πορώδεις δίσκους άνθρακα (Carbon Disks, CD), επίσης έδειξε βελτίωση στις ιδιότητες απελευθέρωσης υδρογόνου από τα βοροϋδρίδια, υποδηλώνοντας ότι η επιφάνεια του άνθρακα μπορεί να δράσει καταλυτικά και να βοηθήσει την διάσπαση των βοροϋδριδίων. Ωστόσο, ο νανοπεριορισμός στους πόρους φαίνεται να παίζει θεμελιώδη ρόλο στην αντιστρεπτότητα της αντίδρασης υδρογόνωσης, τουλάχιστον για την περίπτωση του μείγματος $LiBH_4$ – KBH_4. Η συμπεριφορά αυτή μπορεί να σχετίζεται με έναν συνδυασμό φαινομένων όπως με την καταλυτική δράση της επιφάνειας του άνθρακα, τη νανοδιάσταση των σωματιδίων βοροϋδριδίου και/ή τον περιορισμό μη αντιστρέψιμων πλευρικών αντιδράσεων.

ΘΕΜΑΤΙΚΗ ΠΕΡΙΟΧΗ: Αποθήκευση υδρογόνου με χρήση υλικών

ΛΕΞΕΙΣ ΚΛΕΙΔΙΑ: Αποθήκευση υδρογόνου, μεσοπορώδη υλικά, νανοπεριορισμός, σύμπλοκα υδρίδια, βοροϋδρίδια, ευτηκτικά μίγματα

ABSTRACT

Borohydrides are considered good candidates for low-pressure solid state hydrogen storage, as they have very high hydrogen content. However their high stability and decomposition temperatures hinder their practical use. An appealing approach for adjusting their thermodynamic properties is nano-sizing by confinement in nanometer-sized pores. The aim of this thesis has been to study the hydrogen storage-release properties of eutectic borohydride mixtures such as $LiBH_4$ – $NaBH_4$ (LiNa) and $LiBH_4$ – KBH_4 (LiK), after their incorporation (through melt infiltration) in mesoporous carbonaceous materials. It has been shown that the confinement of the borohydride mixtures into 5 and 25 nm diameter pores of a CMK-3 type carbon and a carbon aerogel (CA-20), respectively, improves the kinetics, also providing a partial reversibility of the dehydrogenation / rehydrogenation reaction for both eutectic mixtures after 5 cycles. While the dehydrogenation reactions of the bulk complex hydrides are irreversible, the nanoconfined systems exhibit a consistent reversible uptake of about 3.5-4 wt% H_2 for the LiNa / CMK-3 and CA-20 composites and about 3 wt% H_2 for the LiK ones. The same synthetic procedure was also followed to obtain composite materials with non-porous carbon disks (CD) and kinetic improvements in the hydrogen release properties of the borohydrides were also observed. These findings in the absence of porosity imply that the carbon surface may act catalytically and assist the decomposition of the borohydrides. However, the pore nanoconfinement seems to play a fundamental role in the reversibility of the hydrogenation reaction, at least for the case of the $LiBH_4$ – KBH_4 mixture. Overall, this thesis revealed that the increased reversibility and improved kinetics may be related to a combination of several phenomena such as the catalytic action of the carbon surface, the nano-sizing of the borohydride particles, and/or the abatement of irreversible side-reactions.

SUBJECT AREA: Material-based hydrogen storage

KEYWORDS: Hydrogen storage, mesoporous materials, nanoconfinement, complex hydrides, borohydrides, eutectic mixtures

TABLE OF CONTENTS

TABLE OF IMAGES

CHAPTER 1
INTRODUCTION

1.1 Today's energy landscape

Energy is essential for economic and social development as well as improvement of the quality of life in all countries.[1] The global energy consumption has doubled in the past forty years. Even though there have been changes in the energy mix adopted during the last 100 years, the use of all energy sources is still growing (Figure 1). The introduction and the widespread of internal combustion engines for transport increased the share of hydrocarbons over solid fuels like coal and wood. Especially the second half of the XX century, experienced a boom of the energy consumption, with the first attempts to diversify the energy sources. Since fossil fuels are not renewable, it can be predicted that by the next decades, mankind will face challenges related to the sustainability of conventional oil production, a peak of gas production and in parallel, increased restrictions on coal production and use, due to environmental regulations. In this context, hydropower and nuclear power have started to grow and played an important role among the energy sources in the last decade of the XX century while renewable sources (wind, solar hydrothermal, tidal power, biomass etc.) began to gain influence in the global overview as well.[2]

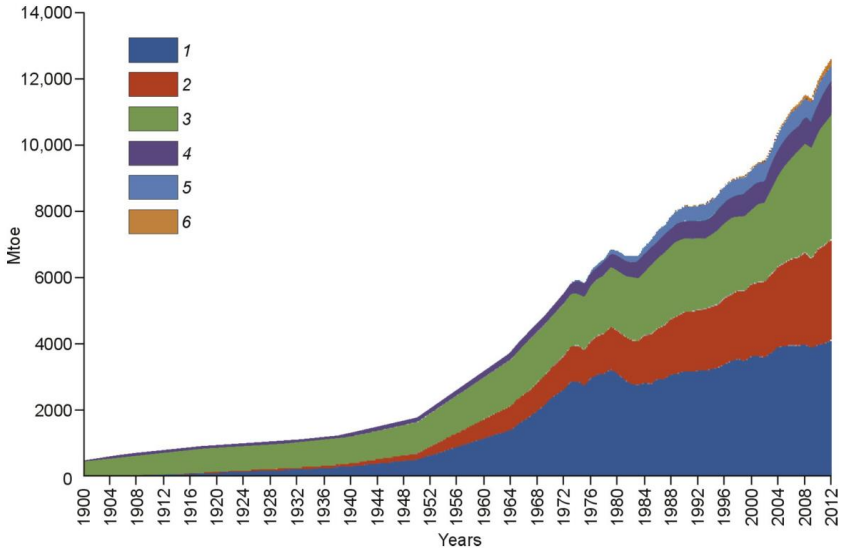

Figure 1: Global production of energy sources in 1900-2012

1, Oil; 2, Natural gas;3, Coal; 4, Hydroelectric; 5, Nuclear power; 6, Others.[2]

In 2013 it has been estimated that 19.1% of global energy consumption was provided by renewable sources[3] and according to optimistic projection models, the 65% of the total energy needs could be covered by renewable sources by 2100.[4] The increase of attention on renewable energy sources can be attributed to several factors such as the limited amount of hydrocarbons, the volatility of oil prices, the energetic dependence from other countries, but also the environmental and health consequences of pollution due to fossil fuels use.[5] In fact, the nature of the renewable sources makes them infinite and practically limitless. For instance, the solar radiation that reaches the earth's surface in one year, provides more than 10.000 times the world's yearly energy needs.[6] Moreover, the existence of different kinds of renewable sources ensures the possibility to build up a diversification in the energy production matrix, reducing situations of political dependence and energy-related instability. But probably, one of the major driving forces behind the growing of renewable energies demand, is related to the awareness of the necessity of a climate change mitigation strategy coupled with reduction of polluting combustion products.[7] On the other hand, in spite of any possible progress on the exploitation of renewable sources, there is always an inherent problem, i.e. renewable energy is most of the times not constant. This issue is particularly important in weather related sources, that despite the modern methods of forecasting, they are still mostly unpredictable.[8–10] In order to counterbalance the fluctuations of the power production coming from different types of renewable resources, it is necessary to store the energetic surplus, in order to use it when needed.[11] Chemical accumulators in the form of batteries are often used to regulate the power supply. In this context, hydrogen has started to emerge, as a promising and flexible medium for energy storage, since it can be directly produced by renewable sources (through electrolysis), stored and converted to electricity (with fuel cells). However, the application and development of this energy carrier requires the optimization of the current technologies for hydrogen production, storage and use, as well as their integration in the everyday energy landscape.[10]

In general, the use of energy carriers is particularly important in the transportation sector. Nowadays, transportation comprises nearly a quarter of the primary energy demands and the global CO_2 emissions, while road transport plays a key role. Projections foresee a ~20% increase of global energy demand and greenhouse emissions related to road transport until 2040. This is also due to the fact that oil is the main fuel source and its use covers about 95% of the transportation energy demands while it is clearly necessary to reach a stage where road transport will not be any more

dependent on fossil fuels. A first option could be based on biofuels, the use of which could reduce the greenhouse gas emissions and the supply security. Moreover, the introduction of biofuels would require limited changes in infrastructure, vehicle cost and performance. However, the production of biofuels is connected with several problems related to the environmental sustainability upon mass production, in particular the use of large amount of water and extended land areas, the need of using fertilizers and pesticides, the risks for biodiversity as well as the competition with food production.[12] The use of biofuels may decrease CO_2 emissions, however the road towards zero emissions involves alternatives based on electricity rather than combustion. The options could comprise pure battery electric vehicles, hydrogen fuel cell vehicles, as well as hybrid vehicles powered by both (batteries and hydrogen).[12] In these cases the emissions would be limited to just water for the hydrogen vehicles.

Such a hydrogen based zero-emission strategy (production of hydrogen by renewable sources, hydrogen storage and hydrogen conversion to electricity when needed) could ideally be expanded to embrace all the renewable systems. In this respect, hydrogen could be the keystone of a society which is unconstraint from fossil fuels availability, but can be supplied by a theoretically infinite amount of energy.

1.2 Hydrogen Economy

The challenge to find alternative fuels to minimize energy supply limitations and mitigate the environmental impact of fossil fuel combustion, has led to the consideration of several more eco-friendly fuels like reformulated gasoline or diesel, methanol, ethanol, dimethyl ether and of course hydrogen. The latter is certainly the best option, both from the point of view of emissions and the energy supply. Hydrogen, like electricity, is actually an energy carrier. This means that it can be obtained from primary energy sources that may include fossil fuels (gas, coal, and oil), biomass (vegetable residues and waste or energy crops), nuclear power but also from renewable sources like sunlight and wind power.[13] Consequently, the energy stored in hydrogen can be delivered by oxidation, i.e. through combustion or electrochemically in fuel cells. When hydrogen is produced by e.g. fossil fuels (grey hydrogen) the problem persists and the amount of energy available will be still limited to the fossil stocks. On the other hand, if hydrogen is produced by renewable sources e.g. through water splitting (green hydrogen), the fuel production and use would be associated with near zero emissions of air pollutants (nitrogen oxides, carbon monoxide, sulphur oxides, volatile hydrocarbons,

and particulates) or greenhouse gases since water is the only product.[13] “Hydrogen Economy” is based on the above zero emission energy production strategy. In this ideal economy, electricity from renewable sources should be used to obtain hydrogen from water via electrolysis and then stored. Finally, the energy temporarily stored in form of hydrogen can be obtained by the reaction of hydrogen with oxygen, to produce water by means of an internal combustion engine or a burner but also with the aid of fuel cells. The concept of using renewable energy to produce hydrogen and then obtain the energy back with the production of water is called “hydrogen cycle” (Figure 2).[14] The solar intensity at the top of the atmosphere is 1360.8 ± 0.5 W/m^2 (minimum)[15], while ~50 % of this energy reaches the Earth surface and since there is no energy during night, the remaining value has to be divided by half. Based on the above, under the assumption of 10% efficient conversion from photovoltaic cells, a surface area of 500000 km^2 would be enough to cover the current world energy demand. [14]

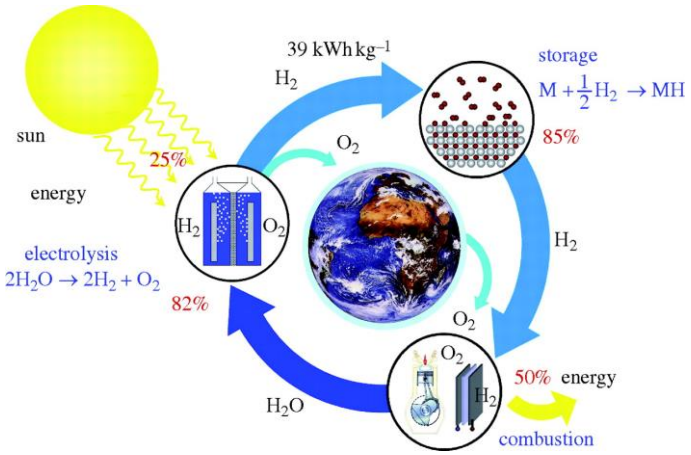

Figure 2: Schematic representation of the hydrogen cycle. The sunlight energy is converted to electricity and used to produce hydrogen by water splitting. The hydrogen obtained is stored and when energy is needed, it is possible to get it with combustion engines/burners or fuel cells by reaction with oxygen.[14]

CHAPTER 2
HYDROGEN

2.1 The element and molecule

Hydrogen (H) is the first and simplest element, consisting of a proton and an electron; its atomic electron configuration is $1s^1$ and is in the first period and first group of the periodic table of elements. In the first period, besides hydrogen there is only helium. While helium is a totally inert noble gas, hydrogen is very reactive and its properties cannot be directly correlated with any of the main element groups of the periodic table; Hydrogen structure is in some ways similar to the metals of the group I, (alkali metals), and like them has only one electron in the outer shell. However, the alkali metals have the tendency to lose their electron and become electronically stable as M^+, while hydrogen is more likely to pair the lone electron to form a covalent bond, similarly to halogens of group 17.

It is possible to find the element in nature in the form of three isotopes. The most abundant (99.985 %) isotope is Protium (^1H) and has a one proton nucleus. Deuterium (0.015 % of total hydrogen in nature) has a nucleus with one proton and one neutron. The use of deuterium is common in chemistry, in particularly as a tracer, in neutron scattering, NMR as well as in UV and IR methodologies. Deuterium as oxide (heavy water) is also used in ton quantities as moderator in nuclear reactors. The least abundant form of hydrogen is the Tritium (T). It is a radioactive isotope and decay with β-particles emission, with a half-life of 12.33 years. Tritium occurs naturally in very small amounts in the order of 10^{-17} %, while it is formed continuously in the upper atmosphere by nuclear reactions induced by cosmic rays. Commonly it is produced artificially in nuclear reactors from ^6Li and used mostly for studies of nuclear fusion.[16–18]

Hydrogen is the most abundant element in the universe. Some estimations mention that hydrogen is 73 wt% of all matter, while helium is around 25 wt% and ~2 wt% comprises all the other elements.[19] However, the presence of H_2 on the Earth atmosphere is very small, since the earth's gravitational field cannot retain such a light element. On Earth, hydrogen is found in molecules (mainly H_2O) bonded to other elements.

Molecular hydrogen is a diatomic molecule with a strong covalent bond between two hydrogen atoms. It is a colourless and odourless gas, the lightest one, with a boiling point of -252.88 °C (20.27 K) and almost no solubility in water. Hydrogen has low reactivity under normal conditions due to the covalent bond strength. For this reason,

many reactions that are slow at low temperatures, require a high amount of energy or catalysts to break the H-H bond and obtain highly reactive single hydrogen atoms. The dissociation of the molecule is highly endothermic, with a bond dissociation energy of 435.9 kJ/mol. The bond can be broken by transition metal catalysts that are able to decrease the bond breaking activation energies. Other more energy demanding ways to split the H_2 molecule and obtain atomic hydrogen include high temperature treatment in an electric arc or under ultraviolet light. Atomic hydrogen is extremely reactive with a lifetime shorter than 0.5 seconds, after which it reacts with other hydrogen atoms in a strongly exothermic reaction to H_2.

Under the appropriate conditions hydrogen can react directly with most elements. In air hydrogen can burn with oxygen to give water. The great energy released is often used in oxy-hydrogen flames, which may reach almost 3000 °C; for this reason, hydrogen is used in metal welding and cutting processes.

$$2H_2 + O_2 \rightarrow 2H_2O \qquad \Delta H = -485 \text{ kJ/mol}$$

Hydrogen is highly reactive also with halogens; for instance, it reacts violently at low temperatures with fluorine. The reaction with chlorine is slow in the dark, but is photocatalyzed and becomes faster under light, while it is explosive under sunlight. The direct combination of the element gives the relative hydracids. H_2 reacts with several metals often under high pressure and temperature to afford metal hydrides. As already mentioned, transition metals react with hydrogen and are commonly used as catalysts to lower the activation energies in common industrial reactions, for instance in the Haber-Bosch process for the production of NH_3 from reaction of H_2 with N_2 that needs high temperatures, pressure of ~200 atm and an iron catalyst.[20,21]

Another important example where transition metals are used as catalysts is the addition of hydrogen to a double bond in organic compounds. Large amounts of hydrogen are commonly used for the industrial hydrogenation of vegetable oils. Unsaturated fatty acids are hydrogenated with H_2 (with Ni, Pd or Pt catalysts)[18,22] in order to obtain their saturated version with higher melting points. A similarly important catalysed H_2 reaction is the production of methanol from carbon monoxide (Cu/Zn)[18,23].

In the previously reported examples, but also in most of the hydrogen reactions, the chemistry of hydrogen is influenced mainly by three electronic processes:

Electron loss: when a hydrogen atom loses its 1s only electron to become a proton (H^+). Cationic hydrogen due to its charge and its small size ($8.4*10^{-14}$ cm)[24] has a unique reactivity and the ability to distort the electronic clouds of nearby atoms.

Electron gain: a hydrogen atom with $1s^2$ configuration (anionic form) and becomes H^-, commonly referred to as hydride. H^- is found only in salt form, coupled with more electropositive metals.

Electrons sharing: hydrogen shares its electron to build a covalent bond with another atom. This is the most common phenomenon that happens between hydrogen and other species, e.g. in countless carbon compounds.[16]

Atomic hydrogen can also make metallic bonds with metals and alloys (interstitial hydrides).

In hydrogen containing compounds, the molecular properties strongly depend on these electronic relationships of hydrogen with other species, and will be highlighted in the next paragraphs when different high-content hydrogen compounds will be presented.

2.2 Hydrogen production

Nowadays a hydrogen production of about 55 million tons per year is estimated, while the demand increases every year. Hydrogen is produced through several routes, among which the steam reforming of natural gas (steam methane reforming, SMR) is the most common and covers around 48% of the global hydrogen production. It has to be noted that the production of hydrogen from methane is also one of most important greenhouse gas emitting processes. Beyond SMR, approximately 30% of the global hydrogen production comes from reforming of oil and naphtha in the context of industrial refinery processes, 18% from coal gasification, 3.9% from water electrolysis and 0.1% from other sources[25] for instance the chlor-alkali process, an industrial process to produce chlorine and sodium hydroxide by electrolysis, with large amounts of hydrogen as a reaction by-product.

2.3 Hydrogen applications: combustion and fuel cells

The simplest way to use the chemical energy carried by H_2 is to burn it. The explosive reaction of hydrogen oxidation can be controlled and used for instance in internal combustion engines more or less like hydrocarbons. However, hydrogen has larger

molar volume and energy output than gasoline, allowing lower fuel to air ratios and complete fuel combustion, increasing thus the overall efficiency. In addition, the emissions of pollutants are minimized (with the exception of low levels of NO_x). A well performing combustion engine can reach an energy conversion of about 45%; a fuel cell however has an average efficiency between 40 and 60%, with an ideal reachable efficiency of 90% in combined heat and power production.[26–28]

Fuel cells are devices for the direct conversion of chemical energy to electrical energy by the combination of a gaseous fuel (hydrogen) with an oxidant (oxygen) through electrodes and an ion conducting electrolyte. The fuel cell, unlike a common electrochemical cell, is not depleted but continues producing electricity as long as fuel is provided.[28] The fuel cell has two main parts: the anode, where the H_2 oxidation takes place and H^+ are generated and the cathode, where O_2 is reduced with consequent H_2O formation. The two electrodes are connected through an electrolyte that allows the selective transport of protons. Several types of fuel cells have been developed during the last decades. The types are characterized by different electrolytes, different electrode materials and working temperatures and include:

- Molten carbonate fuel cells
- Solid oxide fuel cells
- Alkaline cells
- Phosphoric acid fuel cells
- Proton exchange membrane fuel cells

2.4 Hydrogen storage

The development of high performing technologies for the production and use of hydrogen as an energy carrier is not sufficient for a full transition to hydrogen economy; the above should always be coupled with efficient methods to store hydrogen. Currently, research is focused on the development of safe, reliable, compact and cost-effective materials and processes that can be combined with fuel cells and this is a very difficult task especially for mobile applications. Up to now, the most challenging problem is to find a hydrogen containing system with an energy density able to compete with the most common fossil fuels. The system should have large gravimetric and volumetric density, which should be coupled with fast charge/release kinetics, reversibility, near ambient working temperature and pressure and quite importantly, low cost. Current technologies

include storage of pure hydrogen as compressed gas or liquid but also “binding” of hydrogen to solid materials or liquids which can act as hydrogen carriers.[29–31]

2.4.1 Compressed hydrogen

At ambient temperature and atmospheric pressure, molecular hydrogen is a very low density gas and 1 kg of H_2 occupies a volume of 11 m^3. The most common way to reduce this volume is to compress the gas and store it in high pressure cylinders, commonly operating between 200 and 350 bar.[29,32] The volumetric energy density of hydrogen at those pressures is still too low for real-life applications, and increasing the pressure level to higher values is an alternative. During the last years cylinders which can store hydrogen at 700 bar have been tested and are actually used, but at such high pressures the consideration of new tank materials and safety issues is imminent.[33] At the moment, compressed hydrogen storage tanks are divided in four main classes: Type I, refers to all metal cylinders; Type II cylinders, are made of a metal cylinder, hoop-wrapped (periphery only) with a continuous resin-fibre layer; Type III has a non-load-bearing metal liner fully wrapped (axial-hoop) with resin-impregnated fibres; Type IV (Figure 3) refers to non-load-bearing non-metal liner fully (axially and hoop) wrapped with resin-impregnated continuous fibres. Generally the materials used for the type IV are carbon fibres, high molecular weight polymers but also glass fibres are used, allowing high pressures such as 700 bar.[34,35]

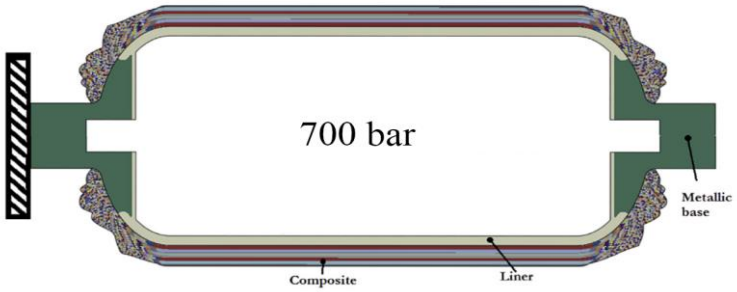

Figure 3: Type IV pressure vessel.[36]

High pressure hydrogen storage problems are not limited to the container itself, but also to the system of valves, pipelines and detectors necessary to sustain and control such drastic conditions and the gas compression process. Nowadays, hydrogen compression is carried out either mechanically or non-mechanically. Mechanical compression includes piston and piston-metal diaphragm compressors. Piston systems are electro-

mechanical, water cooled, non-lubricated and driven by a hydraulic pump. The piston-diaphragm systems use a series of diaphragms to isolate the compressed gas and the piston. However they require particular attention to the maintenance and lubrication of the components, as well as high amounts of electrical energy to operate.[37,38] Those problems are avoided with the second family of compressors, the non-mechanical ones. Generally these systems have several advantages, such as smaller size, lower costs of production, operation, and maintenance, absence of moving parts, smaller energy demand and the possibility to supply high-purity hydrogen. Non-mechanical compressors can be based on metal hydrides sorption or on electrochemical cells.

Figure 4: Prototype of a metal hydride compressor built in the framework of the ATLAS project in Hystore Tech (CY).

The operation of a metal hydride hydrogen compressor (Figure 4) is based on metal alloys that can sorb interstitially and desorb hydrogen at different temperatures. The compression needs two steps: in the first hydrogen is absorbed by the alloy (to form a metal hydride phase) at low pressure and temperature, then in a second step, by simply heating the metal hydride, the released hydrogen can reach pressures between 3 - 10 times higher. Based on this principle, a combination of different metal hydrides with ascending sorption-desorption equilibrium pressures (pressure plateaus) can be used in a multistage/cascade approach to increase the final deliverable pressure.[37–39] On the other hand, the electrochemical compressor is a device able to compress small quantities of hydrogen. The compression mechanism is based on the function of a multistage electrochemical cell: low pressure hydrogen separates into protons and

electrons at the anode and the protons are electrochemically driven across a proton exchange membrane to re-combine at the cathode producing thus hydrogen under pressure.[37]

2.4.2 Liquid Hydrogen

The second method to increase the volumetric density of hydrogen is to decrease the temperature below its critical point (33.2 K) and thus store it as liquid. The normal boiling point of H_2 is 20.28 K and at this temperature hydrogen can be stored as liquid at ambient pressure with a density of 0.071 kg/L. Hydrogen was first liquefied in 1898 by Sir James Dewar[40]. A few years later, based on the principle of the Linde–Hampson cycle for air liquefaction, the Claude cycle was developed. Hydrogen was first pre-cooled with liquid nitrogen, and then led to lower temperatures with a series of iso-enthalpic expansions exploiting the Joule-Thompson effect. A secondary helium-refrigerant can be added, but this system was never adopted for large-scale plants.[32,41,42] However, although the theoretical energy necessary to obtain liquid H_2 is 3.23 kWh/kg, the actual energy consumed is about 11-15 kWh/kg (depending on the quantity to be liquified), reaching almost half of the lower heating value of hydrogen combustion.[32] This high energy consumption, coupled with the loss of hydrogen due to thermal-leakage and consequential boil-off (typically 0.4% daily for 50m^3 tanks), renders this method suitable only for processes where high quantities of hydrogen are consumed in short periods of time, such as space applications.[32]

2.4.3 Solid state hydrogen storage

The storage of hydrogen in a solid-state material shows advantages over compressed and liquid hydrogen storage in terms of gravimetric/volumetric density, safety and energy consumption. Hydrogen can be stored in solid state by exploiting weak physical interactions with surfaces or stronger interactions that may lead to chemical bonds. A wide number of solid-state hydrogen storage materials have been proposed and are potentially promising for applications. For instance, the “physical” route involves nanoporous materials with very high surface areas (activated carbons, metal organic frameworks, etc), while chemical bonds can lead to the formation of e.g. metal or complex hydrides, amides and ammonia boranes. The most important parameters to take into account when selecting good candidate materials for hydrogen storage are the

gravimetric and volumetric storage capacities (or energy densities) but also kinetics, reversibility, scalability and certainly cost.

2.4.3.1 Physisorption

Hydrogen can be stored in molecular form (H_2) on the surface of solid materials through physical adsorption (physisorption). The adsorption of hydrogen is due to the van der Waals forces between the diatomic molecules and the atoms of the solid surface. These forces comprise a long-range weak attractive component and a short-range repulsive one. The former is attributed to the sum of Coulombic interactions (e.g. dipole-dipole, dipole-induced dipole, interactions of higher moments) and London forces, i.e. fast fluctuations of the electron density of atoms (or molecules) that create instantaneous attractive electric moments. The short-range repulsion component is due to the Pauli exclusion principle between atomic/molecular orbitals. At ambient conditions, the H_2-solid interactions are comparable to the thermal energy of gas molecules and thus H_2 adsorption is rather insignificant. In this respect, adsorption is favoured at high pressures (e.g. 100 bar) and low temperatures (usually 77 K); the need of energy-demanding cryogenic conditions is the major disadvantage of this storage method (cryoadsorption)[43,44] Since adsorption is a purely surface phenomenon, porous materials with high surface areas are required. For instance, high surface area carbons, such as activated carbons, graphene and nanotubes have been proved to be effective to store considerable amounts of hydrogen at low temperatures.[45,46]

However, none of the materials above has exhibited acceptable uptakes of hydrogen at near ambient conditions.[47] Among the high surface area materials, other alternatives such as porous polymers, zeolites and metal organic frameworks (MOFs) are currently under study for adsorptive hydrogen storage. The polymer family comprises four types of highly porous polymers: (a) hypercrosslinked polymers (HCPs), (b) polymers of intrinsic microporosity (PIMs), (c) conjugated microporous polymers (CMPs), and (d) porous aromatic frameworks (PAFs). The main advantages of these materials are their low density (they contain only or mostly light elements) the facile synthesis routes and their scalability. It is noteworthy that several resins with surface areas higher than 2000 m^2/g have been synthesized already.[48,49] The family of zeolites (crystalline aluminosilicate materials with a structural microporosity and general formula $M^{n+}_{m/n}[(SiO_2)_p(AlO_2)_m]\cdot xH_2O$) is definitely better studied. Although zeolites have initially been proposed as potential hydrogen sorbents it has been proven that the zeolitic

structures are limited to capacities below 3 wt% at 77 K and are thus currently not considered as a possible solution.[50]

Another class of crystalline materials, with very low density and high surface area are metal organic frameworks (MOFs).[51] Among MOFs there are several examples like NU-111, NU-1501-Al, NU-1103, MOF-117, UMCM-9 with very high surface areas, (>~6000 m^2/g) and adsorption capacities > 10 wt% (10.0 MPa and 77 K).[52–59] These values make MOFs maybe the most promising materials for hydrogen storage by physisorption although cryogenic operation conditions is still a drawback. Generally, physisorption involves a release of energy of around 4-10 kJ/mol of hydrogen, a value much smaller than the 50 kJ/mol per H_2 molecule which is typically released during chemisorption.[60] This aspect, coupled with the complete reversibility of the process and very fast kinetics are extremely interesting for automotive applications and in particularly for on board fuelling.

2.4.3.2 Clathrate hydrates

Clathrates hydrates or gas hydrates are ice-like inclusion structures in which water molecules are linked through hydrogen bonds to create cage structures with cavities where a large variety of molecules can be “entrapped” without any chemical bond, but only physical interactions.[61] In the 1993 Von et al. obtained the first example of clathrate hydrate of pure hydrogen. At pressures between 0.75 and 3.1 GPa at 22 °C (295 K) it was possible to create hydrogen containing water cages [62] and later, capacities of 5.3 wt% were reached on the same kind of compounds.[63] However, the high pressures necessary made this option not interesting for hydrogen storage. It was later discovered that the presence of certain “promoter” molecules (for instance THF) can help to stabilize hydrate clathrates allowing thus the formation of hydrogen containing cages at much lower pressures (60 times lower with THF)[64] while also tuning the cage size to allow higher capacities.[65,66] Other notable promoters are cyclohexanone, furan, tetrahydrothiophene and ionic promoters (belonging to the so called family of semi-clathrates of hydrogen).[67] Similarly to sorbents, clathrates show several advantages in hydrogen storage applications. Firstly, they have very low cost and are environmentally friendly, because clathrates are based mostly on water and quite low concentrations of promoter species; the hydrogen in clathrates is stored in a molecular form and the entrapped molecules can be delivered in a very fast manner by simple depressurization or with mild heating. Generally, mild temperatures and pressures are required to have

relatively high hydrogen contents and thus the method is considered a rather safe storage solution. However, clathrates have also some significant drawbacks severely hindering their application. The major problem is related to the very slow kinetics of formation that imply impractically long charging procedures. Additionally, their stability at ambient pressure and temperature conditions is low, while their capacity is rather low especially when considering the dead weight of promoters and the fact that the promoter molecules occupy cages and thus exclude hydrogen from this space.[67]

2.4.3.3 Metal hydrides

The metal-hydrogen materials have totally different characteristics and chemical behaviour depending on the position of the metal in the periodic table. Three main classes of compounds can be distinguished:

1. Metallic hydrides, with interstitial hydrogen
2. Salt-like hydrides, with ionic interactions among species
3. Molecular hydrides, with covalent bonds

Hydrogen directly reacts with a large number of transition metals generating metallic hydrides (MH_n type), often deviating from the ideal stoichiometry. In these compounds, hydrogen atoms may carry a partial negative charge, depending on the metal of the lattice. Due to its small atomic size hydrogen atoms can occupy the octahedral or tetrahedral interstices between the metal atoms of the lattice, and for this reason these compounds are also known as interstitial hydrides (Figure 5).[32]

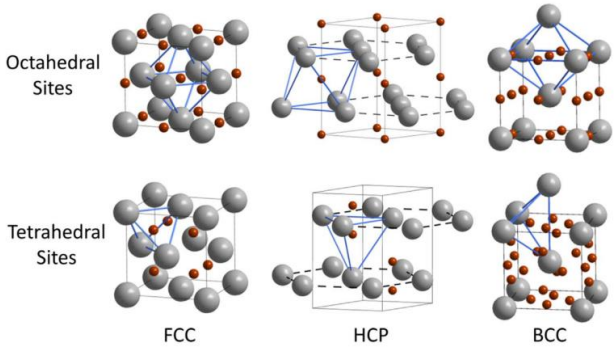

Figure 5: Hydrogen occupying octahedral and tetrahedral sites in interstitial hydrides.[68]

The storage of hydrogen in metallic hydrides is interesting due to the presence of many systems that are able to work at near ambient temperature and to release hydrogen simply by decreasing the external hydrogen pressure or triggering the desorption with a moderate increase of the temperature.[69] However, there are still several issues associated to metal hydrides, like their weight penalty leading to low hydrogen storage capacity.[70] Much interest is focused on intermetallic compounds due to the several hydrogen-related applications of these alloys, including hydrogen storage but also batteries, hydrogen purification systems, catalysts, sensors, hydrogen compressors.[39,71] The most common intermetallic compounds are based on the stoichiometric compositions AB_5, AB, AB_2, AB_3 and A_2B. However, the room temperature reversible hydrides suffer from low gravimetric hydrogen density, which is limited to 3 wt% maximum.[72]

The AB_5 type alloys have been studied with a wide range of different compounds due to the easy substitution of the elements in the A and B sites. The A site usually is occupied by rare earth metals, calcium, zirconium or yttrium. The B site hosts mostly d-metals like nickel, copper, cobalt, iron or platinum. A notable compound of this type is $LaNi_5$, known for its fast kinetics and ability to exchange reversibly hydrogen. These systems can theoretically exchange a 1.5 wt% hydrogen at 100°C,[73] which is not enough for applications. However, better performances as well as lower cost can be achieved by partially substituting lanthanum and nickel with other metals.[74] The AB type alloys have a cubic structure and are also well studied. The most famous alloy of this kind is TiFe, with much lower cost compared to $LaNi_5$ and higher hydrogen capacities (still lower than 2 wt%). On the other hand, AB alloys require intense activation conditions and have in general high equilibrium pressures. In this specific case, the equilibrium is between the solid phase of metal and interstitial hydrogen (α-phase) and the metal hydride with fully hydrogenated interstices (β-phase). The transition region, where both the phases coexist is indicated by the plateau in the isotherm (Figure 6).[71]

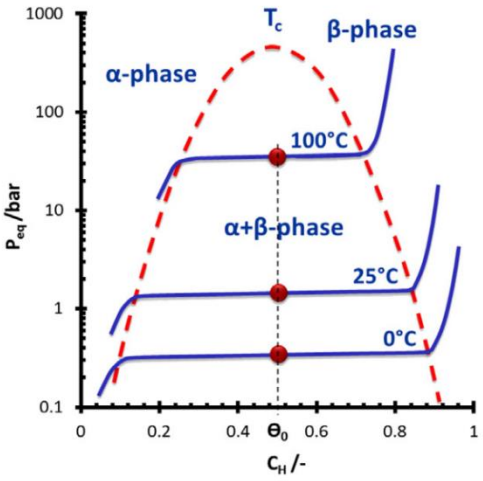

Figure 6: Sketch of an ideal equilibrium pressure/hydride concentration diagram for an hydrogen absorbing metal alloy.[71]

Partial substitution of the metals in the lattice is usually directed towards facilitating activation and decreasing the plateau pressures.[75,76] AB_2 type (Laves phase) materials are usually made by titanium or zirconium in A position and a transition metal in B positions. These alloys are often less expensive than AB_5 ones, due to the minor use of rare earth metals and also exhibit faster kinetics, but they are more prone to contamination.[75] As in other alloy families, the substitution of metals of the lattice lead in several cases to improvement of properties. The use of vanadium to increase the hydrogen storage capacities is common, but on the other hand the high cost of V hinders its commercial use and more economical vanadium-free alternatives are sought.[77] AB_3 structures, where A that is usually lanthanum, cerium or yttrium, have relatively low hydrogen storage capacity. $LaNi_3$ is one of the better known alloys of this family and stability improvements are achieved by partial substitution of La with Mg and Ni with Mn atoms.[78] The last kind of metal hydride widely studied for hydrogen storage purposes has the form A_2B. Ti_2Ni is one of the most interesting structures for hydrogen storage, and it is often modified by addition of other metals, zirconium being between the most common one.[79,80]

When hydrides are formed between hydrogen and alkali metals or the heavier alkaline earths (Ca, Sr and Ba), salt-like hydrides are obtained.

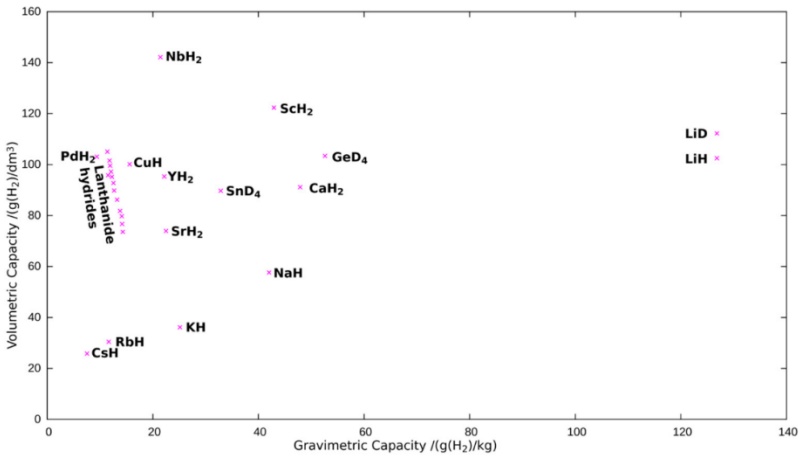

Figure 7: Plot of the hydrogen storage capacities of the binary metal hydrides.[81]

These hydrides are solid at room temperature and are classified as ionic due to their capacity of conducting electricity when melted or even very close to the melting point while H_2 is generated at the anode, revealing the presence of H^- ions. Their crystal structure is known and there is no evidence of directional covalent bonds, but instead, hydrogen atoms occupy all the octahedral interstitial lattice positions.[82] The salt-like metal hydrides are very reactive and for this reason they are often used as reducing agents. However, their facile oxidation renders their hydrogen desorption irreversible.[16,18] Moreover, their thermal decomposition is also difficult to use for hydrogen storage, due to the generally very high decomposition temperatures (for instance the LiH melting point is 688 °C, and the thermal decomposition temperature is ~700 °C[83]).

Despite the neighbouring position on the periodic table, magnesium hydride doesn't show a fully ionic behaviour, but mostly covalent. MgH_2 contains 7.6 wt% of hydrogen, a volumetric capacity of 110 g/L and the highest energy density (9 MJ/kg of Mg) among the reversible hydrides. Additional advantages include the magnesium abundance and low cost, making this hydride very interesting for hydrogen storage purposes. Despite all the good properties of this material, there are still many issues that do not allow a large-scale exploitation, in particularly for mobile applications. The first major disadvantage is the slow kinetics, due to the fast formation of MgO on the material surface, that reduces the hydrogen permeation as well as the surface formation of a MgH_2 layer during the hydrogenation itself. A second problem is related to the high stability of MgH_2, with a decomposition enthalpy of 75 kJ/mol of H_2 that requires temperatures between 300 and 400 °C to reach the thermodynamic equilibrium between Mg/H_2 and MgH_2 with a

plateau pressure of 1 bar. This temperature is 3 times higher than the common working temperatures of a PEMFC, while additionally even under these conditions the hydrogenation is extremely slow.[84–86] Numerous efforts have been devoted to overcome these problems, including the synthesis of nanosized Mg/MgH_2 systems;[87] the use of additives/catalysts like carbon,[88] polymers[85] or various metals[86,89] to improve reaction kinetics as well as the alloying with different elements to destabilize MgH_2.[90]

A general overview of the gravimetric and volumetric hydrogen storage capacities of binary metal hydrides is given in Figure 7.

2.4.3.4 Complex hydrides

Complex hydrides are generally defined as the salts of light metals of group I and II with $[AlH_4]^-$, $[NH_2]^-$, $[BH_4]^-$, known as alanates, amides and borohydrides. All these compounds are salts while hydrogen is found in the anionic part, covalently bound to a central atom in a “complex”. The high hydrogen volumetric and gravimetric density, coupled with the hydrogenation reversibility of some mixtures, make this family of materials one of the most promising for on-board hydrogen storage applications. However, there are several serious disadvantages (irreversibility and slow kinetics in the hydrogenation-dehydrogenation reactions) connected with these structures and they were thus considered totally unsuitable as potential hydrogen stores. This point of view changed drastically after Bogdanovic and Schwickardi demonstrated with their studies that aluminium hydrides (in particular sodium alanate, $NaAlH_4$ and sodium aluminium hexa-hydride Na_3AlH_6), exhibit improved kinetics and reversibility if doped with titanium compounds (e.g. $TiCl_3$).[91,92]

1.2.3.4.1 Aluminium hydrides

The aluminium hydride (alane, AlH_3) is a compound where hydrogen is covalently bonded to a central atom of aluminium. It is a metastable compound, solid and crystalline at normal temperature. Alane has been widely studied for hydrogen storage purposes due its great hydrogen content; the volumetric density is more than double of the liquid hydrogen (148 H_2/L) and the gravimetric density is higher than 10 wt%. Additional advantages include fast kinetics of desorption, and low temperature (<100 °C) H_2 release, which is optimal for fuel cell applications.[93]

A few years after AlH_3 was introduced in literature (early 1940s), Finholt et al. developed a method for its synthesis from $LiH/LiAlH_4$ with $AlCl_3$ in an ether solution.[94] Since then, seven different polymorphs of AlH_3 have been developed and adopted for many different purposes: as a reducing agent, rocket propellant, explosive but also as a hydrogen source for mobile power systems. Based on these applications the first "modification" target was to make the AlH_3 more stable to air and impurities for long periods of time. The stabilization often involved coating of the material with an inert layer such as aluminium oxide (Al_2O_3).[95] The sought of a material able to provide hydrogen with adequate kinetics at temperatures compatible with PEMFCs working conditions shifted the efforts to investigating methods of destabilization instead, in order to develop a light material able to desorb hydrogen with high rates at low temperatures. In such cases, the activation may involve ball milling, in order to increase the surface to volume ratio, doping or even UV irradiation. [93,96,97]

Aluminium compounds with hydrogen in the form of anionic complexes are known as alanates. The structure of $NaAlH_4$ is shown as an example in Figure 8. Like alanes, the high hydrogen content makes alanates interesting for hydrogen storage purposes. Additionally, another advantage of these compounds is their market availability in particularly as sodium and lithium salts. Other compounds, with magnesium, potassium or mixtures can be developed via simple chemical or mechanochemical reactions.[98,99] Hydrogenation-dehydrogenation cycling of some aluminium salts was also explored, mostly aided by catalytic doping,[92] and reversibility was registered for $NaAlH_4$, Na_2LiAlH_6, $LiAlH_4$, Li_3AlH_6 and $KAlH_4$.[100] Of all these aluminium hydrides, many have attractive characteristics pertaining to hydrogen content, reversibility, thermodynamic and kinetics properties but no material so far gathers all the necessary properties for on board hydrogen storage applications.[101]

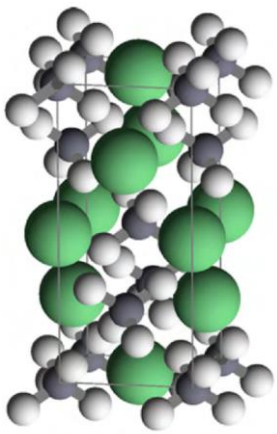

Figure 8: Equilibrium structure of $NaAlH_4$.[102]

2.4.3.4.1 Ammonia borane

Ammonia-borane ($H_3N{\bullet}BH_3$), indicated also as AB, is the simplest amine borane. It is a white crystalline solid. Due to its simplicity compared to other amino-boranes, but also its properties, AB is considered as a good candidate for solid state hydrogen storage purposes. Since the first synthesis of solid ammonia-borane, in 1955 by Shore and Parry[103], several other methods followed and are mostly grouped in three routes: Lewis acid-base exchange; salt-metathesis with hydrogen release; isomerization of diammonate of diborane.[104] AB has orthorhombic structure at low temperatures and tetragonal at - 48 °C (225 K).[105] The AB molecular crystals are different from ionic crystals, but, due to the unusual bonds, also different from other isostructural molecules, like ethane, a fact which is evident for example from the high melting point (112-114 °C).[104] The chemical composition of AB makes this molecule extremely hydrogen rich, with a total gravimetric capacity of 19,6 wt% and a volumetric content of 100-140 g/L. It is non-flammable and has a good stability at ambient temperatures and in water, where it is soluble due to its polarity. However, the hydrogen density of the system decreases if the presence of a solvent is necessary for hydrogen desorption. In aqueous solution AB is mostly stable at high pH values, while it is subject to fast hydrolysis in acidic conditions, a process that may be further catalysed by metals.[106] The major problems about the use of AB for hydrogen storage applications are the unfavourable thermodynamics related to the regeneration of the dehydrogenated molecule. The product of the complete dehydrogenation is boron nitride, an extremely stable molecule that poses a severe barrier to the reversibility of the system.[107] For this reason, it is preferable to stop the dehydrogenation to an intermediate stage, where the partially dehydrogenated products can be rehydrogenated under reasonable conditions. Generally, the decomposition of ammonia borane via simple pyrolysis undergoes a first release of hydrogen at 110 °C to obtain amino borane and polyaminoborane (PAB). Additional dehydrogenation occurs at 130 °C to borazine or polyiminoborane (PIB) and at much higher temperatures (1170-1500 °C) to the hexagonal boron nitride.[107] This aspect further reduces the useful amount of hydrogen that the molecule could deliver. Another problem arises from the compatibility with fuel cells, which are extremely sensitive to the presence of borazine or molecular amino boranes. Based on these problems the adoption of amino boranes for hydrogen storage in solid state requires further improvements and research.

2.4.3.4.2 Metal Amides and Imides

Metal amides and imides are another class of complex compounds, comprising a metallic centre and $[NR_2]^-$ or $[NR]^{2-}$ respectively, as coordination ligands. The R group, can have different chemical identities, but in the context of hydrogen storage, we will focus on the amide/imide forms with the higher hydrogen content, where R = H (i.e. $[NH_2]^-$ and $[NH]^2$).

The chemistry of metal amides was studied in detail during the 20th century, when many of these compounds were discovered. Gay-Lussac and Thénard for the first time obtained sodium and potassium amides, while different methods were tested and amides of lithium, cesium and rubidium have also been synthesized. In particular, among them, lithium amide was synthesized by Titherley in 1984.[108–110] The synthesis involved the direct reaction of the alkaline metal with ammonia, in gaseous or liquid form. Likewise, magnesium amide was also synthesised, by reaction of metallic Mg or the nitride Mg_3N_2 with NH_3. However, the slow reaction kinetics made this route not an optimal choice and new techniques have been developed, involving the reaction of MgH_2 with ammonia, to obtain both amides and imides of magnesium.[111,112] Along with Mg amides other variants have also been developed involving Ca, mixtures of alkali and alkaline earth metals, or alkali metal and aluminium amides.

The majority of all those amide compounds is used mostly in organic synthesis. In particularly $NaNH_2$ found extensive applications as a strong base in ammonia drying, condensation, dehydrohalogenation and cyclization reactions.

Chen et al.[113] revealed the potential of these materials for hydrogen storage as it was experimentally demonstrated that lithium nitride can be charged with a large amount of hydrogen and reversibly exchange it. From this point on, the general interest on amides for hydrogen storage increased dramatically.

2.4.3.4.3 Li-N-H compounds

Lithium based amides, imides and nitrides where key elements of the pioneering work of Ping Chen. Their relationship with hydrogen where first studied by Dafert and Miklauz, in 1910. They initially thought that the product of Lithium nitride hydrogenation was Li_3NH_4, but this was later corrected by Ruff and Goeres in 1911 who discovered that the product it's a mixture of lithium amide and lithium hydride.[29]

In brief, by adding hydrogen to Li_3N, it is possible to proceed with a two-step reaction from the nitride to the imide and then the amide of lithium as follows:

$$Li_3N_{(s)} + 2\ H_{2(g)} \rightleftharpoons Li_2NH_{(s)} + LiH_{(s)} + H_{2(g)} \rightleftharpoons LiNH_{2(s)} + 2\ LiH_{(s)}$$

In this respect, a capacity of reversibly storing up to 10.4 wt% was claimed for the Li-N-H system. In fact, Li_3N shows high hydrogen absorption capacities and fast hydrogenation kinetics from relatively low temperatures, starting at ~100 °C and reaching 9.3 wt% already after 30 minutes at 255 °C, while this value could be increased by eliminating impurities. Desorption occurs in two steps, as expressed in the reaction, however only the second part shows reversibility in practical conditions. The reaction involves the transformation of lithium amide and lithium hydride to lithium imide, with the release of 6.5 wt% hydrogen.

$$LiNH_{2(s)} + LiH_{(s)} \rightleftharpoons Li_2NH_{(s)} + H_{2(g)}$$

Apart from the hydrogen content, the enthalpy involved in this process is important and thus several pertinent measurements have been performed. The final result was a ΔH value of 67 kJ/mol for this hydrogen desorption reaction as determined by means of DSC analysis.[114]

The structure of $LiNH_2$ was investigated with several techniques, and also recently with high resolution neutron powder diffraction. The crystalline compound has a tetragonal structure with space group $I\bar{4}$, with lattice parameters: a = 5.03442(24) Å, b = 5.03442(24) Å and c = 10.25558(52) Å. Hydrogens occupy the 8g1(0.2429, 0.1285, 0.1910) and 8g2(0.3840, 0.3512, 0.1278) sites. The N-H bonds were calculated as 0.942 and 0.986 Å while the H-N-H bond angle is 99.97° (Figure 9). [115]

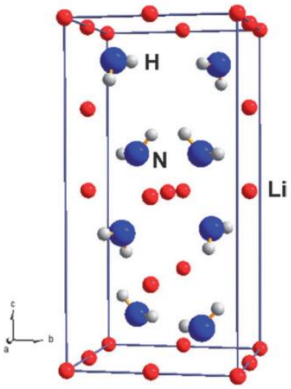

Fig. 3 Structure of $LiNH_2$.

Figure 9: Structure of $LiNH_2$.[116]

The decomposition of lithium amide involves the release of ammonia as a competitive reaction pathway, as follows:[117]

$$2LiNH_{2(s)} \rightarrow Li_2NH_{(s)} + NH_{3(g)}$$

Ammonia release is critical in hydrogen storage processes, since it contaminates the fuel cell catalysts, but simultaneously reduces the quantity of released hydrogen. If the reaction is allowed, the complete desorption of $LiNH_2$ would eventually lead to the conversion of all the material to LiH. This reaction starts at 175 °C and increases its kinetics at about 300 °C. However, the NH_3 equilibrium pressure is low enough (<1kPa at 300 °C) and thus ammonia desorption can be minimized under static pressure conditions.[118]

As already mentioned, lithium imide is, together with hydrogen, the intermediate product between the amide and the nitride in a reaction of hydrogenation-dehydrogenation, capable to store reversibly about 6.5 wt% at temperatures lower than 300 °C and with an “internal” 3.5 wt% hydrogen content. Li_2NH at low temperatures belongs to space group $Fd\bar{3}m$ and has a lattice constant of 10.09-10.13 Å between -173 and 27 °C (100 and 300 K). NH^{2-} ions are arranged in a close-packed configuration. H and N atoms occupy 32e sites with hydrogens tetrahedrally coordinated by vacant 8b sites and nitrogen tetrahedrally coordinated by lithium atoms on 8a and 48f sites. The distance between N and H (actually D as the experiments were carried out in deuterated Lithium

Imide, Li_2ND) was calculated to be 0.977 Å at -173 °C. The other atoms of lithium are positioned in partially occupied 32e sites.[119]

2.4.3.4.4 Mg-N-H compounds

Magnesium amides can be synthesized by the reaction of Mg or Mg_3N_2 with ammonia, in liquid or gaseous phase. However, the reaction is very slow, and can take years to complete. $Mg(NH_2)_2$ can be synthesized also by reaction between Mg and $NaNH_2$ but the reaction of MgH_2 with gaseous ammonia is generally preferred.[109,112] The reaction usually involves the mechanical milling of MgH_2 under high pressure of ammonia, as follows:[111]

$$MgH_{2(s)} + 2NH_{3(g)} \rightarrow Mg(NH_2)_{2(s)} + 2H_{2(g)}$$

The decomposition of $Mg(NH_2)_2$ involves two steps, both coupled with the release of ammonia. The first decomposition leads to magnesium imide, with a theoretical loss of 30 wt%, while the second leads to the corresponding nitride, reaching 40 wt% loss in accordance with the following reaction:

$$Mg(NH_2)_{2(s)} \rightarrow MgNH_{(s)} + NH_{3(g)} \rightarrow 1/3Mg_3N_{2(s)} + 4/3NH_{3(g)}$$

Experimentally, however, the decomposition is limited to 25 wt% and 32 wt%, respectively probably due to the presence of oxide impurities. The decomposition starts approximately at 127 °C with the two decompositions peaking approximately at 357 and 447 °C.[112] The decomposition mechanism of Magnesium compounds in the presence of hydrides (MgH_2 or LiH) is interesting for hydrogen storage applications, as it leads to nitrides, without any NH_3 desorption.[112] Additionally, $Mg(NH_2)_2$ has a high hydrogen content (about 7 wt%). Its structure at room temperature (Figure 10), is described as a sequence of “supertetrahedral” cluster units (an octahedral vacancy with non-adjacent faces covered by four $MgNH_4$ tetrahedra)[120] and was studied for the first time by Jacobs and Juza. They found by single crystal X-ray analysis, the presence of a tetragonal symmetry and lattice constant:

a = 10.37 Å, c = 20.15 Å, c/a = 1.943; Z = 32; space group $I4_1/a2/c2/d$.[121]

The imide product of the decomposition, was also studied by Juza and Jacobs. It can be described as a hexagonal cell[121] with lattice parameters a = 11.574 Å and c = 3.681 Å, space group P6/m and a unit cell containing 12 MgNH formula units.[120]

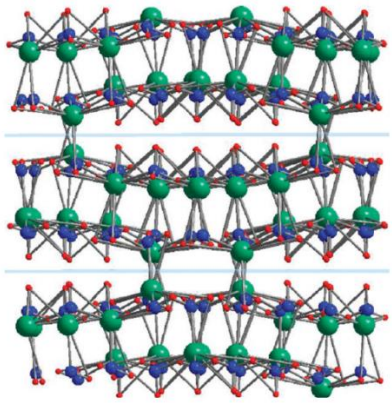

Figure 10: Structure of $Mg(NH_2)_2$.[122]

2.4.3.4.5 Li-Mg-N-H compounds

The thermodynamic properties of $LiNH_2$ make this material not suitable for hydrogen storage. The activation energy of 124 kJ/mol and the equilibrium with the relative imide at about 280 °C and 100 kPa of H_2 are unsuitable for practical applications.[123] However, it has been demonstrated that there is a possibility to decrease the hydrogen desorption temperature of lithium based complex hydrides by partial cation substitution with more electronegative cations, for instance Mg^{2+}.[124] In the presence of $Mg(NH_2)_2$, a drastic decrease of the sorption temperatures of about 130 °C has been registered. Moreover, even though magnesium amide releases ammonia during decomposition, the presence of lithium hydride suppresses this undesired reaction by fast reacting with ammonia.[112]

Several studies have been performed and different routes have been used to obtain a final destabilized product in the form of a ternary Li-Mg-N based compound. One way adopted uses $LiNH_2$ and MgH_2 as reactants; in this case the reaction with a ratio 2:1 affords $Li_2Mg(NH)_2$, showing reversibility and a stable rehydrogenation at 166°C. However, the product of rehydrogenation in this case is not the reactant lithium amide and magnesium hydride, but the magnesium amide and lithium hydride.[125]

The same dehydrogenation product was obtained also by using directly $Mg(NH_2)_2$ and LiH as starting materials. Several different compositions have been tested, affording consequently different products. For instance, upon decomposition of a mixture of $Mg(NH_2)_2$ and LiH with a ratio 3:8 there is no emission of NH_3, due to the fast reaction with LiH.[111]On the other hand, by using a 1:1 ratio both NH_3 and H_2 are generated, together with the $Li_2Mg_2(NH)_3$ ternary imide after a thermal treatment at 374 °C.[126]

These reactions have been replicated by Weidner et al.[127,128] who for the first time resolved the structure of deuterated $Li_2Mg(NH)_2$ and studied the decomposition pathways for the 1:2, 3:8 and 1:4 $Mg(NH_2)_2$: LiH mixtures. In their works Weidner et al.[127] determined that the 3:8 $Mg(NH_2)_2$: LiH mixture, desorbs at 220 °C, decomposes to a mixture of LiH, the alpha polymorph $Li_2Mg(NH)_2$ and a third cubic phase which can be attributed to the beta polymorph of $Li_2Mg(NH)_2$ or Li_2NH that disappears as soon as the hydrogen pressures is increased. By hydrogenation the 3:8 mixture generates LiH, $LiNH_2$ and $Li_2Mg_2(NH)_3$ and for hydrogen pressures above 71 bar also $Mg(NH_2)_2$. The 1:4 $Mg(NH_2)_2$: LiH mixture, at 200 °C decomposes fast and $Mg(NH_2)_2$ disappears while LiH becomes less detectable and $LiNH_2$ and $Li_2Mg_2(NH)_3$ are formed. The rehydrogenation of the mixture with this ratio happens without drastic conditions (already at 60 bar). The 1:2 mixture desorbs at 220°C generating $Li_2Mg(NH)_2$. This compound if hydrogenated, becomes first a mixture of $LiNH_2$, $Li_2Mg_2(NH)_3$ and LiH at around 50 bar, to proceed until complete hydrogenation at 70 bar pressure of hydrogen to $Mg(NH_2)_2$ and 2LiH.

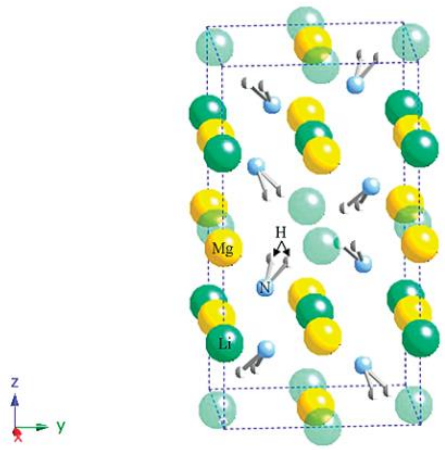

Figure 11: Structure of $Li_2Mg_2(NH)_3$. The translucent spheres denote a ~1/4 filled Li site. The hydrogen sites are half occupied.[128]

Among these reactions, particular attention was placed on the reversible reaction of hydrogenation of $Li_2Mg_2(NH)_3$.[129] This compound, was obtained decades earlier from the reaction of LiMgN with NH_3,[121] and later (2007)[126] synthesized from a mixture of $Mg(NH_2)_2$ and LiH with molar ratio 1:1, together with the formation of ammonia and hydrogen as follows:

$$2Mg(NH_2)_{2(s)} + 2\ LiH_{(s)} \rightarrow Li_2Mg_2(NH)_{3(s)} + NH_{3(g)} + 2H_{2(g)}$$

The compound was studied by Weidner et al.[128] where a model of $Li_2Mg_2(NH)_3$ was developed by indexing the reflections obtained from x-ray diffraction (Figure 11). A tetragonal cell symmetry, space group $I\bar{4}2m$ (121) and lattice parameters a = 5.130(3) Å and c = 9.619(1) Å were deduced.

A related reaction that takes place in similar conditions, involves the heat treatment of $LiNH_2$ and $Mg(NH_2)_2$ in a 1:1 ratio under ammonia backpressure. It was observed experimentally that the mixture of amides melts at about 350 °C and decomposes at about 374 °C generating $Li_2Mg_2(NH)_3$ and releasing NH_3:

$$2LiNH_{2(s)} + 2Mg(NH_2)_{2(s)} \rightarrow Li_2Mg_2(NH)_{3(s)} + 3NH_{3(g)}$$

The properties of this mixture are very attractive for infiltrating the molten phase in a porous scaffold, with the possibility to improve the hydrogen sorption capacity of the material.

The hydrogenation of $Li_2Mg_2(NH)_3$ involves an experimental uptake of 3.4 wt% of hydrogen which is completed at 350 bar and 250 °C.

The products of hydrogenation are evidently $Mg(NH_2)_2$ and LiH, with indications suggesting the presence of MgNH. The hydrogenation-dehydrogenation process follows the reaction:

$$Li_2Mg_2(NH)_{3(s)} + 2H_{2(g)} \rightleftharpoons Mg(NH_2)_{2(s)} + 2LiH_{(s)} + MgNH_{(s)}$$

The theoretical hydrogen storage capacity of $Li_2Mg_2(NH)_3$ according to this equation is 3.6 wt%, which is very close to what the experimental results revealed. Liu also calculated also the activation energy relative to the dehydrogenation of the process, obtaining ~92.7 kJ/mol.[129]

2.4.3.4.6 Borohydrides

The first borohydride synthesized was $Al(BH_4)_3$, obtained in 1939 by Schlesinger et al.[130] after the reaction of diborane with trimethyl aluminium, according to the equation:

$$Al_2(CH_4)_{6(l)} + 4B_2H_{6(g)} \rightarrow 2Al(BH_4)_{3(l)} + 2B(CH_3)_{3(g)}$$

Already in 1940 other alkali borohydrides have been synthesized. First of all the lithium borohydride, by reaction of diborane excess with ethyl lithium.[131] Schlesinger and Brown have also described how to obtain $LiBH_4$ as well as $NaBH_4$, KBH_4 and $U(BH_4)_4$ from the respective metal hydrides and diborane in solvent[132], according to the following general equation:

$$MH_{(s)} + B_2H_{6(g)} \rightarrow 2MBH_{4(s)} \qquad \text{with M = Li, Na, K, 1/2Mg, etc}$$

The difficulties of handling diborane, due to its toxicity, self-ignition and explosive reaction with air or moisture, have pushed researchers to find safer ways to synthesize borohydrides. Some methods use triethylamine borane or dimethylsulfide borane which are safer. These routes however, involve the use of solvents that require further post-synthesis steps to be removed.[133,134]

Metathesis reactions is also a common approach for the synthesis of borohydrides, particularly by substitution of the metal of an alkali borohydride with another metal, chemically bonded with halides.[135] Due to the tendency of affording as product the most thermodynamically stable compound, a problem of this kind of synthesis is that it is difficult to obtain borohydrides with two or more metals.

This problem can be avoided with mechanochemical synthesis techniques. In these cases, synthesis is performed via ball milling, and the development of pure bi- and trimetallic borohydrides from monometallic precursors is possible.[136] Ball milling can also be used to trigger metathesis reactions, in particularly for the synthesis of monometallic borohydrides starting from alkali borohydrides and metal halides.

Nevertheless, it is common to obtain additional unwanted by-products due to the complex reactions that take place during the mechanochemical treatment.[137] The mechanochemical routes for the synthesis of borohydrides can be also carried out under reactive gasses, for example diborane, so that gas-solid reactions are taking place.[138]

An alternative synthesis method of for the borohydrides of alkali and alkaline earth metals that involves reactive gasses is the direct reaction of the metal, boron and hydrogen at high temperatures, of around 550 – 700 °C, under 3-15 MPa of hydrogen.[91] The general reaction can be described as:

$$M_{(s)} + B_{(s)} + 2H_{2(g)} \rightarrow MBH_{4(s)} \qquad \text{with M = Li, Na, K, 1/2Mg, etc}$$

Other methods of synthesis may involve the single crystal growth of borohydrides starting from solutions or the creation of borohydrides complexed by neutral molecules such as ammonia (obtaining ammonia borane) or hydrazine.[138]

The major application of borohydrides is in organic chemistry as reducing agents and this is highlighted by the 1979 Nobel prize awarded to H.C. Brown for the synthesis and use of $NaBH_4$. However, alternative applications have emerged with time. Due to their high hydrogen content, borohydrides became particularly attractive for the possibility to be used as hydrogen storage media with particular attention being given to $LiBH_4$ due to its high (~18.4wt%) hydrogen content.

A big problem related to their application, particularly in the automotive field, is the high stability of these compounds, and consequently the high working temperatures that are required. This behaviour is directly connected to the ionic interaction between the M^{n+} cations and $[BH_4]^-$ anions of the $M(BH_4)_n$ compounds. In fact, after the systematic investigation of the thermodynamic stabilities of several metal hydrides with M = Li, Na, K, Cu, Mg, Zn, Sc, Zr and Hf, Nakamori et al.[139] found a correlation between the Pauling electronegativity of the cation, χ_P, and the heat of formation of $M(BH_4)_n$ (ΔH_{boro}). The correlation represented mathematically by the linear relation for these complexes:

$$\Delta H_{boro} = 248.7\chi_P - 390.8 \text{ (kJ/mol of } BH_4)$$

The decomposition, with consequent release of hydrogen is generally performed via thermolysis. This process can be easily influenced by several factors that may significantly affect the decomposition pathways. These include among others, the addition of catalysts or variation of conditions such as the gas partial pressures.

The reaction of dehydrogenation may follow different routes, depending on the nature of the starting borohydride. For instance, along with the evolution of H_2, dehydrogenation can include the production of elemental boron and metal hydrides or composite products of boron and metal(s).

In specific, for alkali borohydrides:

$$MBH_{4(s)} \rightarrow MH_{(s)} + B_{(s)} + 3/2H_{2(g)} \quad \text{or} \quad MBH_{4(s)} \rightarrow MB_{(s)} + 2H_{2(g)}$$

And for the alkaline earth borohydrides:

$$M(BH_4)_{2(s)} \rightarrow MH_{2(s)} + 2B_{(s)} + 3H_{2(g)} \quad \text{or}$$

$$M(BH_4)_{2(s)} \rightarrow MB_{2(s)} + 4H_{2(g)} \quad \text{or}$$

$$M(BH_4)_{2(s)} \rightarrow 2/3MH_{2(s)} + 1/3MB_{6(s)} + 10/3H_{2(g)}$$

An alternative decomposition route for the borohydrides may involve the evolution of diboranes. This competitive decomposition can also be linked to the Pauling electronegativity of the cation. However, even if there are no clear trends between electronegativity and the amount of diborane released, it has been possible to define that during decomposition, diborane is produced when the metal has an electronegativity in the range between $1.36<\chi_P<1.55$.[140] This is the most undesirable byproduct of borohydrides decomposition due the loss of capacity, the possibility to damage the catalysts and the membranes of fuel cells and last, but not least, the very high toxicity of these compounds.

2.4.3.4.6.1 $LiBH_4$

Lithium borohydride was synthesized for the first time in 1940 by Schlesinger et al.[131] through the reaction of diborane with ethyl lithium. The product is a salt-like,

hydroscopic, crystalline compound formed by the ionic interactions between the lithium cation and the BH_4^- anions. Lithium borohydride has a reported melting point of 275-278 °C and density 0.66-0.68 g/cm^3 at 25 °C. At 0 °C the material does not decompose and its vapor pressure is less than 10^{-5} mbar. At 298.15 K an enthalpy of formation ΔH_f = -194.44 kJ/mol has been determined.[141] The synthesis of this compound can be carried out also by direct reaction of diborane with the lithium hydride, in absence of a liquid medium,[142] according to the following reaction:

$$2LiH_{(s)} + B_2H_{6(g)} \rightarrow 2LiBH_{4(s)}$$

Industrially $LiBH_4$ is synthesized by metathesis reaction of $NaBH_4$ with halides of lithium (LiCl, LiBr) in solvents that may be ether of isopropylamine.[143] The reactions involved are the following:

$$NaBH_{4(s)} + LiCl_{(s)} \rightarrow LiBH_{4(s)} + NaCl_{(s)}$$

$$NaBH_{4(s)} + LiBr_{(s)} \rightarrow LiBH_{4(s)} + NaBr_{(s)}$$

Like other light alkali borohydrides the synthesis of $LiBH_4$ is possible also by direct reaction of lithium with boron and hydrogen. However, due to the inert behaviour of boron, the reaction does not occur at low temperatures and only after increasing the temperature to about 550-700 °C and the hydrogen pressure to 3-15 MPa it is possible to carry out the reaction.[91]

$$Li_{(s)} + B_{(s)} + 2H_{2(g)} \rightarrow LiBH_{4(s)}$$

Structurally, lithium borohydride has been found to have four polymorphs. At ambient conditions $LiBH_4$ crystallizes with an orthorhombic structure (Pnma), where each anion BH_4^- is surrounded by four Li^+ cations, each surrounded by four anions (Figure 12).[144] The B-H bond length calculated at 3.5 K is 1.226(5) Å.[145] At 110 °C the compound goes through a polymorphic transition from orthorhombic to the hexagonal wurtzite-like h-

$LiBH_4$ polymorph ($P6_3mc$).[144] At this high temperature, the tetrahedra are disordered and the length of the B-H bond becomes 1.31(11) Å.[145]

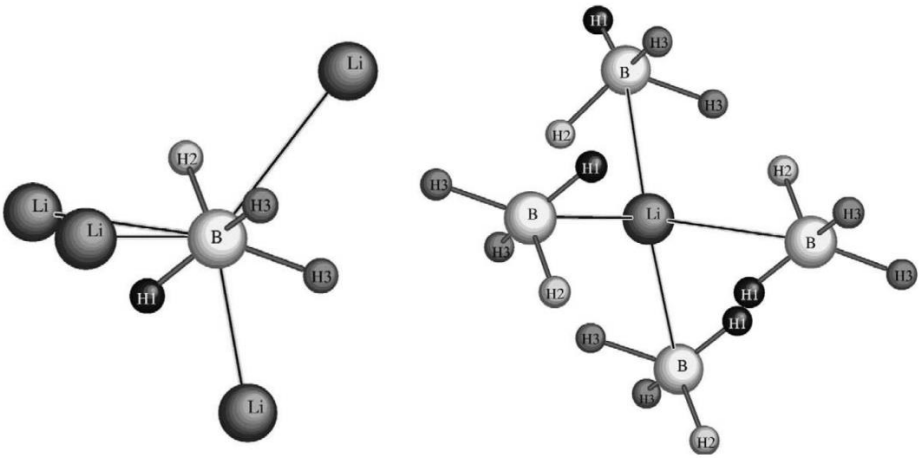

Figure 12: Boron (left) and lithium (right) coordination at room temperature.[144]

Under high pressures, $LiBH_4$ shows two more polymorphic phases. Firstly, there is a transition at 1.2 GPa (room temperature) from the ambient pressure orthorhombic phase I to the so-called phase II. This structure shows an arrangement where BH_4 anions are coordinated in a square-planar geometry by four lithium cations. Upon further pressure increase it is possible to obtain another transition from phase II to phase III. The transition starts at 10 GPa, and the best description leads back to a cubic structure with disordered BH_4 ions.[146] With a content of 18.4 wt% of hydrogen, lithium borohydride is the most interesting compound among the borohydrides. Hydrogen stored in this molecule can be obtained by thermolysis. Generally the decomposition is mostly influenced by the thermolysis conditions, i.e., temperature and partial pressure, but also the presence of impurities can be linked to particular decomposition behaviour.[147] The direct decomposition of $LiBH_4$ at high temperatures leads to desorption of 13.1 wt% of hydrogen, together with the formation of boron and lithium hydride according to the following reaction:

$$LiBH_{4(s)} \rightarrow LiH_{(s)} + B_{(s)} + 3/2H_{2(g)}$$

In case of a less endothermic reaction only partial decomposition may take place, with the simultaneous formation of lithium closoborane ($Li_2B_{12}H_{12}$), lithium hydride and hydrogen, as shown below:

$$LiBH_{4(s)} \rightarrow 5/6LiH_{(s)} + 1/12Li_2B_{12}H_{12(s)} + 13/12H_{2(g)}$$

By applying a low heating rate it was possible to identify a multistep decomposition, with tree phases (Figure 13). A first decomposition with a limited release of hydrogen (around 0.3 wt%) happens between 100 and 200 °C. At 270 °C $LiBH_4$ melting starts without any H_2 desorption. Hydrogen starts to be detected at 320 °C, and at this stage another 1 wt% is released. At 400 °C however, the material starts to decompose continuously, until a peak is reached at around 500 °C, with a variable maximum amount of hydrogen released up to 600 °C.

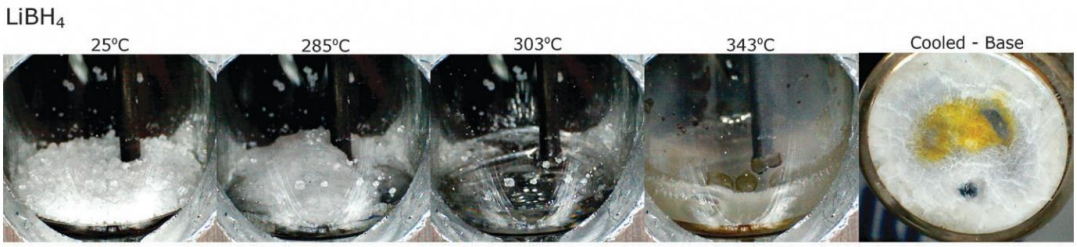

Figure 13: Photographic sequence of $LiBH_4$ thermal decomposition at 10 °C/min under 1 bar of Ar. [147]

The wt% of hydrogen released at these temperatures depends on the experimental conditions and ranges from 9 wt% under static conditions (pressure is built up from the desorbed hydrogen) to 13.8 wt% under dynamic conditions (use of a carrier gas such as helium). However, the decomposition cannot proceed further due to the formation of LiH, which is stable up to 900 °C.[138,141,148–150]

2.4.3.4.6.2 $NaBH_4$

Sodium borohydride was synthesized in 1941 by Schlesinger and Brown,[132] but due to the second world war the results were published in 1953. In their work, the synthesis was performed in the presence of a liquid medium by reaction of sodium hydride with

trimethyl borate, in order to obtain sodium borohydride and sodium methoxide based on the following reaction[132]:

$$4NaH_{(sln)} + B(OCH_3)_{3(l)} \rightarrow NaBH_{4(sln)} + 3NaOCH_{3(sln)}$$

After the synthesis, performed at 250 °C, the product can be extracted by liquid ammonia or primary amines. The solid obtained is a white crystalline ionic compound comprising Na^+ cations and BH_4^- anions. It has high stability, with melting point at 505 °C and a slow decomposition above 534 °C under 1 bar of hydrogen. [147,151] The high stability of $NaBH_4$ is evident by the calculations of the enthalpy of formation. The $\Delta_f H_{0K}$ is -248.50 kJ/mol of $NaBH_4$. The enthalpy value becomes -210.73 by including the zero-point contribution of Na, α-B, H_2 and $NaBH_4$ and the commonly reported values range between -191kJ/mol and -188kJ/mol for the $\Delta_f H$ at T = 300 K.[152] Sodium borohydride can be obtained via a wide number of synthesis routes, however, the most widely used ones are the Schlesinger (mentioned above) and the Bayer processes, which are employed for commercial and large scale production of $NaBH_4$. The Bayer process is a one-pot synthesis combining metallic sodium, borax and hydrogen in the presence of silica in order to obtain sodium silicate and sodium borohydride. The main reaction is the following:

$$Na_2B_4O_{7(s)} + 7SiO_{2(s)} + 16Na_{(s)} + 8H_{2(g)} \rightarrow 4NaBH_{4(s)} + 7Na_2SiO_{3(s)}$$

The reaction takes place at high temperatures of about 400 - 500 °C. At this temperature sodium melts and the reaction takes place in a partially solid phase under some bar of hydrogen pressure. At the beginning a mixture of quartz sand and borax are fused together in a borosilicate glass that reacts with metallic sodium and H_2. The $NaBH_4$ produced is usually extracted by liquid ammonia, and the pure product is obtained by evaporation of the residual ammonia.[153] The production is not cost efficient and several studies have been performed in order to reduce the costs of the Bayer process, by e.g. introducing less expensive reactants like MgH_2 as reducing agent and including recycling processes of the products. [154] The main reaction is the following:

$$NaBO_{2(s)} + 2MgH_{2(s)} \rightarrow NaBH_{4(s)} + 2MgO_{(s)}$$

Other synthetic routes include the direct thermal reduction of sodium metaborate. These processes may involve methane, hydrogen or carbon, in order to obtain $NaBH_4$ respectively with the reactions:[155]

$$NaBO_{2(s)} + CH_{4(g)} \rightarrow NaBH_{4(s)} + CO_{2(g)}$$

$$NaBO_{2(s)} + 2H_{2(g)} \rightarrow NaBH_{4(s)} + 2H_2O_{(l)}$$

$$NaBO_{2(s)} + C_{(s)} + 2H_{2(g)} \rightarrow NaBH_{4(s)} + CO_{2(g)}$$

or

$$NaBO_{2(s)} + 2C_{(s)} + 2H_{2(g)} \rightarrow NaBH_{4(s)} + 2CO_{(g)}$$

Formaldehyde has also been suggested as a potential reducing agent for reactions with boron oxide or sodium metaborate due to its higher reactivity compared to methane or coke which leads to lower reaction temperatures. However, the reactions with the boron oxide are not favoured under standard conditions; even with the addition of calcium oxide, in order to assist the reaction through the formation of calcium carbonate, high yields have not been accomplished so far.[155] The reaction of formation of sodium borohydride with formaldehyde is given below:

$$NaBO_{2(s)} + 2HCHO_{(l)} + 2CaO_{(s)} \rightarrow NaBH_{4(s)} + 2CaCO_{3(s)}$$

Finally, alternative methods for the synthesis of borohydrides or at least the activation of boron oxides, in order to obtain more reactive boron compounds such as B_2H_6, involve the use of metallic reducing agents, as in the Brown-Schlesinger process. In these cases, the metal centre of e.g. metal hydrides, is able to exchange hydrogen with boron. Magnesium, primarily in the form of MgH_2 is one of the most attractive materials in this context.[156,157]

At room temperature $NaBH_4$ crystallizes in a cubic structure. The structure of the deuterated form resolved by neutron powder diffraction belongs to space group $F\bar{4}3m$ with a = 6.137(7) Å, B-D = 1.1160(7) Å (Figure 14). The bonds D-B-D have an angle of

109.5(2)° with deuterium atoms oriented in tetrahedral geometry relatively to the boron atoms at 295 K.[158]

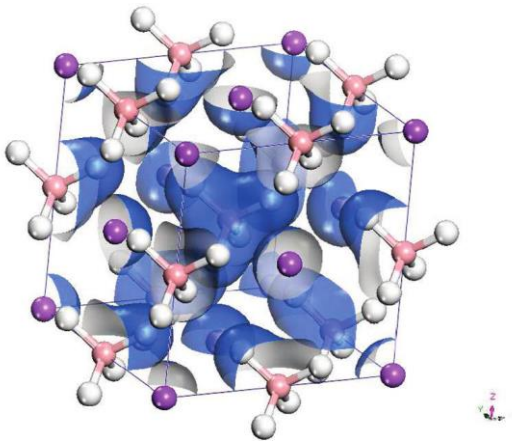

Figure 14: α-NaBH4 structure with symmetry group $F\bar{4}3m$.
Isodensity surface at 0.20 electron $Å^{-3}$ of the total electron density.[152]

At room temperature the cubic structure is stable up to 5.4 GPa. Beyond this pressure it is possible to see transitions, through a tetragonal phase ($P42_1c$) at 6.3 GPa with a = 4.0864(1) Å, c =5.5966(7) Å to orthorhombic phase (Pnma) starting at 8.9 GPa with a = 7.3890(1) Å, b = 4.1660(2) Å and c = 5.6334(5) Å.[159] At low temperatures (190 K) $NaBH_4$ shows an order-disorder transition due to the reorientation of the BD_4 tetrahedra. At 10 K the structure of $NaBD_4$ established by neutron powder diffraction is ordered and belongs to space group $P4_2/nmc$, with lattice parameters a = 4.332(1) Å and c = 5.869(1) Å.[160]

$NaBH_4$ is particularly important as a reducing agent, while it is nowadays considered as one of the most promising materials for hydrogen storage due to its high hydrogen content (10.6 wt%).[151] A major problem for the application of $NaBH_4$ is its thermal stability leading to high desorption temperatures (>460 °C), however, it releases hydrogen very easily by reacting with water according to the following reaction:

$$NaBH_{4(s)} + 2H_2O_{(l)} \rightarrow NaBO_{2(s)} + 4H_{2(g)}$$

This reaction is irreversible, but it has the great advantage that 50% of the H_2 generated comes from water, with $NaBH_4$ acting like a water splitting agent. In this case,

considering the mass of $NaBH_4$ it is possible to release an amount of H_2 corresponding to 21 wt%. Apart from the synthesis of $NaBH_4$, Schlesinger and Brown have also studied how the reactivity of $NaBH_4$ changes with temperature, by using acidic conditions or by the addition of catalysts.[161]

The thermal decomposition of $NaBH_4$ takes place in different steps in a range of temperatures between 400 and 595 °C (Figure 15). The white salt-like compound starts to change colour above 460 °C, indicating an initial desorption in the solid state. At 510 °C melting starts, and the material becomes a transparent liquid at 530 °C. In this phase there is evidence of a small release of hydrogen as minor bubbling. In this first phase approximately only 1 wt% of the total content is released. The full decomposition, takes place at 534 ±10 °C.[125]

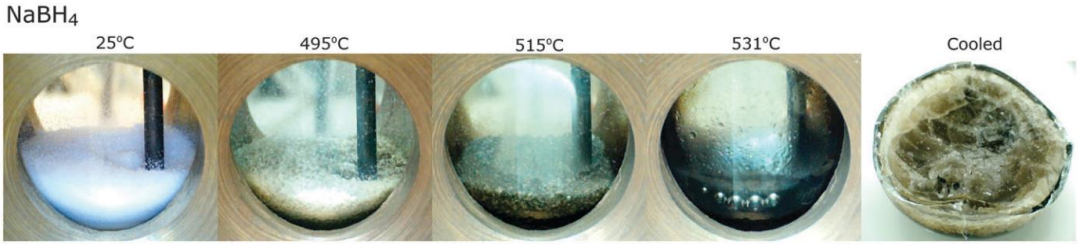

Figure 15: Photographic sequence of $NaBH_4$ thermal decomposition at 10 °C/min under 1 bar of Ar.[147]

From decomposition experiments and the Van't Hoff equation it was possible to determine the enthalpy, ($\Delta_r H$ = -108 ± 3 kJ/mol of H_2 released) and entropy ($\Delta_r S$ = 133 ± 3 J/Kmol of H_2) of the reaction. The decomposition products comprise two solid phases, which can be elemental Na and B (or a boron rich phase).[152]

2.4.3.4.6.3 KBH_4

As already mentioned, potassium borohydride, together with other borohydride compounds was synthesized for the first time by Schlesinger and Brown between the 1940s and 1950s.[163] The similarities between potassium and sodium borohydrides were directly observed. The first synthesis was possible by reaction of diborane with potassium tetramethoxyborate ($KB(OCH_3)_4$), due to the lack of reactivity between

diborane and potassium methoxide, contrary to the correspondent sodium compound. The reactions involved are the following:

$$KOCH_{3(s)} + B(OCH_3)_{3(l)} \rightarrow KB(OCH_3)_{4(s)}$$

$$3KB(OCH_3)_{4(s)} + 2B_2H_{6(g)} \rightarrow 3KBH_{4(s)} + 4B(OCH_3)_{3(l)}$$

The product is a non-volatile, stable, white salt-like compound, comprising tetrahedral $[BH_4]^-$ and K^+ ions. The presence of potassium cations makes this compound heavier than the corresponding hydrides of lithium and sodium, with a density of 1.17 g/cm^3 and much less hydrogen storage capacity (7.42 wt%).[91] Since its discovery, KBH_4 was used mostly in the pharmaceutical industry.[164] The production was based on the reaction of sodium borohydride with potassium hydroxide, in order to obtain, with a yield of about 85-90%, potassium borohydride and sodium hydroxide according to the following reaction:

$$NaBH_{4(s)} + KOH_{(s)} \rightarrow KBH_{4(s)} + NaOH_{(s)}$$

Alternative methods are the synthesis from the direct reaction of the potassium hydride with the alkyl borate. This reaction works well for sodium, but not for potassium and heavier alkali metal hydrides, due to low reactivity, high cost and low yield. The synthesis of potassium borohydride can be obtained also by reaction of $KB(OCH_3)_4$ with diborane, but the use of this reaction was always limited to the laboratory production.[165]

As the other alkali borohydrides (Na, Rb and Cs) KBH_4 at room conditions crystallizes in a NaCl-like $Fm\bar{3}m$ cubic structure with lattice constant a = 6.69 Å and $[BH_4]^-$ octahedrally surrounded by K^+.[166] At low temperature the α-KBH_4 phase changes to assume a tetragonal β-KBH_4 phase that belongs to the space group $P/4\bar{2}_1c$. The low temperature transition for the KBH_4 leads to a more ordered atomic arrangement. Upon increasing the pressure to 4 GPa there is a transition from the α-KBH_4 phase to β-KBH_4 which has a tetragonal geometry, with space group $P4\bar{2}_1c$.[167] With a further increase of pressure to 7 and 11 GPa it is possible to see another high pressure phase of KBH_4 with orthorhombic structure.[168]

The relatively high hydrogen content makes KBH_4 interesting for hydrogen storage purposes and several efforts have been devoted to hydrogen release by hydrolysis

reactions. Research has focused on investigating controlled ways to release hydrogen from KBH_4 and water at high pH, taking advantage its good stability in aqueous media.[169] Other studies focused on using direct thermolysis of solid state KBH_4, often in mixtures with other borohydrides. However, the great stability of this material, with an enthalpy of formation, $\Delta_f H$ = -229 kJ/mol,[91] makes the thermal decomposition more challenging in comparison with the other alkali metal borohydrides. The first reactions take place at temperatures higher than 500 °C and only beyond ~540 °C, KBH_4 starts changing colour, from white to yellow and brown tones, highlighting a first hydrogen release when the material is still in the solid state (Figure 16). Above 590 °C the hydride turns to shades of green and blue. From visual experiments, KBH_4 melts at 606 °C while previous literature data set the melting point at about 625 °C. A conspicuous hydrogen release occurs only at much higher temperatures (ca. 680 °C).[147]

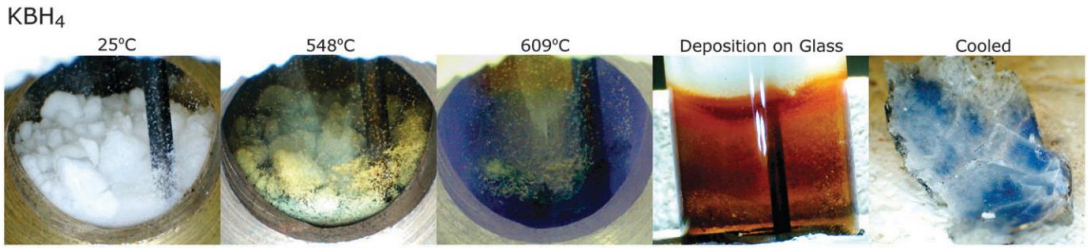

Figure 16: Photographic sequence of KBH_4 thermal decomposition at 10 °C/min under 1 bar of Ar. [147]

2.4.3.4.6.4 Eutectic $LiBH_4$ – $NaBH_4$ mixture

The revival of interest for borohydrides and the possibility to use them as hydrogen storage materials, have also triggered new attempts to improve their properties. The increase of cyclability and reduction of activation energies of these compounds is pivotal in terms of their application. Destabilization can be induced by mixing with dopants like halides or by developing composite materials that include other hydrides or borohydrides.[170–174] The first investigations on the miscibility of the borohydrides of lithium and sodium have been performed in the early 1960s, when Adam highlighted the presence of eutectic melting in a $LiBH_4$ rich mixture.[175] The $LiBH_4$ – $NaBH_4$ was investigated in detail only in 2016 by Dematteis et al.[176] and the presence of an eutectic

point in a mixture of $LiBH_4$ and $NaBH_4$ at 71 % mol of $LiBH_4$ at 219 °C with an enthalpy of melting of 7.07 kJ/mol was determined with precision.[176]

The mixture melts without any significant hydrogen evolution and only minor bubbling can be observed (Figure 17). The major release for the pure borohydride mixture is recorded only above 350 °C, together with obvious liquid spreading due to intense bubbling. The decomposition processes in three main desorption incidents, with the second occurring at about 450 °C and a third at about 500 °C. In general such low temperature decomposition phenomena are unexpected and have been explained after considering possible destabilizing interactions between the alkali cations Li^+ and Na^+ in the liquid phase.[147]

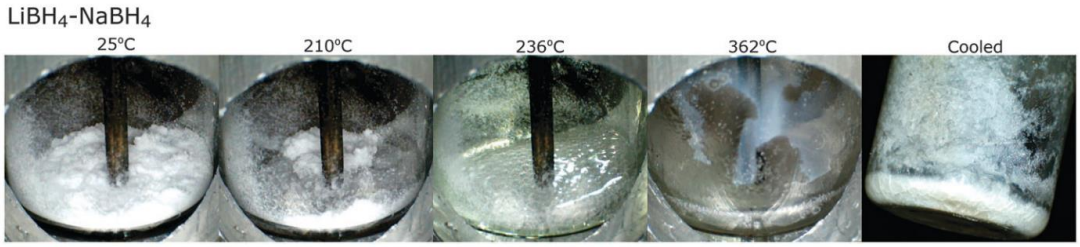

Figure 17: Photographic sequence of $0.62LiBH_4 – 0.38NaBH_4$ (composition antecedent to the more accurate one with the $LiBH_4$ at 71%) thermal decomposition at 10 °C/min under 1 bar of Ar.[147]

Pure $LiBH_4$ shows a polymorphic transition from an orthorhombic to a hexagonal phase at about 110 °C[144] and melts completely at 280 °C. $NaBH_4$ on the other hand, melts at 505 °C.[147] $NaBH_4$ when dissolving into the orthorhombic $LiBH_4$, is able to stabilize the hexagonal structure of $LiBH_4$, reducing the temperature of the polymorphic transition that starts at about 100 °C. The same transition, but in opposite direction (o to h) was detected while cooling the material at 97 °C and the same temperature is obtained theoretically via the CALPHAD (CALculation of PHAse Diagrams) methodology. Furthermore, approximately at these temperatures (around 94 °C) the point of complete solubility (solvus line) of $NaBH_4$ into the orthorhombic solid solution was also detected.[176]

The mixture, with a molar ratio of 0.71: 0.29 ($LiBH_4$ - $NaBH_4$), due to the lithium borohydride rich composition, has a high hydrogen content, equal to 15.25 wt%. This aspect makes the material particularly interesting for solid state hydrogen storage applications. However, like the pure components, the mixture itself doesn't show hydrogen sorption reversibility, hampering any application. On the other hand, thanks to

its low temperature melting it is possible to achieve improvements on sorption kinetics and cyclability. The presence of a low temperature molten phase in fact opens the way for the synthesis of composite materials as well as the nanoconfinement of borohydrides, without passing through long and elaborate wet chemistry processes of solubilization, infiltration and solvent extraction. Some studies have already been performed with the purpose of increasing kinetics and decreasing the release temperature of the materials under analysis by introducing borohydrides in porous carbons. Some examples of borohydrides mixtures infiltrated reported in literature are the $LiBH_4$ – $Ca(BH_4)_2$ eutectic mixture[177–180], $LiBH_4$ – $Mg(BH_4)_2$[181–184], $LiBH_4$ – Mg_2NiH_4[185] and $LiBH_4$ – $NaAlH_4$[186]. The eutectic mixture of $LiBH_4$ – $NaBH_4$ itself was already been confined in porous carbon scaffolds.[187] On this system the nanoconfinement in carbon scaffold showed some improvement from the kinetic point of view and signs of reversibility in hydrogen uptake. However, the nanoconfinement effect was studied only on one carbon scaffold. The material used was an aerogel-type carbon, with an average pore size of 37 nm, which is relatively large, and it is still not clear if the improvements are due to nanoconfinement or to a catalytic effect of the carbon surface with the borohydrides. Improvements on this system are still possible and a detailed study on the effect of the nanoconfinement in different and much smaller pore sizes is still missing in literature. In this respect, part of the work of this thesis was focused on this objective.

2.4.3.4.6.5 Eutectic $LiBH_4$ – KBH_4 mixture

For similar reasons a better understanding the $LiBH_4$ – KBH_4 system could lead to improvements in its hydrogen storage properties. The system has been studied already during 1960s[175], when the presence of eutectic compositions with very low melting temperature for borohydrides was discovered. Nevertheless, a systematic study for determination of the precise composition was performed only at 2014 by Ley et al.[188]. The lowest melting point for the mixture was obtained for the composition 0.725 $LiBH_4$ – 0.275 KBH_4 at about 105 °C, which is actually up to now the lowest melting temperature for alkali and alkali earth metal borohydride mixtures. In fact, the mono-metallic borohydrides, with the form $M(BH_4)_x$, where M = Li, Na, K, Mg and Ca have all melting temperatures, T_m higher than 250 °C.[147] Decrease of melting temperatures on non-doped borohydrides have also been observed in borohydride mixtures in cases of destabilization due to cation substitution and consequent changes of the atomic

distances between the metal cations and the boron centers.[189] This is the case of the eutectic mixture of $xLiBH_4 – (1-x)Mg(BH_4)_2$ with x = 0.5-0.6 with a melting temperature T_m = 180 °C[183,190,191], as well as the already mentioned $xLiBH_4 – (1-x)Ca(BH_4)_2$ eutectic mixture with x = 0.68 [177–180] and melting point at about 200 °C. Among the low melting temperature borohydride eutectic mixtures the mixture $x\ LiBH_4 – (1-x)\ NaBH_4$ x = 0.71, is again noted with melting temperature T_m=216 °C. Such low melting temperature of the $LiBH_4 – KBH_4$ eutectic mixture, in contrast with the pure compounds, $LiBH_4$ T_m = 280 °C and KBH_4 T_m = 625 °C, may allow low temperature infiltrations and opens new possibilities for the synthesis of new composite materials. Due to its composition (lithium borohydride rich), $0.725LiBH_4 – 0.275KBH_4$, it has a content equal to 13.2 wt% of hydrogen, that makes this compound really interesting for hydrogen storage purposes. The infiltration in porous materials, the confinement and the reduction of particle sizes to the nanoscale may drastically change the material behaviour and improve the cyclability and storage capacity of the bulk material. The infiltration of this borohydride eutectic mixture has already been performed by Roedern et al.[192] on a carbon aerogel and improvements on the material properties have been registered. However, the carbon aerogel used had relatively large pore size (diameter of 27 nm) while only one carbon scaffold, with a single pore size was tested. Moreover, it is still not clear if the improvements can be attributed to a catalytic effect due to the borohydride-carbon contact, to the nanoconfinement or both. Further tests with different carbons and smaller pore size are missing, as well as a detailed study of the cycling properties and relative hydrogen uptake capacity. Improvements on this system are still possible and therefore a part of this thesis has focused on the synthesis and study of several composite materials of nanoconfined $LiBH_4 – KBH_4$ eutectic mixture in small size carbon pores.

CHAPTER 3
NANOSCALE AND NANOPARTICLES

As already highlighted, metal and complex hydride materials do not fulfil the requirements of viable large scale solid-state hydrogen storage systems. The reason is often placed in the low hydrogen content, high temperature release and lack of reversibility. Looking in particular at metal borohydrides the main problems are connected with high thermodynamic stability, which eventually leads to impractically high hydrogen desorption temperatures while there are several issues related to cycling/rehydrogenation of the materials.

A way to overcome such problems may be based on nano-sizing. In principle, by following different nano-sizing approaches materials with particle sizes in the low end of the nanoscale (typically 1-10 nm) can be obtained. In general, nanostructured materials, (nanocrystalline, nanophase etc), have properties that deviate from those of the micro-sized crystals. There are three main categories of nanostructured materials: materials with reduced dimensions in the form of nanosized particles, two dimensional materials, e.g. in the form of layers and thin films and bulk materials with a structure on the nanometre scale, with atoms organized in crystallites or small atomic groups with dimensions of a few nanometres.[193] Due to the high surface areas of nanomaterials (actually high surface to volume ratios), their surface energy plays a more important role than in bulk materials. When the surface energy of the hydride is bigger than the elemental form, part of the heat of formation is stored as an excess surface energy. This reduces the enthalpy of formation of the hydride and thus the dehydrogenation temperature. More specifically, for a simple reaction of a nanosized metal particle M and hydrogen to a metal hydride MH_2 ($M+H_2 \rightarrow MH_2$), the contribution by excess surface energy has to be taken into account. The molar free energy of formation of a metal hydride particle becomes:

$$\Delta G(r) = \Delta G_0(r) + RTln\left(\frac{A_{MH_2}}{A_M P_{H_2}}\right) + \frac{3V_M E_{M\rightarrow MH_2}(\gamma, r)}{r}$$

Where *r* is the radius of a spherical particle, *A* is the activity coefficient of the phases, P_{H_2} is the pressure of the hydrogen gas, *V* represents the molar volume of each phase

before and after the hydride formation, γ is the surface energy and the surface term $E_{M\rightarrow MH_2}$, is a surface energy term that has a value given by:

$$E_{M\rightarrow MH_2}(\gamma, r) = \left[\gamma_{MH_2}(r)\left(\frac{V_{MH_2}}{V_M}\right)^{2/3} - \gamma_M(r)\right] + E_{ads}$$

The additional term E_{ads} is related to the interaction between hydrogen and the surface atoms of the nanomaterial. The inclusion of these surface energies have a direct impact on the amount of heat released and the consequent reduction of the enthalpies of formation:

$$\Delta H = \Delta H_0 + \frac{3V_M E_{M\rightarrow MH_2}}{r}$$

Another aspect involved by the size reduction to the nanoscale and fundamental for practical applications is the kinetics of the reactions. Smaller particles lead to reduced mass transfer distances and therefore faster diffusion of species, while fast desorption kinetics are translated in good performance and fast sorption kinetics means fast refuelling. The increase of surface area increases drastically the active sites of the material, helping the hydrogen dissociation and consequent diffusion in the inner part of the material. The diffusion of hydrogen is also facilitated by the high concentration of amorphous grain boundaries. In these regions the chemical bonds that hydrogen can form are weaker favouring site-to-site hopping for hydrogen which may allow a faster hydrogenation at lower pressures.[194–196]

3.1 Nanoconfinement

The most common methods to obtain nanoparticles are summarized in Figure 18. High energy ball milling is up to now the most commonly used method to obtain nanostructured materials. However, despite the simplicity of the technique, there are several problems that occur when applied on hydrogen storage materials. The first pertains to the size limit of the grain, that can decrease to dimensions of c.a. 3-25 nm, and a relatively controllable particle size distribution.[197] Better performance, can be

achieved for some materials by applying special grinding conditions such as cryomilling or the use of solvents.[198,199] However, the good characteristics obtained by ball milling are easily cancelled out by hydrogenation-dehydrogenation cycles that lead to the re-aggregation of the particles via sintering. The nanoparticle synthesis by nucleation and growth in solution is another way to obtain particles of small and controlled dimension, but such methods are not straightforward and require precise control of the solution concentration and temperature.[200] Moreover, these methods are mostly effective for the preparation of transition metal and metal oxide nanoparticles, while the light metals commonly involved in hydrogen storage materials, are not stable in aqueous solutions while they are particularly reactive in most of the solvents. Confinement in nanosized pores is an alternative that has quite recently been investigated. In reality, nanoconfinement in a porous scaffold requires a stable dispersion of particles with dimensions of few nanometres. Nanoconfinement can affect in a significant way the physical properties of the material. First, infiltration in a limited space can afford well-defined and moreover small particle sizes, while it may limit the aggregation induced particle growth during hydrogen sorption. Particle size minimization leads to the previously mentioned enhanced characteristics of nanostructured materials for hydrogen storage as both thermodynamics and kinetics change due to nanoscaling. Furthermore, the surface contact and interaction between the hydrides and the scaffold could induce a destabilization of the hydride, with potential catalytic effects and consequent lowering of the equilibrium pressures.[201]

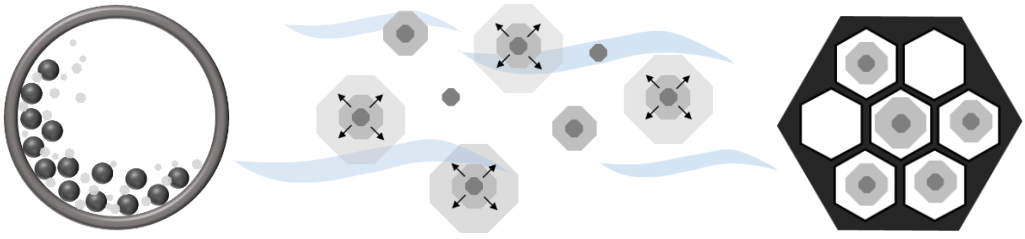

Figure 18: Schematic representation of the most common methods used in order to obtain nanoparticles for hydrogen storage purposes. Left: ball milling. Centre: particle growth in solution. Right: nanoconfinement.

This process can be implemented via two main routes: by infiltration of the hydrogen storage material in a pre-formed porous scaffold or by building the host-material around the (guest) active nanoparticles. Generally, the infiltration based nanoconfinement is

performed by introducing the hydrogen rich material or its precursor in the pores of the host via melting or after solubilizing the guest in a compatible solvent. Contrary, in the second method, the metallic species are enclosed into cavities during the preparation of the porous material.[202] However, before proceeding with the confinement an accurate study of the porous structure and its properties from the chemical and physical point of view is necessary. Among the various aspects that should be taken into account, the choice of a compatible scaffold with sufficiently high surface area and appropriate pore sizes, is of fundamental importance. Moreover, the scaffold to be used should be thermally and chemically stable under the working (hydrogen charging-discharging) conditions. Additionally, abundance, cost efficiency as well as negligible health and environmental effects are pivotal for a large-scale application. The best candidates for our purposes have to be chosen among a wide range of different materials that are available.[177,178,203] Some of them will be analysed in the following chapters.

3.2 Porous materials

Beyond zeolites and activated carbons, which have been traditionally used, the interest for porous materials has grown in the last decades while recently there is an exponential increase of new synthetic porous structures. The reason behind this trend lies in the vast number of diverse applications in different fields, such as catalysts or selective filters in the petrochemical industry, to new materials for energy storage, photocatalytic or fuel cells systems, controlled drug release processes, heat and sound insulation or waste water treatment.[204,205]

A porous solid is made of a continuous solid phase (framework) and empty space. A porous solid is characterized by the presence of a large number of openings e.g. cavities, channels or interstices having length larger than width (Figure 19).[206,207] Pores can be classified in several categories as schematically represented in Figure 19. They can for instance be “closed” (a) if they are totally inaccessible to fluids (liquids or gases); such pores influence the material density, conductivity (e.g. heat and electrical) and mechanical strength but they are inactive in mass transfer processes (adsorption, diffusion). Other structures (b, c, d, e and f) are classified as “open”, however if the pores have only one entrance (b and f) they are described as “blind” pores, while if accessible from several sides they are considered “conducting” (c). It’s also necessary not to confuse pores and surface roughness (g). Another classification is based on the pore shape, as shown in (Figure 20).[206]

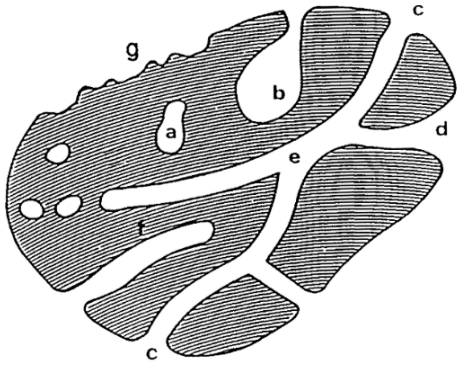

Figure 19: Schematic cross-section of a porous solid.[206]

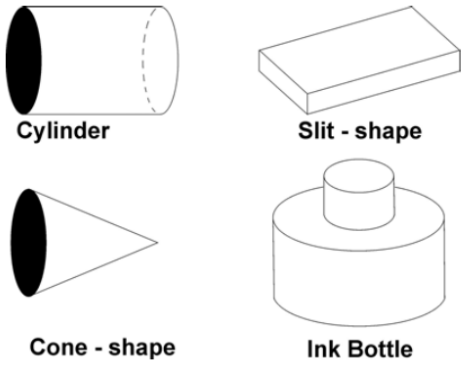

Figure 20: Schematic representation of pores shape.[208]

In order to facilitate the discussion on porous solids several definitions on pore properties are necessary: [207]

Pore volume V_p: it indicates the volume of the pores, measured with a method that must be stated.

Pore size or pore width: the distance between two opposite pore walls or the diameter if the pores are cylindrical.

Pore size distribution: is a value obtained by the derivatives dA_p/dr_p or dV_p/dr_p (dA_p/dw_p or dV_p/dw_p) where A_p is the pores wall area, V_p the volume, r_p the radius (e.g. for cylinders) and w_p the width (e.g. for slits) of pores.

Porosity, ε: it represents the ratio of the total pore volume V_p to the apparent volume $V_a = V_p + V_s$ of the material (V_s is the volume of the solid framework).

Surface area: Value indicating the total surface of the material including both the external surface area of a powder and the area of the pore walls.

The most recent classification of pores is based on their dimensions. According to IUPAC[206] porous materials are defined as:

Microporous, with pore width smaller than 2 nm.

Mesoporous, with pore width between 2 and 50 nm.

Macroporous, with pore width larger than 50 nm.

The dimensions of pores is a fundamental aspect of a porous material and as the pore size changes the functionality of the material changes. Among the materials for hydrogen storage in the following chapters microporous and mesoporous materials will be encountered. The former are mostly used for the storage of molecular hydrogen by physisoption. The latter have been used for the confinement of hydrides in the form of nanoparticles. Macroporous materials do not actually affect the confined material reactivity due to the relatively large particle sizes. For such materials, any possible change can be rather attributed to catalytic reactions due to the surface interaction between hydride and scaffold than nanoconfinement effects.

3.2.1 Microporous materials

Microporous materials, are defined as organic or inorganic porous solids with pore sizes smaller than 2 nm. The microporous family comprises activated carbons, carbon nanotubes, oxides (e.g. silicates, aluminosilicates) like zeolites, polymers of intrinsic microporosity (PIMs), covalent organic frameworks (COFs) and hybrid materials such as metal-organic frameworks (MOFs). In this kind of materials, the solid-gas interaction potentials of opposing pore walls overlap, resulting in increased attractive forces, able to keep highly volatile gasses adsorbed on the porous material surface. In some cases, the packing of the adsorbed molecules is able to reach densities similar to the liquid phase of the adsorbate.[209] Despite the high volatility of hydrogen, some microporous materials at low temperatures exert sufficient surface interactions with the gaseous molecules to store them by physisorption via van der Waals forces. Due to the weak interactions involved, the energy required for desorption is a small fraction of the heats involved in hydrides, making thus adsorption an interesting alternative approach to solid state hydrogen storage.

Among microporous solids, the carbon-based materials find an important position due to the low mass of carbon that limits the scaffold weight, the availability of carbon precursors and the great variety of structures that can be obtained. Activated carbon and carbon nanotubes are the most studied examples. Activated carbons constitute a family of porous carbons, generally obtained by carbonization of an organic precursor followed by activation via gasification at high temperature in presence of an oxidant (e.g. H_2O or CO_2).[210] With surface areas that can often be higher than 3000 m^2/g (Figure 21), at low temperatures such as 77 K and ~20 bar activated carbons can reach hydrogen uptakes between 3 and 5 wt%.[211–213] Closely related to the family of activated carbons are the carbon nanotubes, consisting in a carbon elongated cylindrical structure. However, the synthesis of single and multi-walled nanotubes is performed via arc-discharge, gas-phase catalytic growth, laser ablation and chemical vapor deposition from hydrocarbon and among these methods only the latter can be performed in a relatively large scale.[214–216]

Among the non-carbonaceous microporous materials, zeolites are the most well-known, and several studies have been performed to evaluate their potential for hydrogen storage purposes. Contrary to the carbons previously mentioned, the zeolites can be synthesized in structures with extreme regularity. However, due to their “heavier” solid skeleton their gravimetric surface areas are in general much lower (Figure 21), with maximum values of a few hundred m^2/g, leading also to low gravimetric hydrogen adsorption capacities.[209,217]

Metal-organic frameworks (MOFs) are hybrid organic-inorganic (mainly micro-) porous materials, made of metal ions or clusters connected by organic ligands in extremely regular crystalline structures. The pores and channels of MOFs are easily tuneable by varying the metal ion or the organic ligands, producing in this way a wide variety of different structures. The porosities of MOFs are often occupied by guest species, introduced during the synthesis (e.g. solvents). The removal of these species can lead to structure collapse, however, by following appropriate “activation” protocols it is possible to obtain a permanently stable porosity and guest species like hydrogen can be introduced into the network.

In order to increase the MOFs hydrogen uptake two different routes can be followed, i.e. the increase of the surface area of the material or the increase of the attractive interaction of the framework with the hydrogen molecules. MOFs with surface areas of more than 7000 m^2/g (Figure 21) and micropore volumes higher than 2 cm^3/g, have

been reported and these are significantly higher than those reported for activated carbons. However, despite the relatively large amounts of hydrogen uptake at 77K, the uptakes at room temperatures are still generally lower than 1 wt%. On the other hand, the increase of the binding forces to keep hydrogen molecules can be obtained from different ways. One possibility is related with the generation of unsaturated metal centres, while the use of ligands able to increase the affinity of the metallic site for hydrogen or to stabilize it through the action of functional groups.[51,218–220]

Similar to MOFs, the cyanometallates are porous coordination polymers of Prussian-blue type. In these materials the metal sites are coordinated by cyano groups with a geometry that in the anhydrous form leaves a vacant site on the metal, allowing easy interactions with hydrogen molecules.[221]

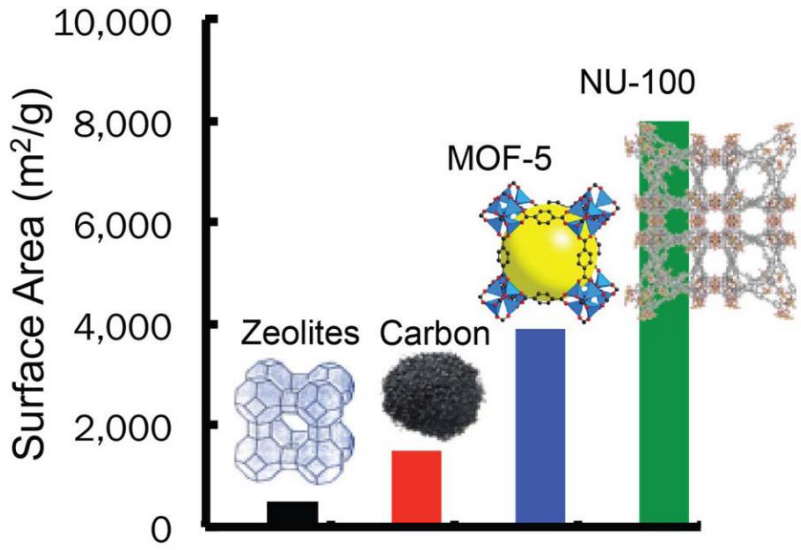

Figure 21: A surface area comparison of different microporous materials.[222]

3.2.2 Mesoporous materials

As mentioned in the previous chapters, a material may significantly change its chemical behaviour when its size is reduced to the nanoscale. This is possible by confinement in pores with a proper size (e.g. pores larger than ~3 nm) to allow facile incorporation of the guest materials but also small enough to provide destabilization effects on the confined material. For this reason, the best class of porous materials for the nanoconfinement of hydrides are the mesoporous ones.

3.2.2.1 Silica mesoporous materials

A large number of mesoporous materials are silica based; these include aerogels, xerogels with controlled porosity, Vycor-type glasses and surfactant templated mesoporous materials. Contrary to zeolites, which are crystalline, the materials mentioned above are amorphous. Aerogels and xerogels are prepared through a sol-gel process followed by aging and drying. However, the relatively large pore sizes obtained in both cases are more appropriate for other applications such as drug delivery and size-selective catalysis.[223–225] Vycor glass and controlled porous glasses (CPGs) are produced by thermally treating alkali-borosilicate glasses in order to induce phase separation to alkali borate-rich and silica-rich phases; the former is consequently leached out by acid treatment. After solubilization, the remaining almost purely silicate glass structure has an interconnected network of pores, but the total pore volume is noticeably smaller than the previously mentioned materials.[226]

The surfactant templated porous silicates have been widely studied after their discovery; these structures have been used in this thesis. This family of materials is called M41S and since their synthesis in the 1990s, many different structures of this kind have been developed.[227] A common aspect of these materials is the possibility to use supramolecular assemblies as soft templates and build silica networks around these structures which have controlled shape, dimension and spatial arrangement. After the calcination of the silica network to a solid structure, the template is removed, leaving as product a material with extremely uniform porosity. The obtainable pores can have sizes from appr. 3 nm up to tens of nanometres with different network structures and connectivities, opening the way to a large number of possible applications. Up to now these mesoporous materials do not have a systematic nomenclature and are historically named by three letters, followed by a number referred to their internal numbering system for new materials.[228] For instance the MCM (Mobil Composition of Matter) series are obtained by using cationic surfactants in alkaline pH and members of this family are MCM-41 with 2D hexagonal structure,[229] the MCM-48 with cubic[230] and MCM-50 lamellar structure (Figure 22).[231]

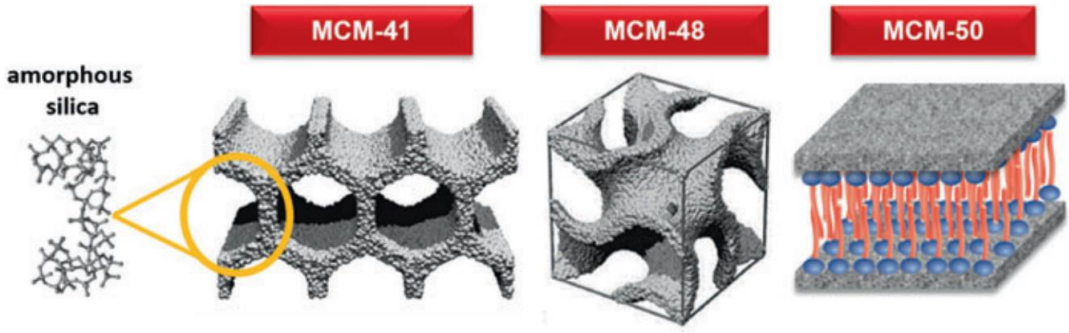

Figure 22: Members of the M41S family. MCM-41 (hexagonal), MCM-48 (cubic) and MCM-50 (lamellar). [232]

The SBA (Santa Barbara Amorphous) series includes mesoporous templated silicates obtained in acidic solution. Among these, using cationic surfactants there are SBA-1 with cubic structure,[233] SBA-2 combined cubic and hexagonal geometry [234] and SBA-3 hexagonal scaffolds.[235] Upon using block copolymers as surfactants, it is possible to synthesize the SBA-15 with 2D hexagonal mesopores,[236] which will be analysed in the next chapters, and the SBA-16 with cubic structure.[237] The MSU-X series are materials synthesized in neutral solutions with non-ionic surfactants such as polyoxyethylene oxide and develop wormlike frameworks.[238] Other series of ordered mesoporous materials are the KIT (KIT-6 has a cubic structure like MCM-48), obtained with triblock copolymers;[239] the FDU series, with cubic structures obtained with ionic or nonionic block copolymers;[240,241] the HOM (highly ordered monoliths) with different geometries, obtained with nonionic triblock copolymers in low pH solutions as template;[242–244] and FSM series, synthesized with ionic surfactants in alkaline solution to obtain highly ordered hexagonal structures.[245]

The general synthesis involves a silica source, a catalyst for the silica polymerization, a template and a solvent, usually water. Often, co-solvents with different polarity, able to modify the template behaviour and self-assembly process are also added , leading to different pore shapes and dimensions.[246]

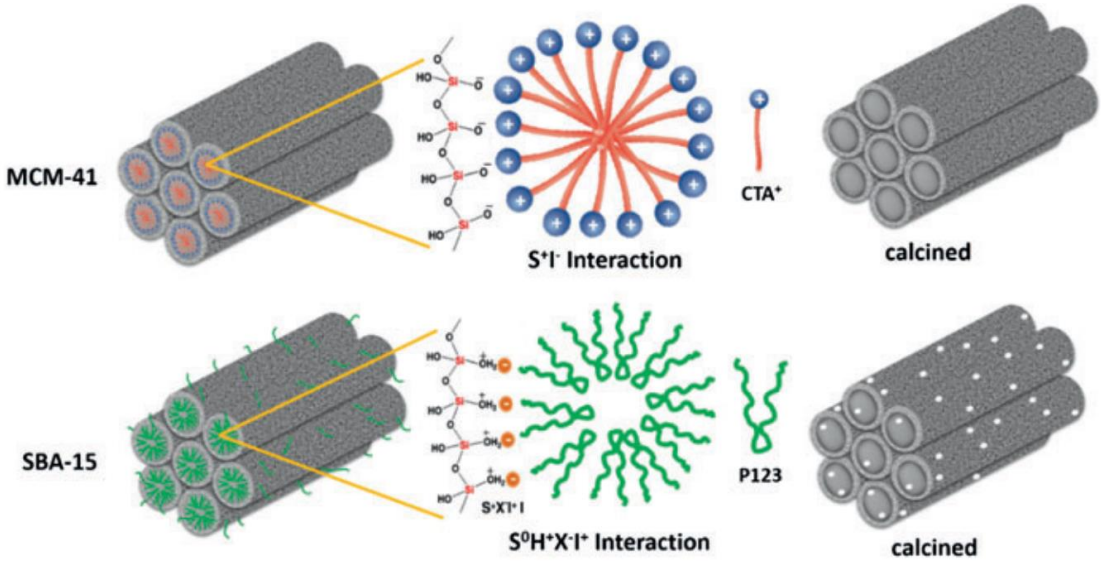

Figure 23: Electrostatic interactions involved during the synthesis of ordered mesoporous materials types MCM-41 and SBA-15.

The size and shape of the silica pores are actually determined by the size and shape of the surfactant assemblies in solution. The spatial arrangement of the surfactants in solution is due to their amphiphilic nature and the interaction of the hydrophilic and hydrophobic parts of the molecules with the solvent (Figure 23). During the synthesis process the surfactant molecules self-assembly to geometries which minimize the interactions of their hydrophobic parts with water. When the concentration of surfactant in solution is above a certain concentration, known as critical micelle concentration, stable structures are formed. These supra-molecular assemblies (micelles) are self-organized homogeneously in size and shape depending on the solution parameters, i.e. surfactant concentration, pH, temperature, strength of the surfactant interactions, ion concentration, etc.[247] These micellar structures constitute a perfect template which can induce silica polymerization, and thus solid silica structures with the same shape of the micelles can be can be obtained. The structure of the micelles in solution can be predicted either by knowing the morphologies that correspond to certain ratios among surfactant and the reactant source of silica or taking into account a series of characteristics typical of the surfactant in order to obtain a so-called packing parameter g. The packing parameter, takes into account aspects such as the hydrophobic tail volume, the hydrophilic head area and the tail length.[248–250] Generally, with the increase of the packing parameter value it is possible to observe different micellar structures in the following order: spherical, cylindrical, flexible bilayers or vesicles, planar bilayers and finally inverted micelles at higher concentrations (Figure 25).[250]

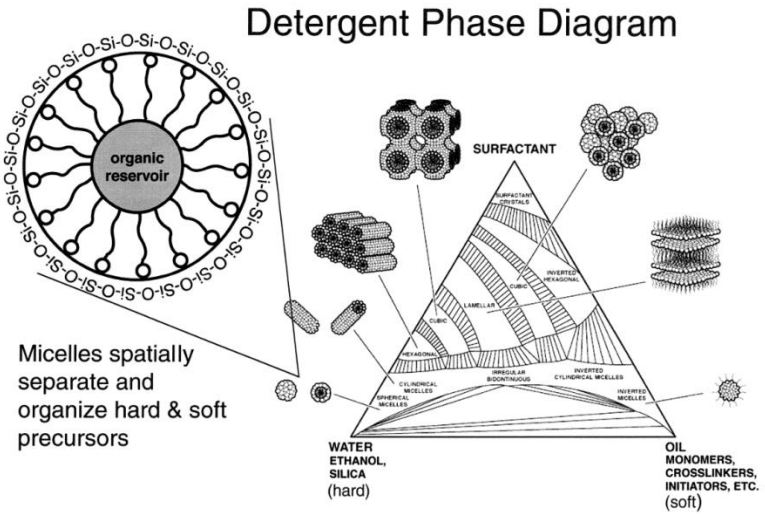

Figure 24: Schematic detergent (surfactant-oil-water) phase diagram with the introduction of hydrophobic or hydrophilic precursors.[251]

Many different types of surfactants have been used for the synthesis of mesoporous silica scaffolds. These include cationic (positive charge on their hydrophilic end), anionic (negative charge on their hydrophilic end) and or amphoteric (zwitterionic hydrophilic end, i.e. both positive and negative) surfactants as well as nonionic surfactants. The latter are actually co-polymers with regions of different hydrophilicity that can self-assemble in micelles.[252,253]

The condensation of silica around the micelles structure can be performed at different pH environments. In neutral solutions the silica condensation is often driven by the surfactant itself, acting like a catalyst. In the same pH conditions also the presence of F^- ions can drive the same polymerization reaction.[238,254,255] In alkaline or acidic conditions, the condensation reaction among the silanol groups is driven by the basic or acidic species in solution. The reaction takes place quickly at high pH and the precipitation of solid silica is observed immediately after the introduction of the silica precursor. The reaction ratio is much slower in acidic conditions, with reactions taking place at values of pH generally slightly below 2. The polymerization reaction requires some time, while further aging steps may be necessary, between room temperature and 140 °C to consolidate the silica structure and complete the silica polymerization reactions.[256] Typically, the materials prepared in alkaline conditions are based on sodium silicate solutions or colloidal sources of silica, which are cost efficient. However, with methods where silica dissolution is required, it is easy to form silica oligomers in solution, with a

negative impact on the final product. To avoid this problem, in many syntheses either in alkaline or in acidic conditions, alkoxysilanes with general formula $Si(OR)_4$ are used as SiO_2 source.[228,257]

After the polymerization of the silica around the micelles' surface is complete, it is possible to remove the template. Due to the organic nature of the surfactant and the good thermal resistance of the silica scaffold, in most of the cases the template is removed by performing calcination in air with fast heating, generally up to temperatures around or higher than 550 °C. During this process the surfactant is totally decomposed and oxidized to CO_2. However, calcination sometimes induces lattice contractions or leaves traces of residual products of decomposition depending on the kind of surfactant used. To avoid these consequences, sometimes it is preferable to extract the template, commonly through treatment with acidic solutions containing ethanol.[258] At the end of the template removal, only the silica framework remains, and the surfactant is replaced by pores. The materials obtained through the above general route have potential applications in a wide number of processes, such as catalysis due to the high surface area and possibility of easy silica functionalization (e.g. metal decoration), pollutants removal, waste water treatment and nanoconfinement, including active pharmaceutical ingredients (APIs) or hydrides for hydrogen storage purposes. In this thesis, porous silica was used as a solid template for developing porous carbons with high pore volume and surface area. In particularly, the material synthesized was SBA-15.

3.2.2.1.1 SBA-15

SBA-15 is a mesoporous silica material that belongs to the SBA family (Santa Barbara Amorphous), which was synthesized for the first time by Zhao et al. [256] in 1998. This material is characterized by cylindrical pores arranged regularly in a 2D hexagonal structure (p6mm). The pores have a variable diameter between 4 and 30 nm and a length of ~1 μm, while the silica pore walls have thickness generally between 3 and 6 nm. An additional network of micropores runs through the silica walls and interconnects the hexagonally oriented mesopores.[259] The microporosity of SBA-15 is generated by a minor overextension of the surfactant's hydrophilic chains in the solution that affords disordered pore wall percolating "pinholes" after the poly-condensation of silica and subsequent template removal. A further increase of the micropores may be due to shrinkage of the silica during calcination. The presence of microporosity is a fundamental advantage of SBA-15, because it allows the material to be used as solid

template for the synthesis of other porous materials with “inverse” SBA-15 structure. This aspect will be better illustrated during the description of the hard template synthesis of CMK-3 carbon. The microporosity also contributes to the high surface area of the material, (commonly 700-900 m^2/g) and the total pore volume (~1.1 cm^3/g).

As already mentioned, the synthesis of SBA-15 is performed in solution. The surfactant used as template is Pluronic® P-123, a nonionic amphiphilic triblock copolymer of class ABA, where A is a hydrophilic block of polyethylene oxide (PEO) and B is a block of hydrophobic polypropylene oxide (PPO). The first letter of the code name indicates the physical form of the copolymer (liquid (L), paste (P) or flake (F)), while the first one or two digits are 1/300 of the PPO block molar mass and the last digit is 1/10 of the molar mass percentage of PEO in a molecule of polymer.[260] In solution the Pluronic P-123 self-organizes in micelles with a core occupied by PPO chain blocks, which is surrounded by a corona of PEO chain blocks. The conformation assumed by the micelles is strongly dependent on the concentration of surfactant and temperature. In fact, Pluronic P-123 can assume first cubic and then hexagonal structures with the increase of the concentration above the critical micelle concentration (CMC).[261] Temperature influences the interactions between the polymer and the solution; at low temperatures the PPO is hydrated, while by increasing the temperature, PPO becomes hydrophobic initially, while at even higher temperatures it starts to stretch, leading to larger cylindrical micelles.[262] The effect of enhancing the repulsive interactions among polymer and solvent, usually driven by temperature increase, can be also achieved with the introduction of salts in solution.[263] Once the right conditions of surfactant concentration and temperature are reached they must be kept constant. Commonly the sources of silica for SBA-15 are silica alkoxides, in particularly the tetraethyl orthosilicate (TEOS). The synthesis is usually performed at very low pH, approximately pH=2, after adding HCl to the solution. In this environment, TEOS hydrolyses immediately releasing ethanol in solution but condenses slowly making the reaction more controllable.[264,265] The reactions involved are the following:[247]

Hydrolysis: $\equiv Si\text{-}OR + H_2O \rightleftharpoons Si\text{-}OH + ROH$

(fast)

Alcohol condensation: $\equiv Si\text{-}OR + HO\text{-}Si\equiv \rightleftharpoons \equiv Si\text{-}O\text{-}Si\equiv + ROH$

(slow)

Water condensation: $\equiv Si\text{-}OH + HO\text{-}Si\equiv \rightleftharpoons \equiv Si\text{-}O\text{-}Si\equiv + H_2O$

(slow)

The polymerization takes place in the aqueous solution on the hydrophilic surface of the micelles, where the heads of the surfactants can interact with the inorganic precursor electrostatically. While the silica walls are formed, the micelles assume an elongated shape and arrange in a hexagonal structure, while some protruding external chains of PEO are trapped in the solid silica, creating thus micropores upon template removal (Figures 25, 26). The amount of micropores can be modulated and reduced by hydrothermal treatment. In fact, with the increase of temperature the polymer blocks assume a less hydrophilic behaviour, leading generally also to larger pore sizes.[259]

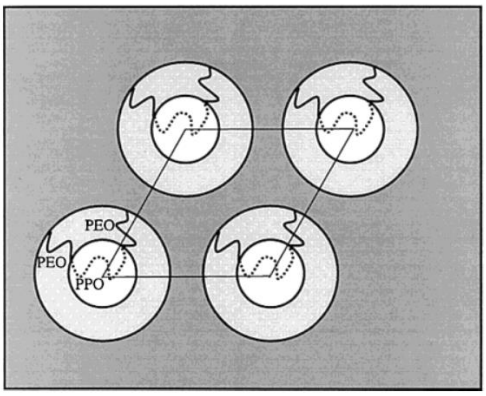

Figure 25: Schematic representation of Pluronic P-123 in uncalcined SBA-15 materials.[259]

As already mentioned in the previous paragraph for the general synthesis of mesoporous silica, the removal of Pluronic P-123 is commonly performed via calcination. During this process, the material is heated in air to around 550 °C or higher temperatures. Above 300 °C the surfactant is already decomposed while the water trapped in the structure is released. The silica structure slightly shrinks during calcination; this can be avoided by using solvents or oxidizing agents as ethanol, hydrogen peroxide or sulphuric acid.[266] After the template removal only the mesoporous silica scaffold remains.

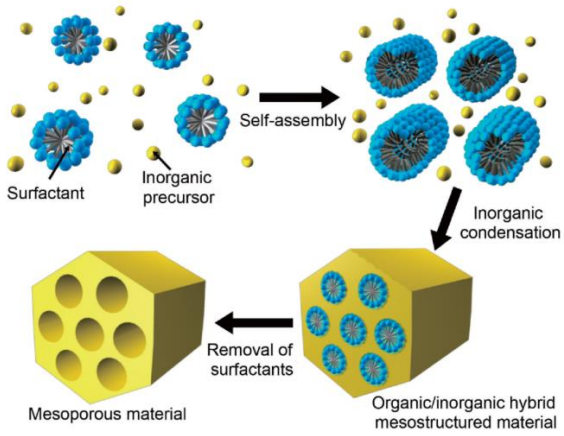

Figure 26: Formation mechanism of a SBA-15 –like structure induced by self-assembly of a surfactant in solution.[267]

3.2.2.2 Carbon porous materials

Carbon is another important material for the development of porous scaffolds. Porous carbons are interesting materials due to their unique properties, such as surface hydrophobicity, large surface areas and pore volumes as well as good mechanical, thermal and chemical stability. Due to their characteristics, porous carbons are often used in several applications such as water purification, gas separations and storage but also as catalyst supports, and high surface area electrodes.[268] Carbon materials usually contain micropores and thus are also used in handling small molecules, e.g. catalytic processes, molecular sieving and gas adsorption. Microporous carbons have been produced from carbonization of coal with organic additives, ion exchange resins and biomass, highlighting the possibility to synthesize materials with surface areas higher than 3000 m^2/g from cost efficient precursors.[269–271] An alternative synthetic approach involves the presence of a hard template. For instance, zeolites with a regular framework can be used as a host material that is filled with organic carbon precursor (by e.g. chemical vapor deposition or wet impregnation) which can be carbonized. After pyrolysis and the removal of the silica scaffold only the carbon remains, with sub-nanometre pores shaped on the walls of the zeolite, surface areas that can reach values of 3600 m^2/g and pore volumes of around1.5 cm^3/g.[272,273]

After the synthesis of the first ordered mesoporous silica via soft-templating, the development of mesoporous carbon obtained via nanocasting was a natural next step. The wide variety of different silica structures allowed for the development of several different carbon negative replicas, with surface area and pore volume similar to the

silica templates, but properties typical of carbon materials. The technique adopted is called hard template synthesis, and was used to obtain mesoporous carbons since 1999 when two research groups from Korea, Ryoo et al.[274] and Lee et al.[275] impregnated MCM-48 silica to obtain the correspondent carbon negative replica. Ryoo et al. infiltrated the silica template with a sucrose solution containing sulphuric acid, to obtain, after the silica removal, the CMK-1 mesoporous carbon (Figure 27). The CMK-1 has a cubic structure with mesopores of appr. 3 nm diameter and also a large amount of micropores, which contribute to the high surface area of ~1400 m^2/g and pore volume of ~1.4 cm^3/g, of the material.

Figure 27: Schematic representation of the synthesis of the porous carbon CMK-1 starting from the silica template CMC-48.

On the other hand, Lee et al. impregnated the Al-MCM-48 silica with implanted aluminium, and infiltrated the porous material with a phenol - formaldehyde resin. After resin polymerization, which was catalysed by the aluminium, carbonization of the polymeric carbon precursor and etching of the silica template, the SNU-1 porous carbon was obtained. The SNU-1 carbon has similar pore size with CMK-1 separated by 2 nm carbon wall pores and a surface area of ~1300 m^2/g.

Particularly important members of this family are the SNU-2 obtained from hexagonal mesoporous silica (HMS) and CMK-3 from SBA-15. The first has bimodal pores of appr. 0.6 and 2 nm, pore volume of 0.69 cm^3/g and surface area of ~1100 m^2/g.[276] The second has pores of variable diameter between 4 and 10 nm depending on the SBA-15 template, pore volume of ~1.3 cm^3/g and surface area higher than 1500 m^2/g.[277] Other examples of porous silica adopted in hard templating synthesis include MCM-41 to obtain carbon nanowires with surface area of 1400 m^2/g.[278] CMK-2 carbon obtained from SBA-1, CMK-4 from Al-MCM-48 (Si/Al = 20) and CMK-5 from just coating with carbon films the SBA-15 surface. Using the same technique several other materials were used and these include KIT-6, FDU-5, HMS, SBA-1, SBA-7, SBA-12, SBA-16,

HMS, MSU-1 and MSU-H. The source of carbon can be different, but it's always an organic precursor able to wet or fill the pores of the template as solution or through vapour deposition, while consequent pyrolysis generates a solid structure.[228,279,280] A similar method of synthesis uses as hard template dense silica instead of porous materials. This involves the use of closed (or random) packed spherical particles, in which pores form between the contacts of the spherical particles. These are again filled with a carbon source, which is pyrolyzed to create a silica-carbon composite, while the final step is removal of the silicious ceramic part. This process affords porous carbon "foams" with highly interconnected spherical pores.[281–284]

To conclude, for the hard template synthesis of carbon porous materials, a solid with controlled pore structure is required and, in most cases silica is used due to the large variety of different structures. The silica template is impregnated with a suitable carbon precursor. The introduction of the carbon source can be implemented via wet impregnation, chemical vapour deposition or a combination of both. There are several carbon precursors and usually the simpler and most economical substances are preferred; some examples are sucrose, phenolic resins, furfuryl alcohol, poly(divinylbenzene), naphthalene, acetylene, etc. Generally, the molecules introduced in the silica scaffold are initially polymerized (e.g. caramelized in the case of sucrose), in order to build a first organic framework rich in carbon, and then carbonized. The carbonization/pyrolysis is performed under inert gas atmosphere or vacuum, at high temperatures, depending on the material to be synthesized, but often between 800 and 1000 °C. The carbonization temperature has a direct effect on the atomic composition and pore arrangement of the material, as the amount of oxygen and impurities is reduced with increasing temperature. At high temperatures graphitization may occur and this in general reduces the final surface area and pore volume of the material.[268,285–287] After carbonization the template is removed via solubilisation. The chemical agent used in most of the cases is hydrofluoric acid (HF), which is able to attack the hydrated silica and remove it from the framework as silicon tetrafluoride according to the following reactions:[288]

$$SiO_{2(s)} + 2H_2O_{(l)} \rightarrow Si(OH)_{4(aq)}$$

$$Si(OH)_{4(aq)} + 4HF_{(aq)} \rightarrow SiF_{4(g)} + 4H_2O_{(l)}$$

$$SiO_{2(s)} + 4HF_{(aq)} \rightarrow SiF_{4(g)} + 2H_2O_{(l)} \quad \text{overall reaction}$$

However, due to the high risks related with the use of HF, the use of sodium hydroxide is sometimes preferred. The action of NaOH is much less effective than HF and has slower etching rates that may correspond to the need of more elaborate material treatment to completely eliminate the silica. The reaction involved is the following hydrolysis reaction:[289]

$$Si\text{-}O\text{-}Si_{(s)} + H_2O_{(l)} \rightarrow 2SiOH_{(aq)}$$

After the silica removal, only the carbon scaffold remains with the space previously occupied by the silica template as the empty space of pores.

Another way to obtain mesoporous carbons involves a “soft-template” synthesis approach (Figure 28). This technique, instead of using solid materials as molds, targets the direct synthesis of the carbonaceous scaffold by exploiting the self-assembly of the carbon precursor, often assisted by a surfactant.

The one-step synthesis allows a more efficient production of mesoporous carbons, with the possibility to tune the shape and size of the pores during the material production. Moreover, the possibility to avoid the use of a silica template reduces the cost, the time of preparation and avoids high risk processes like the silica solubilisation with HF or high concentration NaOH.

The firsts works of Liang et al.[290] and Zhao et al.[291] reported the direct synthesis of highly ordered mesoporous carbon through the carbonization of resorcinol-formaldehyde resins and self-assembled block copolymers.

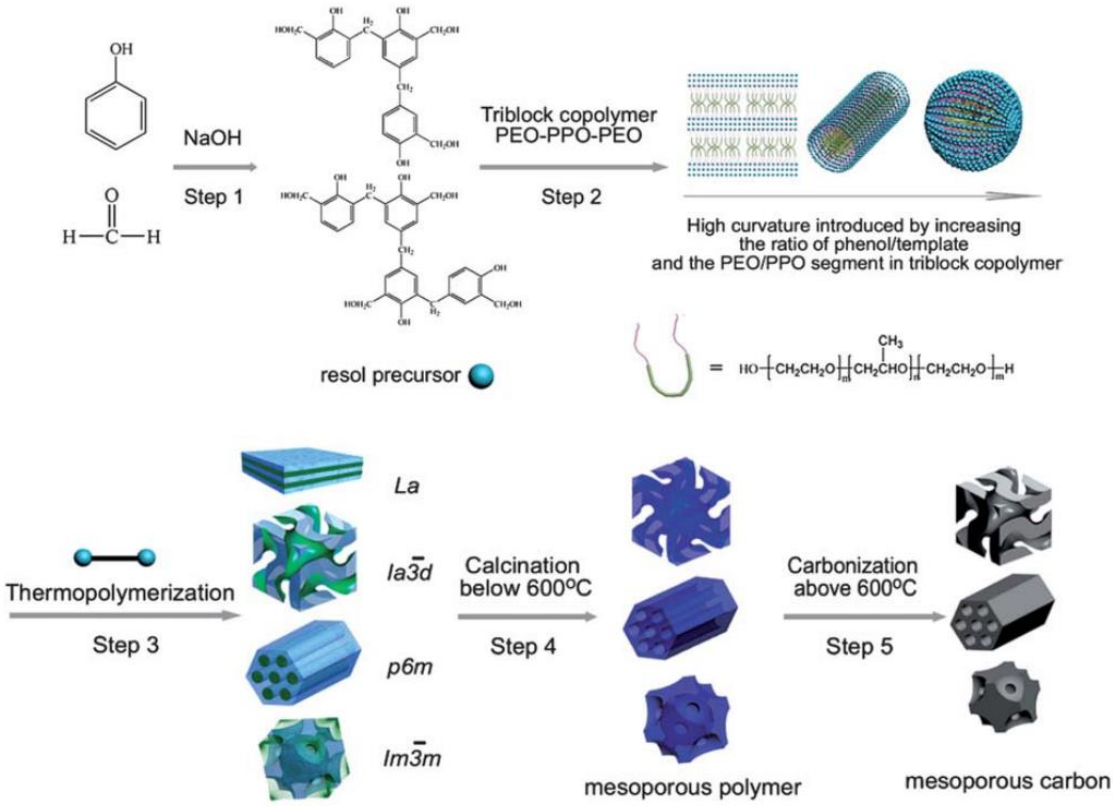

Figure 28: Representation of the preparation of mesoporous carbons from ordered mesoporous polymeric resins. [286]

Block copolymers that can self-assemble in regular structures can be used for the direct synthesis of soft templated carbons. However, due to the limited cross-linkage of the organic structure, it is difficult to preserve the organized structure of the polymer, because of the massive loss of carbon and volatile species during the carbonization process. For this reason, carbon sources that can be highly cross-linked are widely used, the most common being resorcinol-formaldehyde or the phenol-formaldehyde resins. Even though the rigid polymers obtained by resins can retain their structure during carbonization, they cannot self-assemble efficiently in solution. Therefore, resins are often associated to copolymers able to organize themselves in solution during the polymerization and cross-linking of the carbon precursor. The soft template (co-polymer based) decomposes much easier that the highly cross-linked polymer (resin based) under heat treatment and is thus removed during the carbonization step.[291–294]

Several synthetic methods to allow the polymer self-assembly in porous structures have been explored. The most commonly used are the EISA (Evaporation Induced Self Assembly), the dilute aqueous route, the synthesis with a macroscopic phase separation and the hydrothermal autoclaving process. The EISA method generally

involves a precursor of reticulate polymers (phenol, resorcinol, phloroglucinol-formaldehyde) with surfactants and low vapour tension solvents. Gradual evaporation of the solvent and the consequent increase of the interactions among solvent and surfactant, leads to the assembly of the polymer precursor which is then carbonized (Figure 29). The products obtained by this technique are often films or powders.[251,295,296]

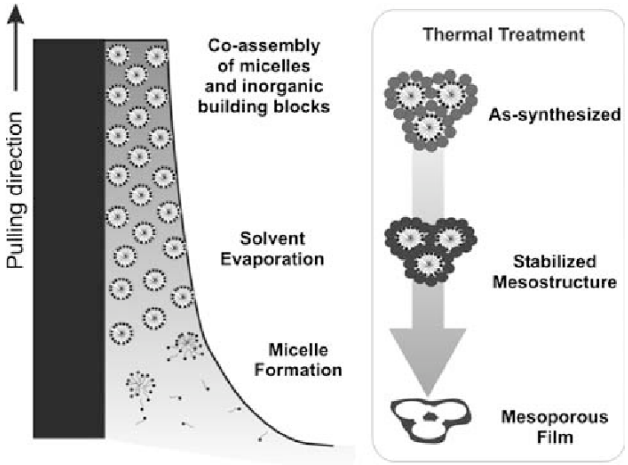

Figure 29: Left: scheme of the Evaporation Induced Self Assembly process. Right: evolution of the pores with the thermal treatment.[297]

However, the need of large surface spaces to allow the solvent evaporation is a limiting factor for the synthetic upscaling. The dilute aqueous route overcomes the EISA limit by promoting surfactant/polymer precursor self-assembly in solution, however without the need of evaporation. The surfactants used are often the already mentioned Pluronic block copolymers, that are able to generate micellar structures where the oligomeric resins can be polymerized.[298] Similar to this method is the so-called macroscopic phase separation method. Following this synthetic route, the self-assembly mixture of polymer precursors and surfactant is treated in a solution containing water and ethanol. When polymerization progresses, it is possible to distinguish a separation between a polymer-rich phase and the solvent.[298,299] On the other hand the hydrothermal autoclaving process can be used to develop monolithic polymers and carbons (Figure 30). This method is characterized by a great control of reaction pressure and temperatures, allowing fast and energy efficient synthesis. The reaction, usually performed in autoclave, involves also in this case polymer precursors such as phenol/formaldehyde or resorcinol and a surfactant, usually block copolymer in a limited amount of solvent.

The autoclaving treatment leads to monolithic and regularly structured polymers, that also in this case can be carbonized to obtain a monolithic porous carbon.[298,300,301]

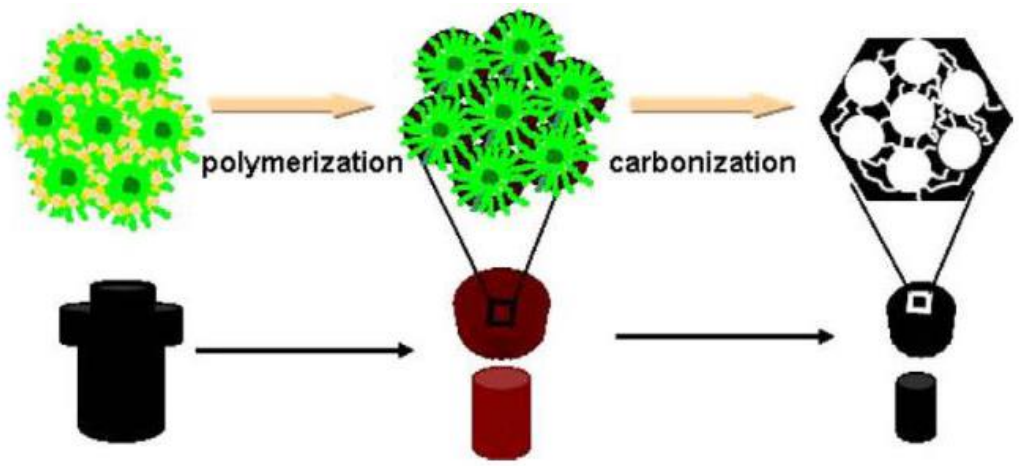

Figure 30: Microscopic and macroscopic evolution during the synthesis of a monolithic porous carbon.[301]

3.2.2.2.1 CMK-3

CMK-3 is a mesoporous carbon that belongs to the CMK-n series, an acronym created by the developer (Carbon Mesostructured by Korean Advanced Institute of Science and Technology).[302] This material, synthesized for the first time by Ryoo et al. in 2000,[303] is obtained via carbon nanocasting, using the porous SBA-15 silica as solid template (mold). The resulting material has a carbon framework that is the inverse replica of the silica, since by filling the SBA-15 silica with carbon it is possible to obtain a series of amorphous carbon rods, of diameter approximately 7 nm. Moreover, the typical microporosity of SBA-15, allows the formation of carbon nano-strands, able to connect and hold the main carbon rods in place. The regular arrangement of the rods generates a 2D hexagonal pattern (p6mm) with pores of diameter appr. 5 nm, arranged like a honeycomb. The large number of pores contributes to the extremely high total pore volume of ~ 1.3 cm^3/g and surface area of ~ 1500 m^2/g. These characteristics can be adjusted by changing the pore size of the silica template.

As already mentioned, the synthesis of CMK-3 is implemented by a so-called hard template synthesis, where the carbon scaffold is built on a solid silica structure, in our case the SBA-15 (Figure 31). In this process, the porous silica is impregnated with a carbon precursor, generally sucrose, solubilized in an aqueous solution in presence of

sulphuric acid as catalyst. When in the silica pores, the sucrose is induced to polymerization (caramelization) by increasing the temperature at ~100 °C and 160 °C. The structure obtained is then consolidated by pyrolysis under inert atmosphere at ~ 900 °C. In these conditions the carbon framework is totally formed, but still embedded in the silica structure. The removal of the template is performed via solubilisation of the silica with aggressive agents as HF or concentred NaOH. Due to the narrow porosity a meticulous treatment is necessary for complete removal of silica.

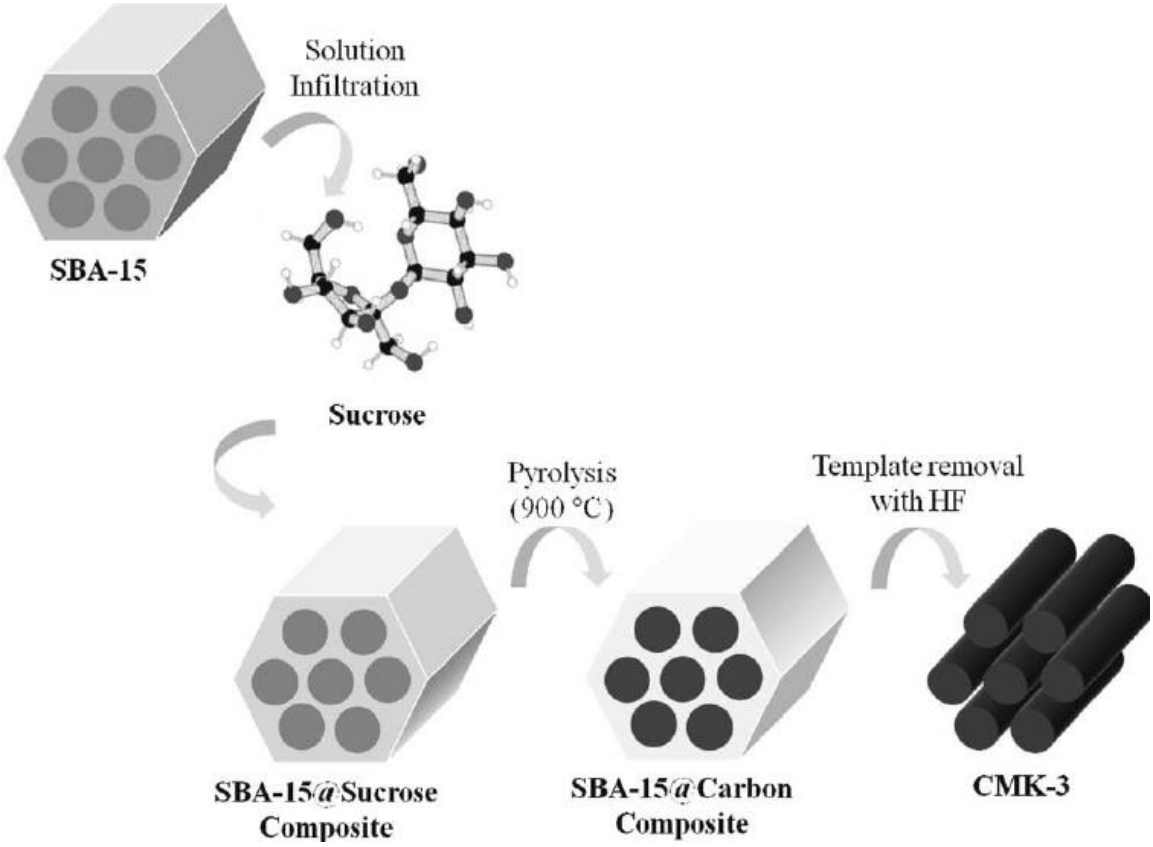

Figure 31: Description of the steps involved in the synthesis of CMK-3 via hard templating starting from SBA-15.[304]

3.2.2.2.2 Carbon Aerogel

Carbon Aerogels are a wide family of carbons characterized by a highly porous structure (up to 90-99% porosity), having however a stable 3D structure that does not collapse.[305,306] The high porosity gives to these materials a series of properties including very high pore volume, high surface area, electrical conductivity, low thermal conductivity and acoustic insulation properties. In this respect such materials are

exploitable in several applications such as energy storage and catalytic processes, adsorbents and insulators. [305]

Since Pekala developed the first aerogel obtained by polycondensation of resorcinol with formaldehyde in 1989, the synthesis and use of these materials expanded fast. [305,307,308] This is because the direct synthesis of the carbon, without intermediate use of a solid silica template, reduces drastically the synthesis time of the material, the production costs and the need of special measures for the disposal of harmful by-products. Particular attention should be given to the fact that for aerogels the use of HF or highly concentrated NaOH, which are necessary for the solubilisation of silica template, and are particularly dangerous is completely avoided.[303] It should also be mentioned that apart from resorcinol - formaldehyde other carbon sources have been used as precursors. These include agricultural waste,[309] paper and fabrics,[310] or other polymeric materials.

According to the general procedure for the synthesis of carbon aerogels from a resorcinol – formaldehyde resin, three main steps are necessary: polymerization, drying and finally carbonization (Figures 32, 33).

Polymerization occurs in different stages and is usually carried out in aqueous solution, at temperatures lower than 100 °C.[311] The first step is the addition of hydroxymethyl groups derived from the formaldehyde to the aromatic rings of the resorcinol and is followed by the condensation of the functionalized rings. The aggregation continues through a 3D crosslinking reaction that consolidates the structure. The reaction is carried out in the presence of an alkali catalyst; Na_2CO_3 is commonly used. [312,313]

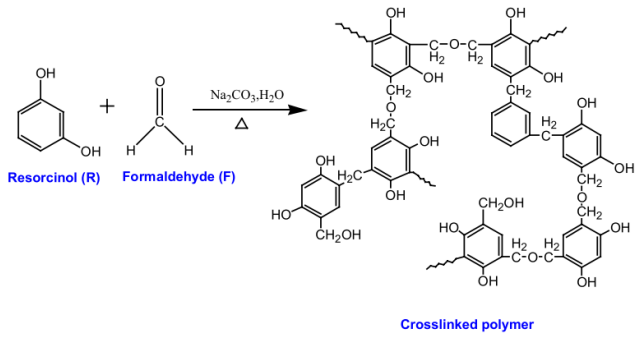

Figure 32: Reaction between resorcinol and formaldehyde, used for the synthesis of carbon aerogels.[314]

In the gel state, the polymeric framework is filled by the solvent, the removal of which leads to the formation of the aerogel. This step is often preceded by a solvent substitution treatment in order to pass from an aqueous solvent to an organic one,

which is easier to remove.[314,315] Drying can be carried out through three main processes: supercritical drying, freeze drying and ambient temperature drying.[316–318] The last phase of the preparation is the pyrolysis of the sample. Usually, pyrolysis is carried out by heating the sample at high temperatures between 600 °C and 2100 °C under inert gas flow, commonly N_2 or Ar. During this stage of the synthesis most of the functional groups containing oxygen, nitrogen and hydrogen are removed as volatile species and there is an increase of the amount of micropores and therefore an increase of the surface area as well. The carbonization induces an overall shrinkage of the material, reducing the amount of macropores in favour of mesopores and micropores.[314,319]

The obtained carbons have a three dimensional highly interconnected, disordered porous network. The pores are obtained by the interstices between fused carbon spherical primary particles, which stem from the polymeric clusters that are generated in solution.[308] Surface area and total pore volume can have quite different values among different aerogels, however, typically they are relatively high; for instance the carbon aerogel adopted during the work of thesis had a surface area of 760 m^2/g and total pore volume of 1.36 cm^3/g, with average pore size of 25 nm.

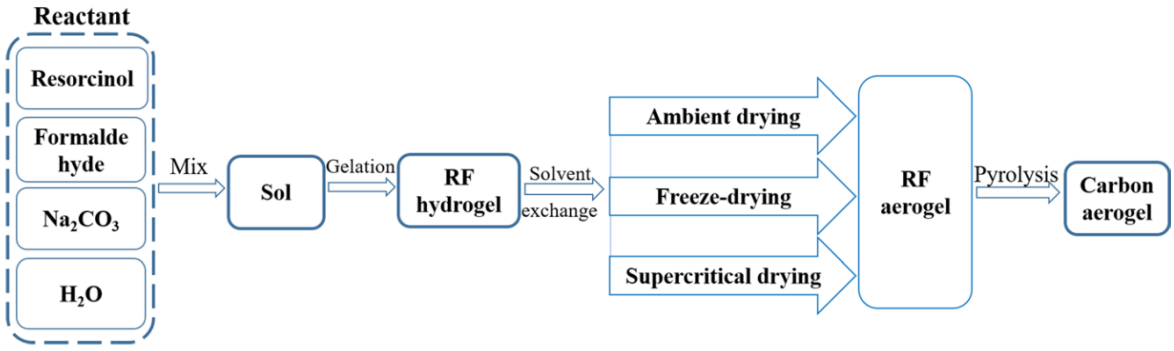

Figure 33: Synthetic procedure for the production of carbon aerogels.[314]

CHAPTER 4
EXPERIMENTAL PART

The preparation and study of the materials that were investigated in this work involved a wide range of synthesis and characterization techniques. In particular, due to the biphasic nature of the composites, separate efforts had to be made to synthesize the active phases (borohydride mixtures) and the carbon scaffolds and then to create the composites through the nanoconfinement process, via melt infiltration.

4.1 Glovebox and inert atmosphere handling

Due to the high reactivity of hydrides with air and the easy formation of oxides, all the handling was performed under inert atmosphere, either in a glovebox (with O_2 and H_2O concentrations <0.5 ppm) or in sealed reactors. Most of the sample handling was performed in MBraun LABstar gloveboxes (Figure 34) at National Centre for Scientific Research (NCSR) Demokritos (Athens) and Aarhus University (Denmark) as well as at the Helmotz Zentrum Geesthacht (HZG) laboratories (Germany), under similar parameters in an argon atmosphere. MBraun gloveboxes are equipped with a gas circulation system, for the constant purification of the argon atmosphere. More specifically, the argon is passed through filters and getters to trap O_2 and H_2O and keep their concentrations below <0.5 ppm. Similarly, activated carbon traps for the solvents are used. The filters and getters are regenerated periodically and the quality of ambience is continuously monitored by specific detectors.

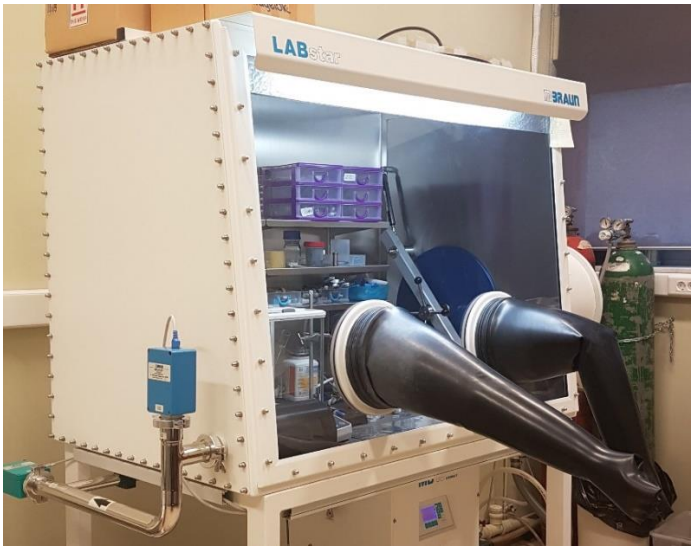

Figure 34: MBraun LABstar glovebox at NCSR Demokritos.

To transfer the samples outside the glovebox it is always necessary to hermetically seal them in plastic or glass sample holders, while the same protection from the external atmosphere must be maintained also during the processing and analysis of the materials.

Therefore, when inserting the samples to the reactors, a wide series of different gaskets and flanges must be used, varying from stainless steel and graphite for high temperature treatments to nickel and Teflon for room temperature treatments. More details of the processes are described in the following paragraphs.

4.2 Mechanical milling

Mechanical milling is one of the most common treatments used in the field of nanomaterials for solid-state hydrogen storage, as well as for the development of new composite materials and metal alloys. The method involves the introduction of the materials into a rotating cylindrical chamber with a set of hard spheres (balls) (Figure 35).[198,320,321] The container and the balls can be made of a wide variety of materials including hardened steel, stainless steel, tungsten carbide, zirconia, silicon nitride, or methacrylate and the choice is directly dependent on the material to be milled. The chamber is usually sealed in an inert atmosphere, however, as will be explained in the following chapters, processing in a reactive atmosphere is also possible, with the milling energy being used to promote the gas-solid reaction. In these cases, containers with one or more valves are used to allow either the introduction of gas or the evacuation of the system. The container is generally filled to about 50% and moved by a “high energy” mill in order to create collisions both between the spheres and the chamber and between the spheres themselves. The ball-to-powder ratio depends on the processing and affects the milling time. The most common ratio used is 10:1 but a much higher ratio, even 100:1, can also be used. During this process the kinetic energy is transferred to the milled material, breaking the structure in small particles, mixing the different components and in high-energy treatments, creating new alloys from the starting reactants. The mechanically treated grains generally have sizes on the order of micrometres or nanometres. Especially for the second case, where the particles are extremely small, the materials can be considered as textureless polycrystals.

Figure 35: Fritsch Stainless steel jar for planetary ball milling with stainless steel spheres inside.

The possibility of obtaining such small particle sizes has made this technique interesting also in the field of hydrogen storage research, however, the small particle sizes are not maintained during repeated hydrogen uptake and release due to re-aggregation phenomena. Planetary mills, SPEX mills and vibratory mills are the most widely used mills in laboratories, while attritor mills are used for grinding large amounts of materials. In a planetary ball mill, the container rotates on a disk or balanced arm on its own axis and in the opposite direction at several hundred rotations per minute. This motion causes the grinding balls to run against the walls of the container. The movement is different in the SPEX or shaker mills, where the jar is shaken along the longitudinal and vertical axis, performing an “∞” (infinite or eight) motion creating high energy impacts of the balls on the top and the bottom of the vial (Figure 36).

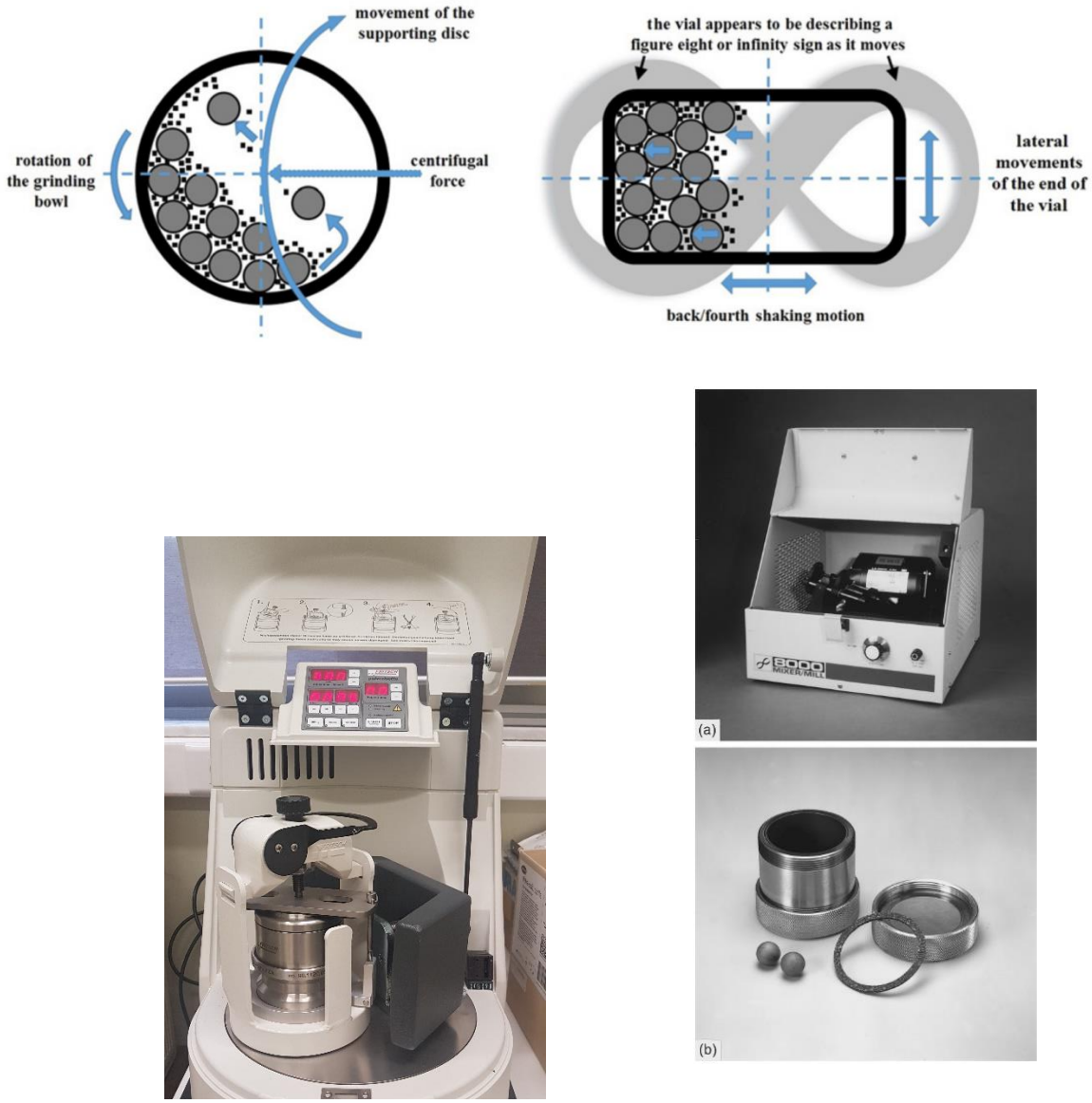

Figure 36: Principle of operation of planetary ball milling (top left) and SPEX ball milling (top right).[321] Planetary ball mill with jar (bottom left). SPEX mill (a) and tungsten carbide jar with spheres (b) (bottom right).[198]

Generally, milling can take from a few to several tens of hours, however, in this work, a milling time of minutes was sufficient for the purposes of our mixing case. This is because the high energy of the treatment easily increases locally the temperature of the system, potentially leading to undesired reactions. Temperature rise, vacancy generation, and movement of high-density grain boundary planes contribute to element interdiffusion and phase mixing. During the collisions, the powders are subjected to high energy impacts of several GPa in the planetary mill, lasting a few µs. With these conditions it is possible to induce reactions that are otherwise not attainable with other techniques.

4.3 High temperature and pressure resistant reactors/melt impregnation devices

The preparation of the composite materials via melt infiltration, as well as the hydrogenation/dehydrogenation cycles, required devices able to resist extreme conditions of high temperatures and pressures. The infiltration with borohydrides and the following hydrogenation-dehydrogenation cycles were performed on a custom-made device, also used for the sorption experiments, at the premises of NCSR Demokritos.

The experiments involving the infiltration of borohydrides into carbons, as well as the heat treatments to study the sorption capacities of the materials were performed in a stainless-steel reactor able to withstand temperatures above 500 °C and hydrogen pressures higher than 200 bar. The reactor was connected to a custom-made Sievert's apparatus to evaluate the gas released and absorbed during the treatments. Measurements with this device are based on Sievert's method, in which the amount of gas exchanged by the sample is calculating from the pressure changes in a known volume. The system consisted of a stainless-steel reactor containing the sample, usually in a quartz sample holder and covered with quartz wool, to prevent the elutriation of powders (Figure 37). The cylindrical body of the reactor was welded with a Swagelok VCR type gland, allowing multiple connection and disconnection of the reactor to the body of the instrument via a metal gasket.

Figure 37: 3D model of the stainless-steel reactor used to perform the borohydride infiltration into the carbon scaffolds and the sorption cycling experiments on the samples.

All the pipelines were connected with stainless steel VCR fittings. The sample chamber of the reactor was separated from the system by a porous flange, with a stainless-steel filter, in order to allow gas transfer but keep all the fine powders of the sample in the reactor avoiding any kind of contamination along the pipelines of the instrument. The

reactor was connected through a manifold to the helium and hydrogen gas lines as well as to a vacuum pump. The piping system also included a connection to a pressure gauge and an auxiliary chamber of known volume. All the parts of the manifold, including manometer and heaters, were contained in a stainless-steel case, externally covered with insulating material and thermostated at 30 °C with air circulation and a heating system regulated by a PID-type temperature controller (Figure 38). The pressure was monitored by an MKS type Baratron (870B) manometer with a working range between 20 psia and 3000 psia (~1.38 bar – 206.84 bar absolute pressure) and accuracy 1% of measurement.

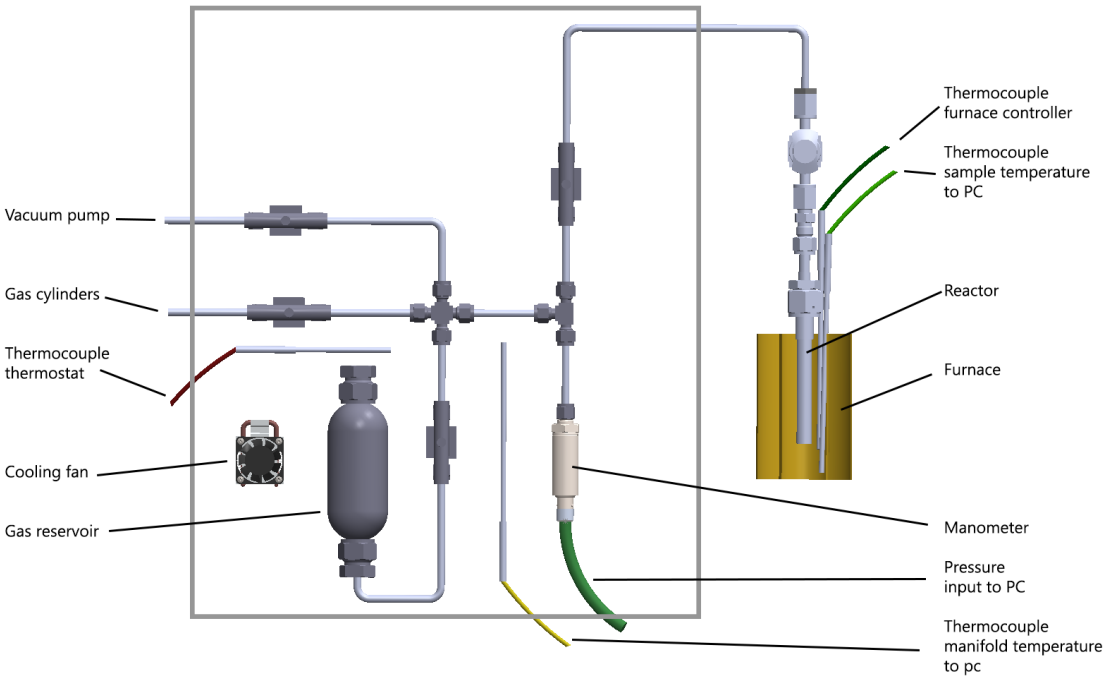

Figure 38: 3D model of the Sievert apparatus used to determine the amount of gas exchanged during the sorption cycles by the samples.

The pressure and temperature signals detected by the instrument were read and recorded on a computer through a specially developed LabView program. The device compartments were separated by HiP (High Pressure Equipment) taper seal needle valves, able to provide good control over the gas flow during the experimental phases. Evacuation was performed with a Pfeiffer HiCube turbo pump system equipped with a full scale vacuum gauge. The reactor was attached to a custom-made furnace able to

reach temperatures higher than 700 °C, which is made of a metal cylinder that fits perfectly with the reactor, contains a heating element and is externally thermally insulated by ceramic wool. The reactor temperature was constantly monitored by a thermocouple in contact with both the reactor and the furnace. The power supplied to the furnace was monitored by a PID controller, with the aid of a thermocouple located in the furnace and a safety (watch-dog) thermocouple. For safety and thermal insulation reasons, the reactor and furnace were covered by an insulating vest filled with ceramic wool.

4.4 Preparation of $LiBH_4$ – $NaBH_4$ and $LiBH_4$ – KBH_4 eutectic mixtures

The synthesis of the two eutectic mixtures of borohydrides was performed in the laboratories of the University of Aarhus and the laboratories of INano (Denmark), under the supervision of Prof. Torben R. Jensen. The $LiBH_4$ – $NaBH_4$ mixture was prepared starting from the pure borohydrides: $LiBH_4$ (Sigma-Aldrich 95% purity grade) and $NaBH_4$ (Sigma-Aldrich 98% purity grade). The two components were mixed together using the eutectic molar ratio of 0.71: 0.29 (with a melting temperature of 216 °C). The mixing process was initially performed manually, with a pestle and mortar and then by ball milling. The powder milling was carried out in an 80 ml tungsten carbide vial of a Fritch P4 planetary mill with spheres of the same material as the container. The powder to ball weight ratio utilized was 1:30, using 10 mm diameter spheres. The grinding/mixing treatment of the two borohydrides was supposed to be 1 hour long. However, in order to avoid chemical reactions due to an excessive increase of the temperature in the milling vessel, the full milling time was divided into shorter treatments. The sample was then milled in a 2 minutes session at 350 RPM, followed by a 2 minutes pause to allow the sample to cool down, and the program was repeated 30 times. As already mentioned, due to the high susceptibility to oxidation, all the handling processes were performed under inert atmosphere. The mixture was analysed as prepared through powder XRD analysis and o-$LiBH_4$ and α-$NaBH_4$ were detected.

Following a similar procedure, a second borohydride eutectic mixture was prepared, consisting of $LiBH_4$ and KBH_4, with a melting temperature of 105°C. As in the previous mixture, the preparation starts from the pure borohydrides $LiBH_4$ (Sigma-Aldrich 95% purity grade) and KBH_4 (Sigma-Aldrich, 97% purity). The two salts, in the form of a white fine powder, were mixed in a molar ratio of 0.72: 0.28 $LiBH_4$ – KBH_4, first manually and then mechanically. The ball milling was performed using the same

instrument, with an 80 ml tungsten carbide jar, and the same powder to balls weight ratio of 1:30. Also in this case the full mixing process was divided in short milling sessions in order to keep the temperatures low. The powders were milled for 5 minutes at 400 RPM, with a 2 minutes pause, and the process was repeated 48 times making the total treatment to last 240 minutes. Also in this case, all the handling was carried out under inert atmosphere. At the end of the mixing, X-ray powder diffraction analysis was performed, revealing the presence of $LiBH_4$, KBH_4 and $LiK(BH_4)_2$.

4.5 Hard templating synthesis of porous materials

4.5.1 Synthesis of SBA-15

As already mentioned, SBA-15 is the porous silica scaffold used as a solid template for the preparation of the carbon used for the nanoconfinement of the hydrides. The synthesis used in this work was based on the original synthesis developed by Zhao et al.[253] with some modifications that gave overall better performance for our case (Figure 39). In order to prepare approximately ~1 g of SBA-15, at first it was necessary to prepare an acidic aqueous solution with a surfactant. The solution was obtained by adding 16.4 ml of HCl (37% m/m) to 150 ml of water in which 2 g of the anionic surfactant Pluronic P-123 (Sigma-Aldrich) had been dissolved. After this stage, two different experimental routes were tried, both leading to SBA-15 with the same properties. In the first method, the solution was maintained under constant stirring for the entire synthetic procedure and solvent evaporation was avoided by a condenser. The temperature of the solution containing the surfactant was increased up to 40 °C and 5 ml of TEOS (Tetraethyl orthosilane) were added. The solution changed colour, from transparent to milky white. The same stirring and thermal conditions were kept for 24 hours. After one day the temperature was increased to 100 °C while keeping the solution under stirring. After the two-day reaction in solution, SBA-15 could be filtered.

The second method, also adopted for the upscaled synthesis yielding quantities up to three times higher than the original procedure, involved a hydrothermal reaction that took place in a Teflon autoclave without constant stirring. The acidic solution containing the Pluronic P-123 surfactant was heated to 35 °C and kept under regular stirring. 5 ml of TEOS were added to this solution, and as in the first method the solution acquired a milky white colour. The solution is kept at 35 °C under constant stirring for 2 hours. After this time the solution was transferred into an autoclave and left at 35 °C in an oven for

24h. The next day the temperature was increased to 100 °C. As in the first method, after two days of reaction in solution, SBA-15 was ready to be filtered. The filtration of the solid product of synthesis was performed under vacuum with a Buchner filter. The solid was washed with water to remove the excess surfactant and then dried. The polymeric surfactant was totally removed by subsequent calcination in air. The thermal treatment was usually performed with a heating ramp of 5 °C/min up to 600 °C and this temperature was kept constant for 6 hours. During this process all the organic residues from the surfactant decomposed into CO_2 and the water evaporated, leaving only the silica structure with empty pores. From the typical synthesis, in which 5 ml of silica precursor (TEOS) are used, ~1.1 g of SBA-15 is usually obtained.

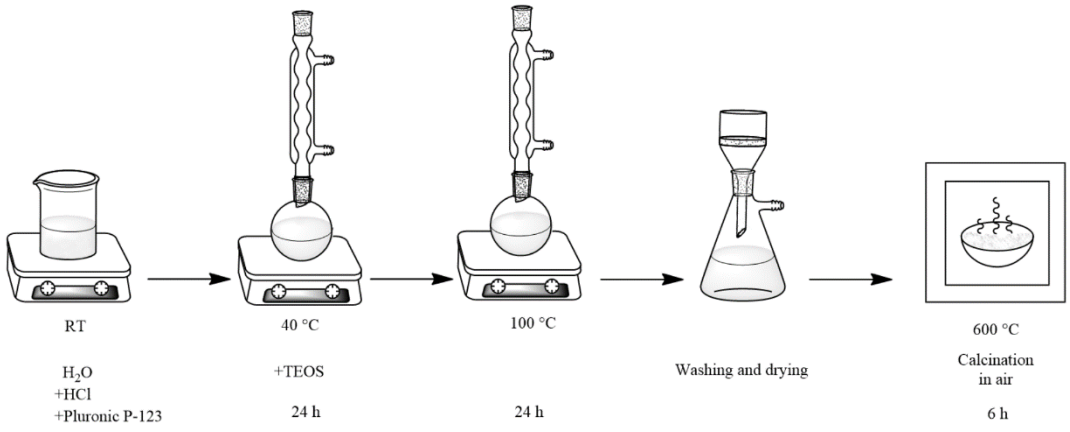

Figure 39: Steps for the synthesis of SBA-15.

4.5.2 Synthesis of CMK-3

The hard templating method and specifically the synthesis of CMK-3 type ordered mesoporous carbon have already been explained in the previous chapters. In particular, the experimental procedure adopted to synthesize the CMK-3 material was based on the original work of Ryoo et al. with some modifications (Figure 40). Scaling up of the synthesis (typically based on 1 g of SBA-15 as the starting template) was also possible, for larger and faster production of carbon that was revealed to have the same properties as the carbons resulting from the lab-scale production. Typically, 1 g of SBA-15 was subjected to three impregnations with a solution containing the carbon precursor, and each infiltration was followed by a carbonization treatment. The carbon precursor used

was sucrose, dissolved in water in the presence of sulphuric acid as the polymerization catalyst.

During the first impregnation, an aqueous solution prepared from 1.25 g of sucrose dissolved in 5 ml of water containing 0.07 ml of fuming H_2SO_4 was added dropwise onto the SBA-15, in order to wet all the powder. The soaked powder was then placed in an oven, heated up to 100 °C at a rate of 10 °C/min, under air and held at this temperature for 6 hours. Subsequently, the temperature was increased to 160 °C at the same heating rate and the sample was left overnight to be partially carbonized at this temperature. The second impregnation was performed following the same procedure with the difference that the solution with the precursor consisted of 0.8 g of sucrose, dissolved in 5 ml of water, containing approximately 0.05 ml of H_2SO_4. Also in this case the solution was added dropwise onto the SBA-15 powder, which was already black/brown at this stage of the synthesis. The subsequent thermal treatment was the same as the one used after the first impregnation (i.e. 100 °C for 6 hours and 160 °C overnight). For the third impregnation the procedure was the same but the reactants contained in the impregnating solution were further reduced: 0.5 g of sucrose dissolved in 5 ml of water with ~0.03 ml of H_2SO_4. The thermal treatment was the same as that adopted in the previous two stages. After the impregnation – carbonization treatments, the SBA-15/carbon composite material was pyrolyzed in order to stabilize the carbon structure. The pyrolysis was performed in a tubular furnace at 900°C for 6 hours, under a constant flow of inert gas. At this stage of the synthesis the product is actually a composite material consisting of SBA-15 and CMK-3. The removal of the silica template was performed by dissolving the material with hydrofluoric acid (Sigma – Aldrich conc. 40%). Due to the strong exothermic reaction of HF with silica the procedure was performed in Teflon vessels and the acid was poured onto the silica/carbon composite slowly with a Teflon pipette. Once the composite was covered with HF solution, the vessel was loosely closed and left under magnetic stirring for at least 3 hours in order to fully dissolve the silica scaffold. The removal of the acidic solution was performed in a first step through a series of centrifugations (15 minutes at 9000 RPM), removal of the supernatant and addition of water in order to dilute the remaining acid. After centrifugation, the material was filtered under vacuum with a Buchner funnel, washed first with copious amounts of water and then with ethanol. After washing, the carbon was dried in an oven at 120 °C overnight. From 1 g of SBA-15 usually 0.6 - 0.7 g of CMK-3 were obtained.

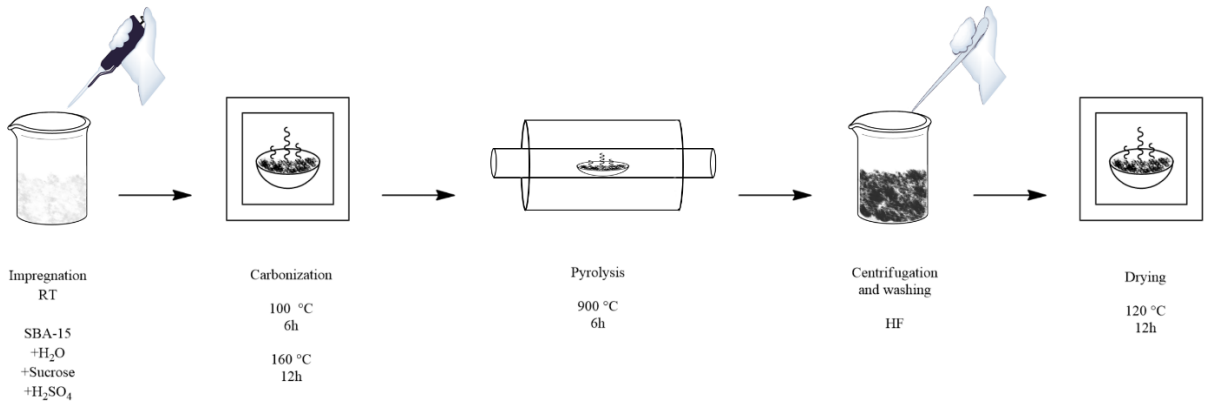

Figure 40: Steps for the synthesis of CMK-3.

For the purposes of our study, the carbon surface should be as “clean” as possible of functional groups, which are potentially generated by the several chemical treatments and which may react with hydrides. For this reason, the material was further heat treated at high temperatures under inert atmosphere. More specifically, the carbon was heated to 700 °C at a heating rate of 10 °C/min and remained at this temperature for 3 hours.

4.6 Synthesis of the composite materials

4.6.1 Carbon - $LiBH_4$ /$NaBH_4$ (LiNa) composite materials

The preparation of the composite materials LiNa/Carbon was performed in a heated stainless-steel reactor connected to a Sievert apparatus, described in the previous paragraphs. In order to investigate the nanoconfinement effect versus the catalytic effects of the carbon surface on the borohydrides sorption behaviour, three different carbons were adopted: CA-20, a carbon aerogel obtained by the polymerization of resorcinol and formaldehyde provided by ZAE Bayern, with average pore size of about 20 nm; CMK-3 carbon, that was synthesized according to the procedure described in the previous paragraphs, with average pore diameter of 5 nm; and non-porous graphitic carbon disks (CDs) purchased from n-TEC (Norway). The eutectic mixture was prepared according the method described by Javadian et al.[187], but with a molar ratio of $LiBH_4$ and $NaBH_4$ of 0.71: 0.29 as suggested by the more recent study of Dematteis et al.[176] Carbon and borohydrides were mixed manually with a pestle and mortar, placed in a quartz sample holder and sealed in a stainless steel reactor. The amount of hydrides

used for the infiltration was based on the total pore volume (TPV) of the carbons (i.e. TPV = 1.4 cm^3/g for the CA-20 and 1.2 cm^3/g for the CMK-3) and the density of the hydrides mixture (0.78 g/cm^3) in order to fill the 60% of the carbon pore volume. The mass ratios were 1.57:1 and 1.76:1 respectively for the mixtures with CA-20 and CMK-3 with LiNa. Because of the sensitivity of the hydrides to air, all handling was performed under inert conditions in the glove box. The carbon – LiNa mixtures were heated to 250°C (eutectic melting temperature = 216 °C) under an initial backpressure of 100 bar of hydrogen, in order to allow the melting of the hydrides while avoiding potential decomposition reactions. The melting temperature was reached with a heating ramp of 3 °C/min and held constant for 30 minutes before cooling and consequent solidification within the carbon pores. The same experiment, with the same ratio of carbon – hydrides as in the case of CMK-3, was also performed with graphitic carbon disks (CDs), in order to develop a composite non-porous material for comparison, namely CD-LiNa. In this way it would be possible to highlight and separate any enhancements arising due to nanoconfinement from those originating from catalytic effects due to contact with the carbon surface. Finally, the same experiment was performed with the pure eutectic mixture as a blank.

4.6.2 Carbon - $LiBH_4$ /KBH_4 composite materials

The LiK/Carbon composite was developed using a method similar to the one adopted for the LiNa eutectic mixture and described by Roedern et al.[322] The $LiBH_4$ – KBH_4 eutectic mixture, with a molar ratio of 0.72: 0.28 and a melting temperature of 105°C, was used to synthesize the composite material with both the CA-20 and the CMK-3 mesoporous carbons. Also in this case, a non-porous graphitic carbon borohydrides composite was prepared in order to highlight the effect of nanoconfinement on the sorption behaviour of the infiltrated material over a simple catalytic effect induced by the surface reaction between hydrides and carbon. The processing to prepare the material starts with manual mixing of the carbon scaffold with the eutectic mixture (in the glove box) in order to obtain a homogeneous mixture of powders. The amounts of carbon and hydrides used in the experiments were calculated taking into count both the total pore volume of the carbon (TPV=1.4 and 1.2 cm^3/g respectively for CA-20 and CMK-3) and the density of the mixture to be infiltrated (0,86 g/cm^3) in order to fill 60% of the total pore volume (weight ratios CA-20 – LiK 1.56:1 and CMK-3 – LiK 1.58:1). The product was sealed in a stainless-steel reactor, under a starting backpressure of 100 bar of high

purity hydrogen, heated at a rate of 3 °C/min up to 125°C for 30 minutes in order to allow the molten hydrides to penetrate inside the pores of the carbon. The same procedure was used for the synthesis of the LiK/CD composite material and the blank where the hydrides were melted and recrystallized without carbon.

4.7 N_2 adsorption measurements (77 K)

The typical properties of porous materials, such as pore size distribution, total pore volume (TPV or V_t) and specific surface area (S_{BET}) are deduced by means of N_2 adsorption/desorption experiments at 77 K (Figure 41). The measurements were performed in the N.C.S.R. Demokritos with a Quantachrome Autosorb-1MP. Such measurements are very important in order to determine the successful infiltration of borohydrides into the pores of the carbon scaffolds. In fact, the amount of material nanoconfined is evaluated by comparison of total pore volume and surface area of the carbon scaffolds before and after the hydrides infiltration. The experiments for the determination of the nitrogen adsorption isotherms at 77 K were performed on the carbon scaffolds after outgassing, in order to eliminate any trace of air or moisture trapped into the narrow pores. The outgassing treatment was performed by applying high vacuum at 250 °C for at least 10 hours. The total pore volume was determined by assuming that the pores are totally filled at high relative pressures, while the adsorbed N_2 has the density of the liquid. Particular attention must be paid on the assumption of pore filling which holds only if there is a clear plateau at high relative pressures.

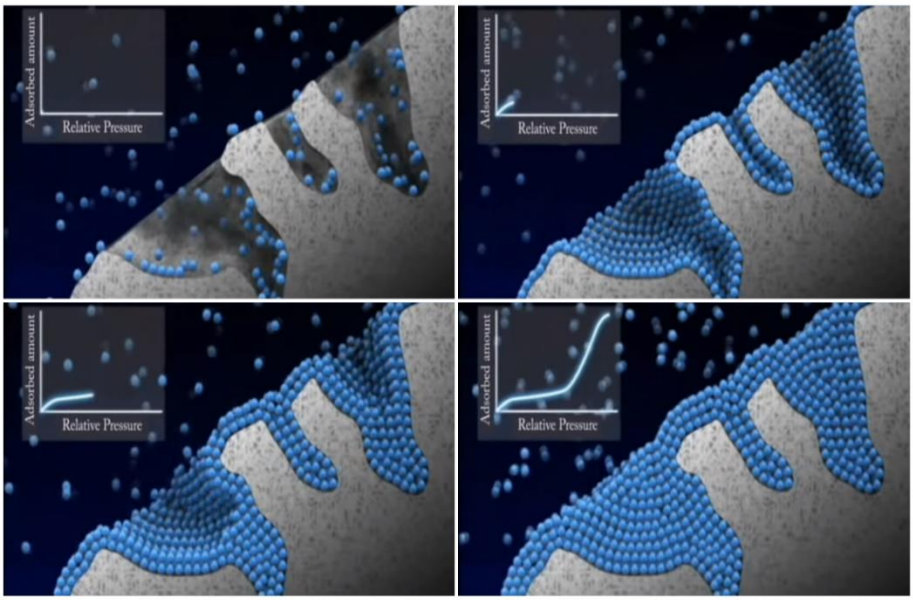

Figure 41: Evolution of the pores filling and the relative isotherm (squares) with the increase of the value of relative pressure p/p_0.[323]

In general adsorption isotherms of subcritical gases can be grouped in five different types (Figure 42):

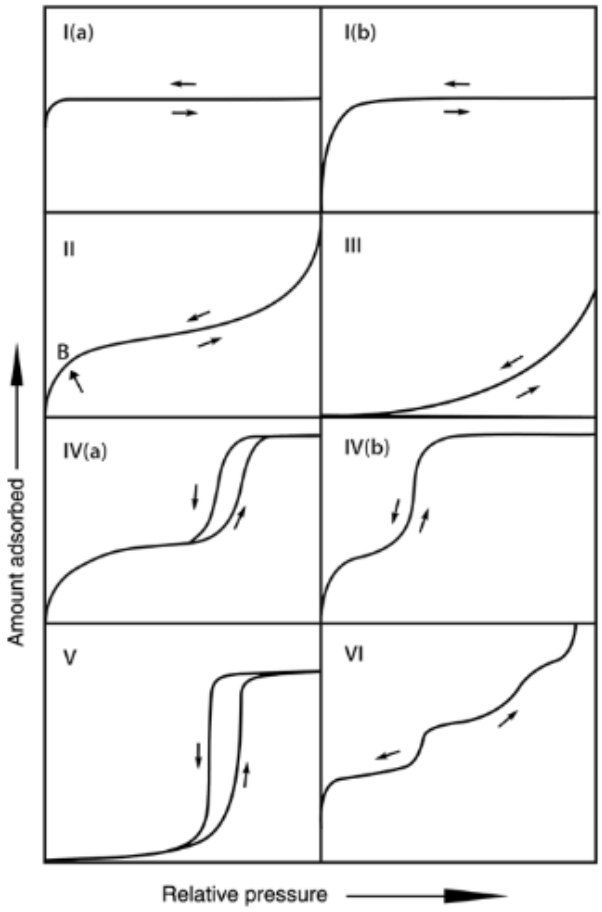

Figure 42: Classification of physisorption isotherms [324]

Type I isotherms are typical for microporous materials. In micropores (< 2nm) the interaction potentials of opposing walls overlap creating thus deep potential wells that lead to enhanced adsorption. For this reason micropores are totally filled at low relative pressures and a clear plateau is observed even at a certain low relative pressure value. Type I(b) isotherms reveal a smoother uptake at low relative pressures and are observed when the pore size distribution includes larger mesopores and extends slightly to the low mesopore range (< 2.5 nm).

Type II isotherms are typical of physisorption on nonporous or macroporous materials. In this case the adsorption is not limited and the B knee indicates monolayer coverage after which additional layers are built (multi-layer adsorption). In Type III isotherms point B is missing and the formation of a monolayer cannot be identified. This happens when the interactions between the fluid-fluid interactions are stronger than the fluid-solid ones and complete wetting of the solid surface is not favoured (e.g. H_2O sorption on a hydrophobic surface). Type IV isotherms are the most interesting for our materials, as they are observed in mesoporous adsorbents. At low p/p_0 values the isotherm has a Type II behaviour, due to monolayer and multilayer adsorption on the mesopore walls. At higher relative pressures capillary condensation occurs in mesopores since due to confinement, the gas can condense at lower pressure p than the saturation pressure of the bulk liquid, p_0. At even higher pressures, mesopores are completely filled and a saturation plateau is observed. The condensation in certain conditions in pores wider than ~4nm is accompanied by hysteresis (Type IV(a)). For pores with smaller size, isotherms of Type IV(b) are obtained. Type V isotherms are typical of micro and mesoporous materials with weak adsorbent-adsorbate interactions. At low relative pressures the isotherm is similar to the Type III isotherms, however at higher relative pressures clustering and pore filling occur. Type VI pertains to extreme situations were the solid surface is extremely uniform and layer by layer adsorption occurs giving rise to separate adsorption steps for each adsorbed layer.[324,325]

The values of surface area are calculated according to the BET multipoint method (Brunauer-Emmett-Teller multipoint) in accordance with the standard specification ISO 9277:2010 (ISO/TC_24/SC_4, 2010) for the correct selection of points in micro and meso-porous materials. The BET equation describes the adsorption isotherm of a free surface and is given by: [324]

$$\frac{\frac{p}{p_0}}{n\left(1-\frac{p}{p_0}\right)} = \frac{1}{n_m C} + \frac{C-1}{n_m C}\left(\frac{p}{p_0}\right)$$

Where n is the amount of moles (normalized e.g. to the weight of the adsorbent) adsorbed at relative pressure p/p_0 and n_m is the specific monolayer capacity (e.g. moles/g adsorbent). The constant C is a parameter which is related to the energy of adsorption and the isotherm shape is reflected on its value: for $C < 2$ we have Type III or V isotherms and BET method is not applicable; for C at least ~80 the B point is well defined; for high C values >150 the isotherms are those typical of materials with high energy adsorption sites. After calculating the C value and the monolayer capacity n_m by the linear relation between $(p/p_0)/[n(1-(p/p_0)]$ and p/p_0 in a range of values (usually between $0.05<p/p_0<0.35$) it is possible to calculate the BET specific area a_s through the equation:

$$a_s = \frac{n_m \cdot N \cdot \sigma_m}{m}$$

Where N is the Avogadro number, σ_m is the molecular cross-sectional area of the adsorbate molecule in the monolayer (typically 0.162 nm^2 for N_2 at 77K) and m is the mass of the adsorbent.

Pore size distribution was calculated through the software AS1Win Quantachrome by applying modelling methods such as NLDFT (Non-Local Density Functional Theory) and QSDFT (Quenched Solid Density Functional Theory). For each material the proper model was selected depending on the material (silica or carbon) and the expected shape of pores (slits for carbon micropores and cylinders for carbon and silica mesopores).

4.8 X-ray powder diffraction

Part of the characterization of the porous materials before and after infiltration was performed via X-ray powder diffraction at both low and wide angles. The instrument used (NCSR Demokritos) was a Rigaku R-AXIS IV Imaging Plate Detector coupled with

a Rigaku RU-H3R Rotating Coper Anode X-Ray Generator (λ = 1.54Å). The instrument operates in Debye-Scherrer geometry (Figure 43).

The samples were typically loaded in Lindemann type glass capillaries (sealed with grease if the material under analysis was sensitive to air), and secured on a rotating stage, after careful alignment with the X-ray beam. In general, 10 minutes exposure time (in transmission mode) was sufficient for a good signal to noise ratio. The 2D detector data (powder diffraction rings) were integrated. The detector distance was fixed during the exposure depending on the range of angles of interest. Small angle x-ray scattering (SAXS) is particularly interesting for mesoporous materials with regular pore patterns and was used to detect the regularity of the pore structure and often to evaluate the integrity of the scaffold after the thermal treatments. Wide angle x-ray scattering (WAXS) on the other hand was used to characterize the borohydrides and moreover check the extend of infiltration, since successful confinement in the pores results in significant broadening or complete disappearance of the Bragg reflections. The same kind of analysis was performed also in the University of Aarhus; in this case the instrument utilized was a Rigaku Smart Lab X-ray diffractometer (Bragg-Brentano geometry), with a Cu Kα source (λ = 1.54 Å).

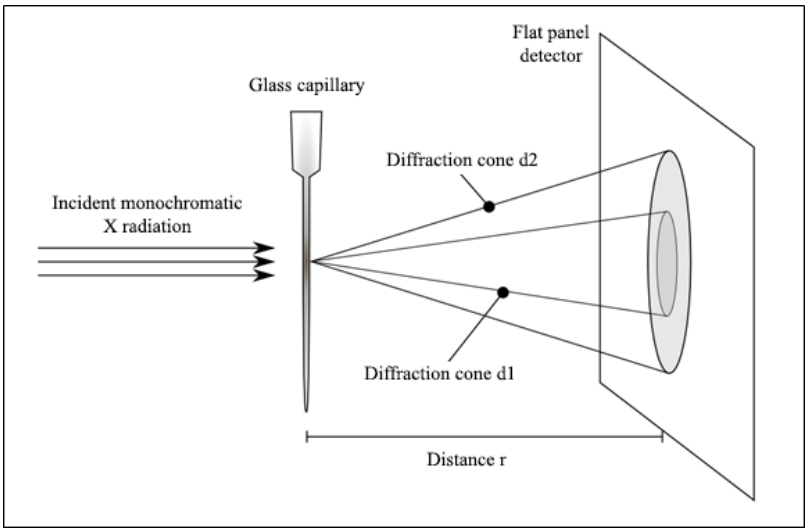

Figure 43: Debye-Scherrer diffractometer geometry. [326]

4.9 Temperature Programmed Desorption – Mass Spectrometry (TPD-MS)

The study of the thermal decomposition paths of the pure borohydrides as well as the composite materials was partially performed through experiments of dehydrogenation

under controlled conditions. The Temperature Programmed Desorption (TPD) experiment allowed the gradual decomposition of the material under analysis, with consequent emission of volatile products. The gaseous species were constantly analysed through a Mass Spectrometer coupled to the TPD set-up. Continuous monitoring of the gas phase products of decomposition upon heating the sample with a certain temperature ramp gave us in real time indications of the possible reactions taking place at different temperatures. The instrument used for the experiment is divided in different parts, as follows:

• Heating unit or furnace: The core of the furnace is an electrical resistance encased in a cylindrical ceramic brick, and directly connected to the heating controller that provides the power. The internal section, where the sample is placed, is a one end open carbon cylindrical tube that provides thermal contact between the resistance and the sample as it is in direct contact with the quartz sample holder. For this reason, all the thermocouples for the temperature control and monitoring are located in direct contact with both the carbon and the sample holder. The working temperatures commonly used were on a range between room temperature and 700 °C. The heating core was insulated externally and a further ceramic wool insulation was applied to cover the sample area.

• Proportional – Integral – Derivative controller (PID controller): the controller is equipped with temperature monitoring and safety systems and allows programming different heating programs.

• The carrier gas line: a special piping construction was constructed in order to allow a continuous flow of inert gas through the sample cell. This stream was connected to the mass spectrometer in order to detect decomposition products. The gas used was high purity argon, the flow of the carrier was regulated by a mass flow controller usually set to 60 ml/min. Through a series of valves the carrier is directed first to the sample cell, and the to an exhaust to atmosphere); however, before the exhaust a small quantity of gas (1-2 ml/min) was sampled and directed to the mass spectrometer. The connection with the MS was made by a heated capillary, serving as an anti-condensation system, while an additional turbo pump system was used for outgassing/cleaning all the gas lines.

• Sample holder: it was constituted by a quartz test tube attached with vacuum compatible resin to a metal connector able to link the sample with the gas line. The sample was packed in a 5 mm diameter quartz cell and covered with quartz wool, in

order to let the gasses pass without elutriating the powders. A series of valves was used to connect the sample with the carrier gas (or isolate) (Figure 44).

• Mass Spectrometer: the instrument utilized was an Omnistar GSD 301 O1 by Pfeiffer. The molecules produced by the decomposition of the sample are directed by the carrier along the gas line and from that to a capillary directly connected to the mass spectrometer. The environment inside at the instrument is kept under high vacuum (i.e. 1E-8 mbar) by a turbopump. The molecules introduced in the instrument are ionized, filtered according to the fragment m/z values (m: mass, z: charge) by means of a quadrupole mass analyser and finally directed to the detector.

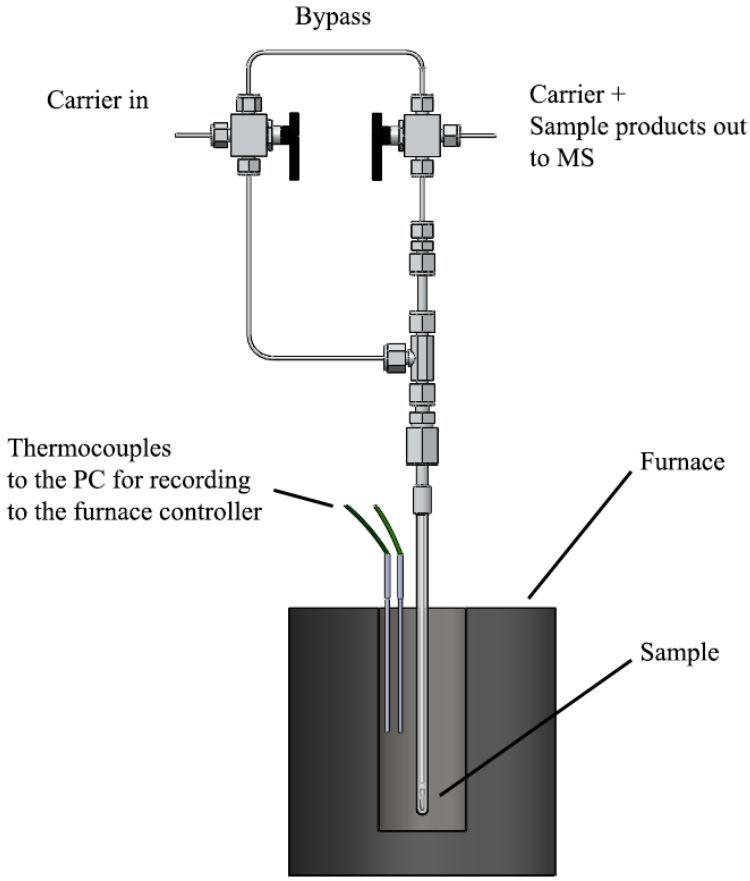

Figure 44: Schematic model of the cell used to keep the sample inside the furnace during the thermal treatment and give it a connection to the mass spectrometer.

4.10 TPD-MS experiments for the LiNa, LiK and relative composite materials

The thermal decomposition of the borohydride composite materials as well as the bulk borohydrides, was performed by heating the sample from room temperature to 700 °C. The sample, located in a quartz cell, described in the previous section, was heated with a rate of 5 °C/min up to 700 °C and then kept to 700 °C for 1 hour before free cooling to room temperature. The experiments were performed under 1.4 bar of pressure, with a constant gas carrier (Ar) flow of 60 ml/min.

The m/z signal monitored was mainly H_2 (m/z=2). A second molecule, often released during the decomposition of borohydrides is diborane, with signals at m/z = 27, 26 and with smaller percentages also 25, 24, 23 (diborane was actually never detected during the decomposition of analysed compounds). Additionally, H_2O, N_2 and O_2 (m/z = 18, 28, 32) were constantly monitored (in order to detect any air contamination in the gas line) along with CO and CO_2 (m/z= 32, 44) as possible products of carbon decomposition/oxidation.

4.11 Sievert apparatus and hydrogenation/dehydrogenation cycles

The sorption properties of the materials as well as the hydrogen capacity were studied through a series of cyclic hydrogenations and dehydrogenations. The instrument used was the same manometric apparatus used to infiltrate the borohydrides in the carbons. Also in this case, pressure and temperature were constantly monitored and recorded on a computer through a LabView program.

During the cycling experiments of LiNa and the composite materials with carbon, the sample was transferred in a quartz tube (9 mm diameter, 50 mm length), closed at one side and covered with quartz wool, in order to avoid the elutriation of the thin powder in the reactor chamber. The quartz sample holder was inserted in a stainless-steel reactor, connected to the Sievert's apparatus. The reactor was sealed with stainless-steel VCR connections, was able to work at high temperatures and pressures reachable through a custom-made furnace. The experiment of dehydrogenation was performed by initially pulling vacuum with a turbopump. Once the reactor chamber was completely evacuated, 1.4 bar of hydrogen (purity 99.9999%) was admitted in the reactor. The sample was heated slowly from room temperature to 450 °C with a heating rate of 2 °C/min and left at that temperature for 10 hours. During this process the temperature of the instrument was kept constant (at 30 ˚C) and the pressure was constantly monitored.

After the 10 hours of isotherm at 450 °C the sample was cooled down in order to evaluate the difference of pressure at room temperature due to the presence of the desorbed hydrogen.

The dehydrogenated sample was then subject to a hydrogenation procedure under high pressure of hydrogen. As for the dehydrogenation experiment, the reactor chamber was evacuated and hydrogen was then admitted in the reactor increasing the pressure up to ~100 bar. The sample was heated up with a ramp of 5 °C/min to 400 °C. The temperature was then kept constant for 10 hours in order to allow the material do sorb hydrogen. Also in this phase of the experiment, after the heat treatment the sample was slowly brought back to room temperature in order to evaluate the variation of pressure and consequently to calculate the amount of sorbed hydrogen. Dehydrogenation-hydrogenation experiments were repeated five times on each sample in the same conditions, in order to evaluate the cycling capacity of the materials, which is fundamental for possible applications.

The same experiment was performed with the same instrument also on the LiK and the LiK/carbon composite materials. Following a procedure similar to the one reported for the LiNa composites, before starting desorption, the reactor chamber was evacuated with a turbopump and refilled with high purity hydrogen (purity 99.9999%), with a pressure of about 1.4 bar. In this case the dehydrogenation was performed by heating the sample with a heating ramp of 3 °C/min from room temperature to 450 °C. The material was kept 4 hours at 450 °C for a full dehydrogenation before cooling to room temperature, where it was possible to evaluate the pressure change and thus the amount of desorbed hydrogen. The rehydrogenation of the sample also in this case was performed by means of a high temperature and high-pressure treatment. The sample, in a reactor loaded with about 100 bar of hydrogen, was heated up with a rate of 5 °C/min to 400 °C and left at that temperature for 12 hours, in order to let the material reach the full hydrogenation level. Dehydrogenation and rehydrogenation were repeated with the same procedure on the same material in order to complete 5 cycles and evaluate the cycling sorption capacity of the samples.

4.12 Fourier-transform infrared spectroscopy (FTIR)

The carbon scaffolds, during the carbonization process at high temperatures lose most of the heteroatoms of the original precursors. These atoms are mostly oxygen and

hydrogen and are removed as low molecular weight volatile molecules, however, traces of these species may remain as functional groups, typically –OH, -O-, -CO and -COOH. The presence of functional groups reduces the chemical inertness of the scaffold as they may react with the confined hydrides. An estimation of the surface functional groups of a carbon is possible through Fourier-transform infrared spectroscopy (FTIR).

The analyses of the carbons were performed by irradiating the solid samples with an IR beam after mixing the carbons manually with pestle and mortar with anhydrous KBr. Due to the high absorbance of the carbons only a little amount (~1 mg or less) of carbon was mixed with around 300 mg of KBr. The KBr/carbon powders were pressed with a hydraulic press initially to 3 ton-force/in^2 for 30 seconds and after to around 10 ton-force/in^2 for 3 minutes. After fixing the pellets in a proper window along the path of the IR beam, it is possible to irradiate the samples and collect the absorbance data.

4.13 Scaffolds characterization results

4.13.1 Characterization of SBA-15

As already mentioned in the previous paragraphs, the preparation of SBA-15 is the first step in order to synthesize the CMK-3 carbon scaffold. The synthesis of SBA-15 was performed several times, giving products with almost identical characteristics, as revealed through a series of analytical methods detailed below, highlighting the good reproducibility of the procedure.

The pore properties of the SBA-15 were evaluated by N_2 adsorption-desorption measurements at 77 K. As shown in Figure 45, the obtained isotherm is of Type IV, typical for such materials. An average BET surface area slightly higher than 600 m^2/g and a total pore volume of about 0.7 cm^3/g (at a P/P_0 of 0.97) were estimated, in accordance with literature values. Pore size distribution was deduced using N_2-silica NLDFT kernel for cylindrical pores, revealing a narrow distribution with an average pore diameter of 7.5 nm (Figure 46).

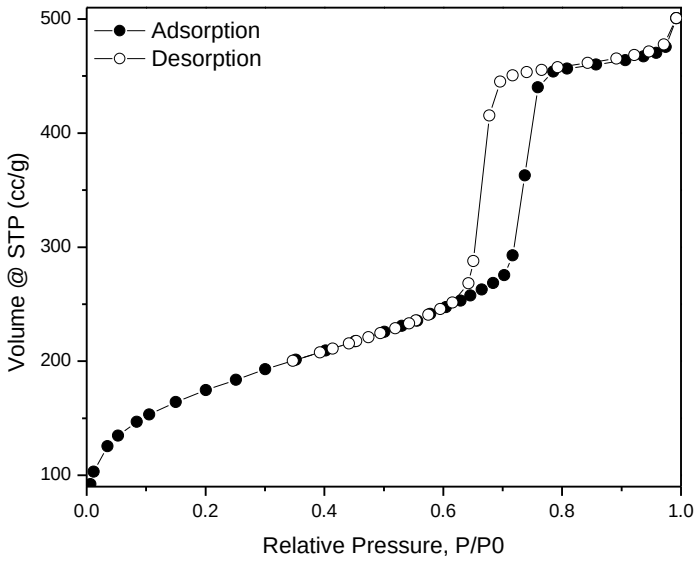

Figure 45: N_2 adsorption (full symbols) - desorption (open symbols) isotherm at 77 K of the SBA-15 porous silica, typical for mesoporous materials (type IV).

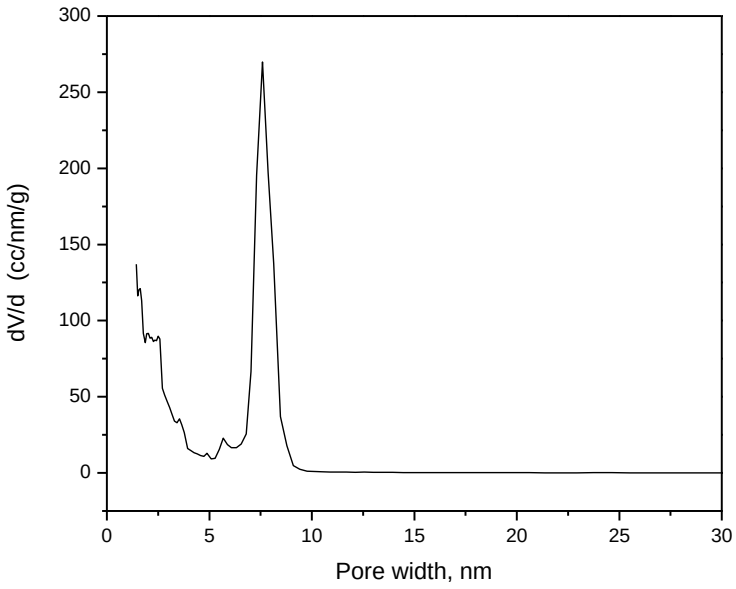

Figure 46: Pore size distribution of the SBA-15 via NLDFT calculations, showing a narrow distribution centred on diameters of 7.5 nm.

The ordered mesoporous structure of the amorphous silica scaffolds was investigated by small angle X-ray scattering (SAXS). The SAXS pattern (Figure 47) revealed three peaks attributed to the (100), (110) and (200) reflections of the typical 2D hexagonal structure of the SBA-15 with a very good long-range ordering of the pores.

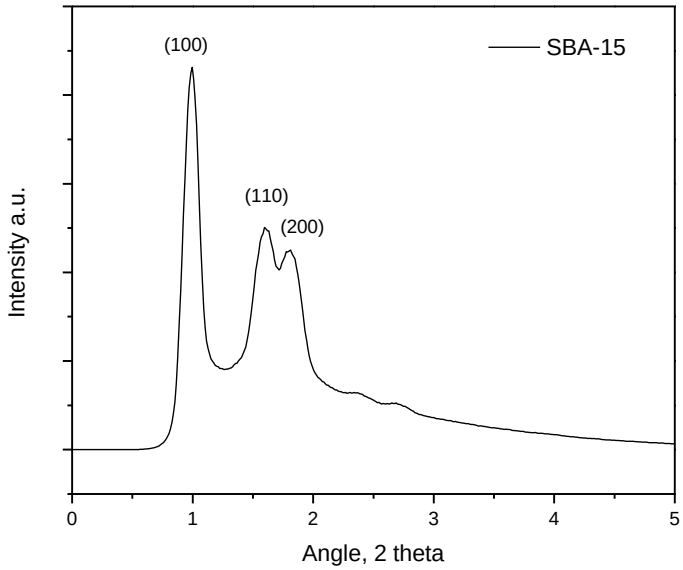

Figure 47: Small-angle X-ray powder diffraction pattern of the SBA-15, showing the typical peaks of the 2D hexagonal structure.

The morphology of the materials was investigated through Scanning Electron Microscopy (SEM) analyses. Figure 48 shows the typical stripe-like macrostructure of the SBA-15, consisting of elongated bean-shaped aggregates in the size of μm, with long mesochannels.

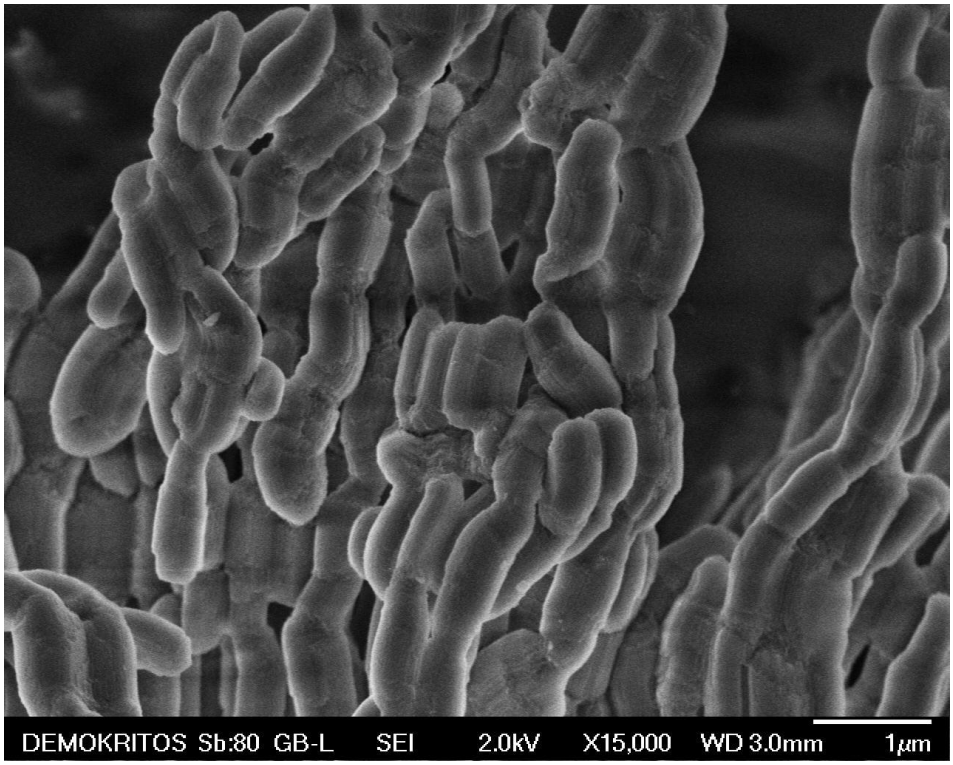

Figure 48: SEM image of mesoporous SBA-15 silica, showing the typical elongated macrostructure.

4.13.2 Characterization of CMK-3

CMK-3 carbon, as obtained from SBA-15 via nanocasting and subsequent heat treatment for removing surface oxygen functionalities, was fully characterized. As revealed, the procedure followed in this work was reproducible and led to carbons with the typical characteristics of the CMK-3 with controlled pore size, in accordance with literature.

As in the case of SBA-15, the N_2 adsorption isotherm at 77 K of CMK-3 carbon was of Type IV, typical for mesoporous materials (Figure 49). The BET area was estimated to be about 1100 m^2/g, and the total pore volume about 1.1 cc/g (at P/P_0 = 0.96), both significantly larger than those of SBA-15. DFT calculations on a carbon model with slit/cylindrical pores revealed a narrow pore size distribution, with the average pore diameter centred at 5 nm (Figure 50).

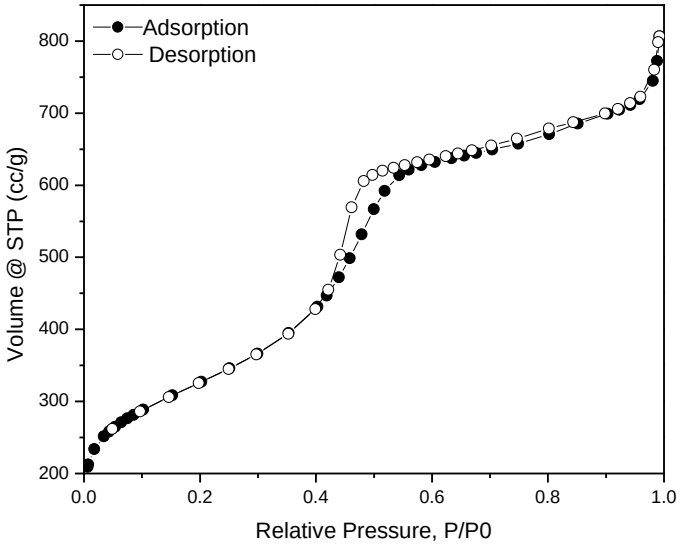

Figure 49: N_2 adsorption (full symbols) - desorption (open symbols) isotherm at 77 K of the CMK-3 carbon, typical for mesoporous materials (type IV).

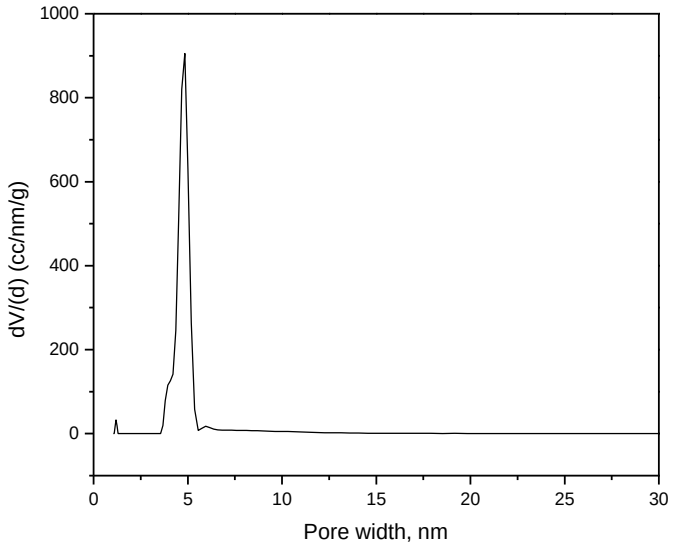

Figure 50: Pore size distribution of CMK-3 carbon obtained through NLDFT calculations, showing a narrow distribution centred on diameters of 5 nm.

CMK-3 carbon is the inverse replica of the SBA-15 silica, both with 2D hexagonal symmetry. The small-angle PXRD pattern (Figure 51) revealed the three typical peaks of CMK-3 ascribed to the (100), (110) and (200) reflections, highlighting the long-range ordering of the carbon nanorods in a hexagonal arrangement.

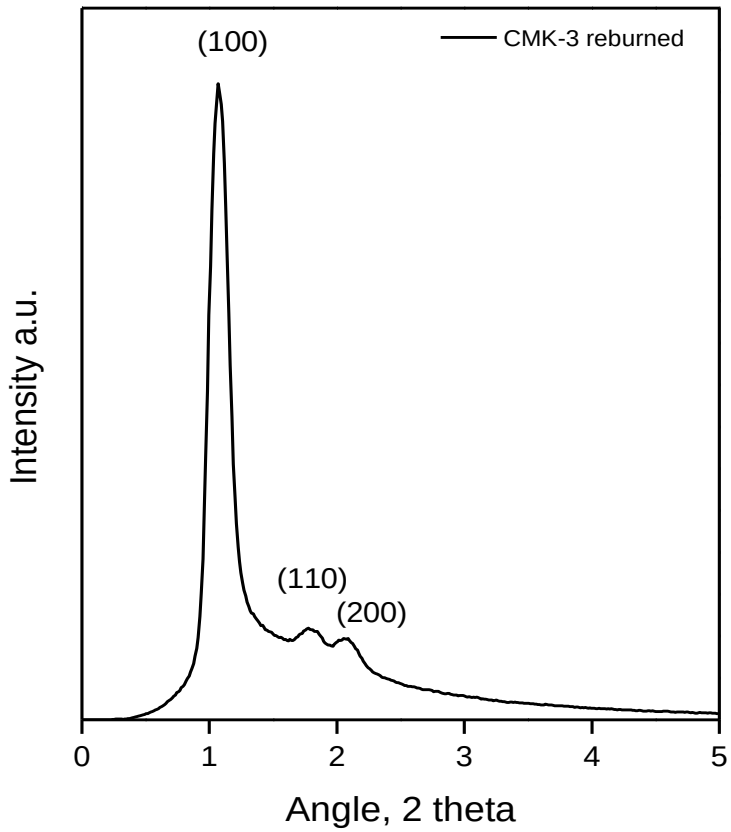

Figure 51: Small-angle PXRD pattern of CMK-3, showing the typical peaks of the 2D hexagonal structure.

SEM images, as shown in Figure 52, revealed the typical morphology of CMK-3 carbon, similar to that already described for SBA-15, consisting of μm-sized agglomerated worm-like particles with long mesochannels.

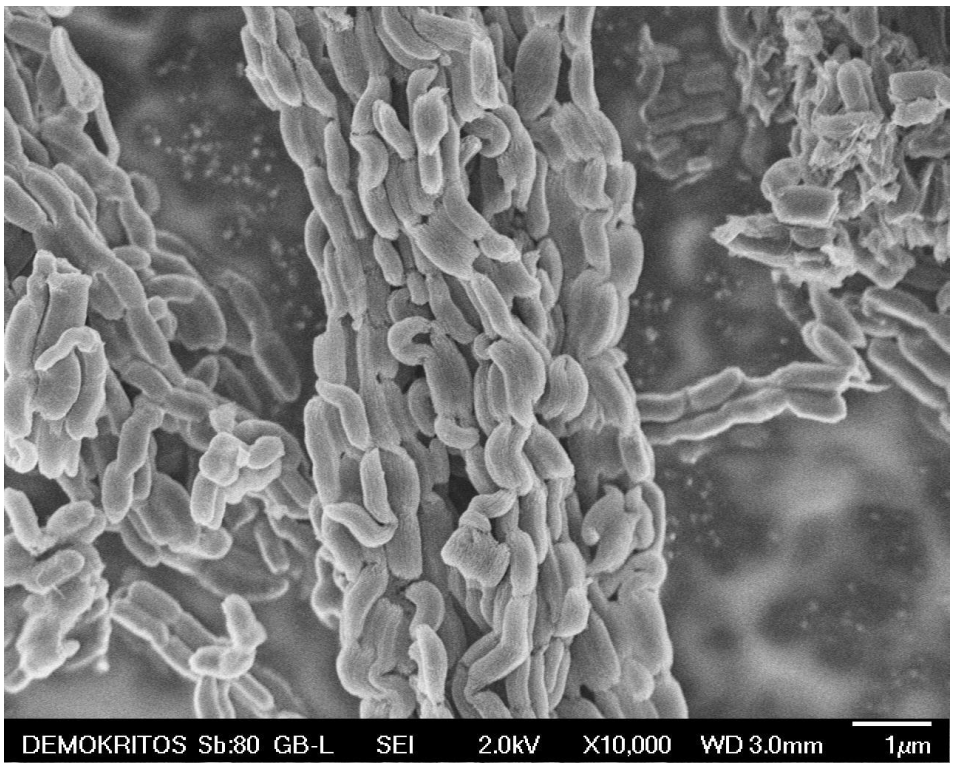

Figure 52 SEM image of mesoporous CMK-3 carbon, showing the typical elongated macrostructure.

CMK-3 after the standard synthesis, that includes treatment with HF acid to remove the silica template, has a considerable number of surface oxygen functional groups. For this reason, as mentioned above, it is necessary to reburn the carbon at 700 °C in order to remove the functional groups that can potentially react with the hydrides. However, despite the drastic reduction of the functional groups after heat treatment, some groups cannot be completely removed, leaving some residues. FTIR analysis is a way to assess these functional groups and investigate whether their presence can affect the capacity of the composite materials. The FTIR spectrum of the thermally treated CMK-3 (Figure 53) revealed a band between 3600 and 3300 cm^{-1} that could be ascribed to O-H stretching vibrations, two small peaks at about 2920 and 2850 cm^{-1} that could be assigned to the stretching vibrations of C-H bonds and a band between 1660 and 1500 cm^{-1} that could be attributed to C=C stretching vibrations.

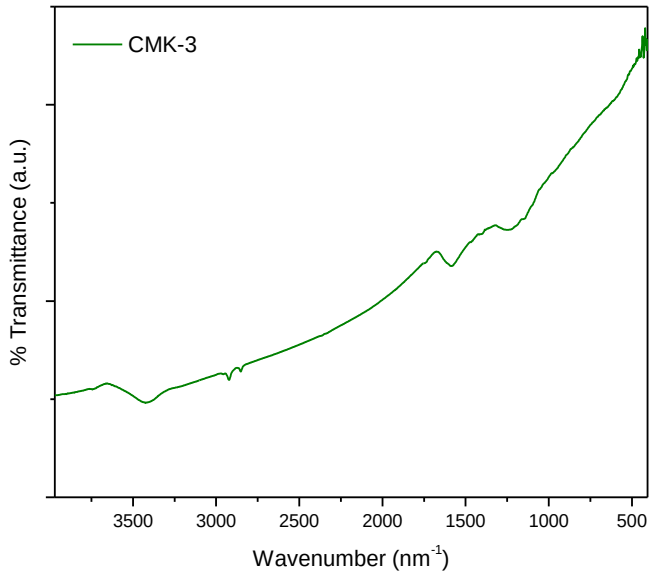

Figure 53: Transmittance FTIR spectrum of reburnt CMK-3 in the range of 4000 - 500 cm^{-1}.

4.13.3 Characterization of Carbon aerogel (CA-20)

The carbon aerogel CA-20 from ZAE Bayern, was used for the infiltration of both the eutectic mixtures of LiNa and LiK borohydrides. CA-20, originally provided as large monoliths with sizes in the order of cm, was manually crushed into powder, both to facilitate analyses and to achieve better infiltrations. From the nitrogen adsorption/desorption isotherm at 77 K of the outgassed sample (10^{-6} bar), it was possible to identify the mesoporous nature of CA-20 by the Type IV shape of the isotherm (Figure 54). By calculating the Brunauer-Emmett-Teller (BET) area in accordance with the BET consistency criteria (ISO 9277:2010), a surface area of about 760 m^2/g was obtained. The pore size distribution was deduced by using the N_2- carbon QSDFT (Quenched Solid Density Functional Theory) kernel for slit/cylinder/sphere pores and revealed an average pore diameter of about 25 nm (Figure 55). The total pore volume (TPV) was determined at $P/P_0 = 0.99$, giving a value of 1.36 cm^3/g.

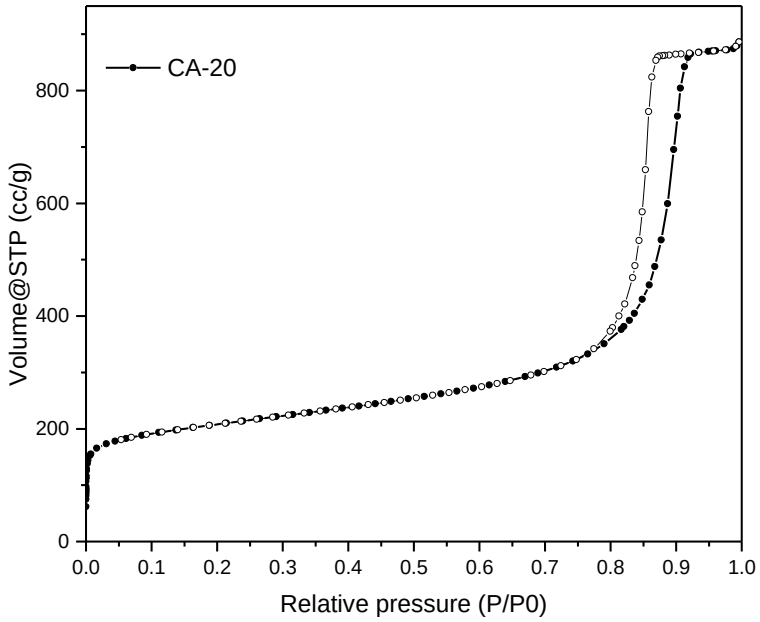

Figure 54: N_2 adsorption-desorption isotherm at 77 K of the CA-20 carbon aerogel.

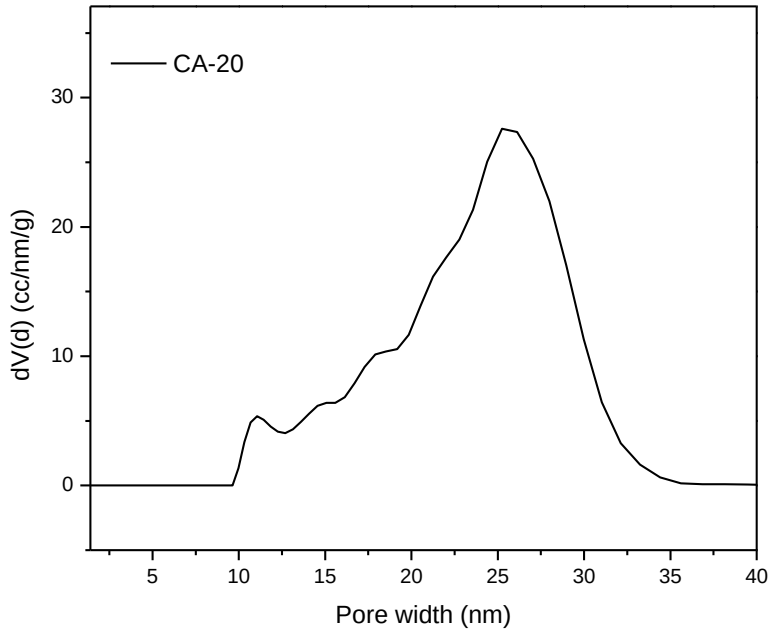

Figure 55: Pore size distribution of CA-20 carbon aerogel obtained through QSDFT calculations, showing a wide distribution centred around 25 nm.

Unlike SBA-15 and CMK-3, the pores of CA-20 are not well-ordered and therefore SAXS cannot provide interesting structural information as in the case of the first two materials.

The CA-20, synthesis process can lead to incomplete elimination of some functional groups that can interact with the infiltrated hydrides and affect the sorption properties of the material. These functional groups, mainly oxygen based, are detectable by FTIR analysis. FTIR spectrum of CA-20 (Figure 56) revealed an intense band between 3650 and 3200 cm^{-1} highlighting the presence of O-H stretching vibrations, two smaller peaks between 2850 and 2930 cm^{-1} that could be assigned to C-H stretching vibrations of alkanes and a series of signals at lower wavenumbers than 1630 cm^{-1} that could be related to C=C stretching vibrations. The signals indicate the presence of several kinds of functional groups on the carbon surface and the intensity indicates a number of groups that may give a non-negligible contribution to the overall behaviour of the material.

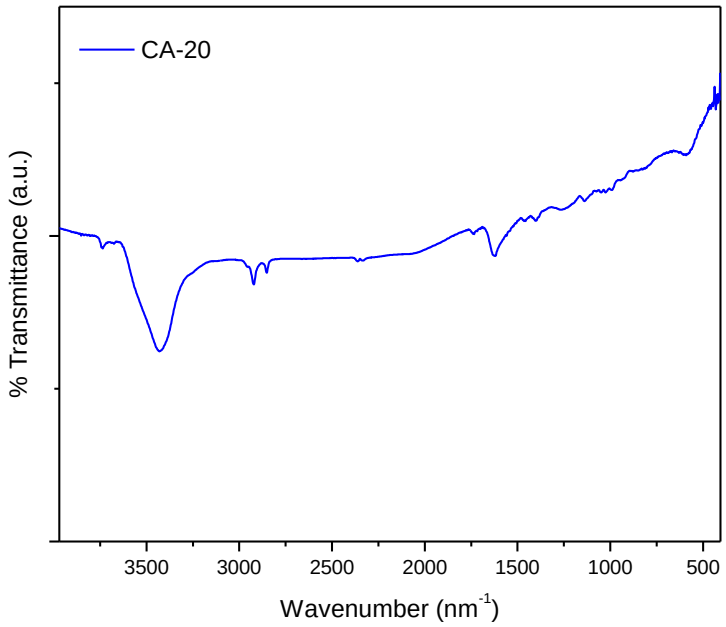

Figure 56: Transmittance FTIR spectrum of CA-20 carbon aerogel in the range of 4000 - 500 cm^{-1}.

4.13.4 Characterization of Carbon discs (CD)

The carbon discs, obtained from n-TEC (Norway), are non-porous graphitic carbons. This material was produced via a plasma torch process and used in this work in order to compare the sorption capacity of the hydrides that have been infiltrated and nanoconfined into porous materials with those simply in contact with this non-porous carbon. The analysis of N_2 (77K) adsorption-desorption isotherm in this case resulted in negligible values of pore volume and surface area, with the latter smaller than about 50

m^2/g. On the other hand, the study of the surface chemistry could lead to useful information about the quality of the material and the possible interactions with the hydrides.

FTIR analysis (Figure 57) revealed only signals with very low intensity, indicating a carbon surface poor in functional groups. The detected signals were similar to those of the other carbon materials (Figure 58). More specifically, the FTIR spectrum of CD revealed a broad band between 3640 and 3320 cm^{-1} related to the common stretching vibrations of the O-H bond, two small peaks at 2920 and 2850 cm^{-1} due to C-H stretching vibrations and a series of signals at wavenumbers smaller than 1680 cm^{-1} due to the presence of C=C bonds.

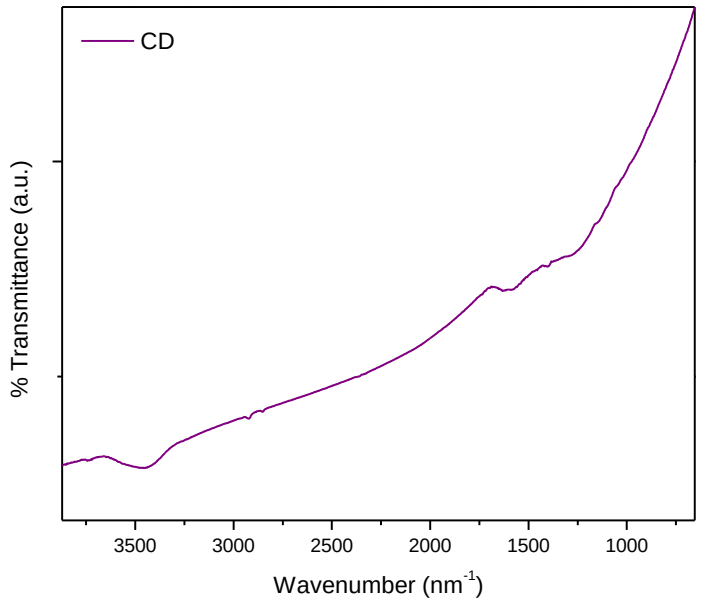

Figure 57: Transmittance FTIR spectrum of carbon discs (CD) in the range of 4000 - 500 cm^{-1}.

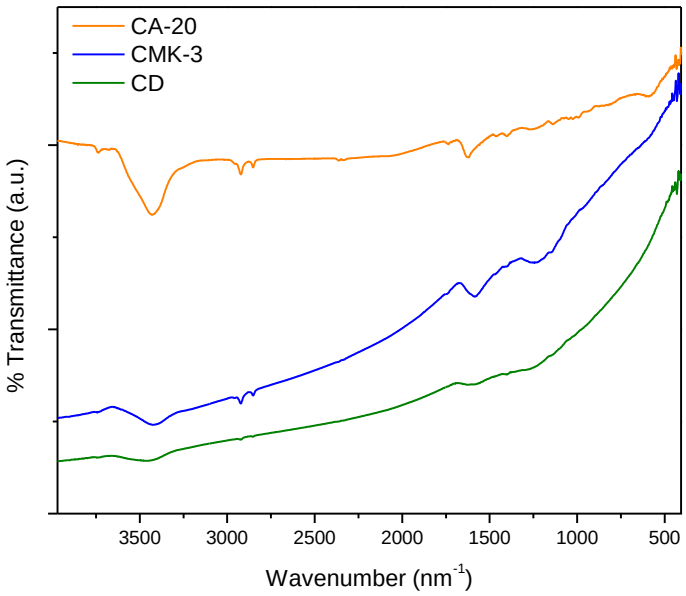

Figure 58: Comparison of the FTIR spectra of CA-20 (orange), CMK-3 (blue) and CD (green).

4.14 Infiltrated eutectic mixtures of borohydrides into carbons

As explained in the previous chapters, nanoconfinement can change the inherent behaviour of the materials in several ways. The most significant are destabilization due to particle size reduction and the ability to prevent reaggregation, thereby preserving the destabilized state. To achieve nanoconfinement, the use of substances that can melt to reach a liquid form without the use of solvents is preferable to a system where wet chemistry is necessary. In this way, post-infiltration processes to eliminate the solvent and possible by-products such as stable complexes can be avoided. Moreover, performing a melt infiltration usually requires easier procedures and more user-friendly equipment than common wet infiltrations. However, when in contact with the carbon surface, some hydrides may be further destabilised due to catalytic effects before the completion of the infiltration, and thus treatments under high hydrogen pressure may be necessary to avoid decomposition phenomena during the infiltration process.

Eutectic systems, such as those studied in this work, can melt entirely at a certain temperature, allowing full infiltration into the materials without leaving any portion of solid outside the scaffold.

Two different eutectic mixtures of borohydrides were used, both with $LiBH_4$ as the major and most active component. The first was a mixture of $LiBH_4$ and $NaBH_4$, with a molar ratio of 0.71: 0.29 ($LiBH_4$ - $NaBH_4$) and a hydrogen content of 15.25 wt%. The second

was a mixture of $LiBH_4$ and KBH_4, with a molar ratio of 0.73: 0.27 ($LiBH_4$ - KBH_4) and a hydrogen content of 13.2 wt%.

As already mentioned, both mixtures studied in this work and the individual hydrides of which they are composed are not able to reversibly exchange hydrogen. Destabilization due to nanoconfinement could play a fundamental role in changing this aspect, which is crucial for hydrogen storage materials.

In order to investigate how the nanoconfinement affects the behaviour of the materials, the hydrides were melt infiltrated into CMK-3 and CA-20 type porous carbons, to obtain carbon-hydride composite materials and were further compared to both a non-porous carbon borohydride composite and the pure bulk hydrides.

The materials were characterized by several analysis techniques.

The phase composition of the eutectic mixtures of the borohydrides as well as the presence of any possible crystalline phase of the hydrides located outside of the pores of the scaffold were investigated by X-ray diffraction. The instrument used was a Rigaku Rotating Anode/R-AXIS IV Imaging Plate Detector (Cu Kα radiation, λ = 1.540593 Å, transmission geometry). Due to the air-sensitivity of the borohydrides, the samples were placed into borosilicate glass capillaries and sealed with vacuum grease. The preparation of the samples was performed in a glovebox, under an argon atmosphere with O_2 and H_2O concentrations below 0.05ppm.

A complementary method to evaluate the efficiency of the infiltration process is the analysis of N_2 adsorption/desorption at 77 K, which was performed with the aid of a volumetric gas sorption analyser (Autosorb-1-MP, Quantachrome). Surface area, total pore volume and pore size distribution of the carbon material before and the composite material after the infiltration can reveal whether the hydrides effectively filled the scaffold pores.

Differences in the decomposition of borohydrides upon heating, were detected through Thermal Programmed Desorption Mass Spectrometry (TPD-MS) measurements. The measurements were performed using a special temperature-controlled heating device connected to a turbo pump and a quadrupole mass spectrometer (OmniStar GSD 301 O1 Pfeiffer). The samples were heated from room temperature to 700 °C at a heating rate of 5 °C/min under a constant argon flow of 60 ml/min and a pressure of 1.4 bar. The air-sensitive samples, which were handled in a glovebox under an Ar atmosphere, were placed in a quartz sample-holder (5 mm diameter). The sample-holder was then

inserted into a quartz cell (9 mm diameter) with an internal gas flow, located in a furnace and connected directly via the gas line to the mass spectrometer. The gasses released from the decomposing samples were identified by matching the molecular masses to the corresponding m/z values detected as described before.

The sorption capacity of the materials, the carbon-hydrides composites as well as the bulk mixtures, were analysed with a custom volumetric device, through hydrogen release-uptake cycles. During cycling, the samples, were transferred in a stainless-steel reactor and were loaded with hydrogen with a purity grade of 99.9999%. The cycling experiments were performed by heating the samples to activate the sorption reactions, under ~1.5 bar during desorption and ~80-100 bar for rehydrogenation of the materials.

4.14.1 $LiBH_4$ – $NaBH_4$ (LiNa) eutectic mixture

The bulk eutectic mixture was prepared according to the procedure descripted in paragraph 4.6 in the inano laboratories at Aarhus University under the supervision of Prof Torben R. Jensen. starting from pure $LiBH_4$ and $NaBH_4$.$LiBH_4$ - $NaBH_4$ eutectic mixture with a molar ratio 0.71: 0.29 (melting temperature 216 °C), was then subjected to the same treatments as the carbon composites.

To determine the phase composition of the material obtained, X-ray powder diffraction was performed, collecting data from 10 to 70° 2Theta. In Figure 59 the pattern obtained by PXRD is reported. The preparation of the eutectic mixture involves only a physical treatment where no chemical reactions take place. The only two phases found were the expected ones: o-$LiBH_4$ and α-$NaBH_4$, as also reported by Javadian et al., while no impurities, oxides or reaction by-products were detected.

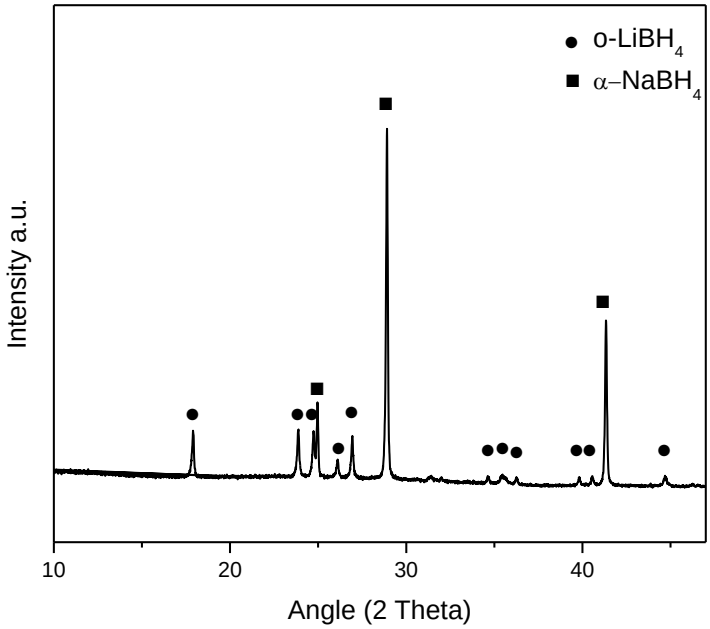

Figure 59: PXRD pattern of $LiBH_4$ and $NaBH_4$ (LiNa) after ball milling.

The TPD-MS measurement of bulk LiNa, by heating the sample up to 700 °C, shows that only H_2 is released during the experiment, with no detectable traces of diboranes. The dehydrogenation of the mixture occurs at temperatures intermediate between those of the pure $LiBH_4$ and $NaBH_4$, in accordance with the observations reported in the literature.[327] LiNa, after being pre-melted under H_2 backpressure, decomposes in four main stages, the first three at 290, 390 and 450 °C can be attributed to the decomposition of $LiBH_4$, while the last one occurring at 490 °C can be ascribed to the $NaBH_4$ decomposition. The thermal decomposition of a mixture of $LiBH_4$ and $NaBH_4$ with a slightly different composition was studied by Liu et al.[327] and two main decomposition pathways were identified: one up to about 520 °C involves the release of H_2 and the precipitation of LiH, $Li_2B_{12}H_{12}$ and B; the second, that occurs at higher temperatures, involves the release of H_2 as well as the precipitation of Na and B.

In Figure 60 the main dehydrogenation events, through the deconvolution of the MS signals, are highlighted. The curves related to the decomposition phases of $LiBH_4$ are shown in green with a profile identical to that presented in the literature for this hydride[91]; at higher temperature, the high intensity signal (orange) is related to $NaBH_4$ decomposition. The last reaction ($NaBH_4 \rightarrow Na + B + 2H_2$)[327,328] without the aid of catalysts/additives [329–331] is highly irreversible and for this reason it was decided to limit

the cycling experiments to 450 °C and actually study only the decomposition of $LiBH_4$ (in the presence of $NaBH_4$). The decomposition of $LiBH_4$ is governed by a complex mechanism that can be represented by two main reactions [327,332,333]

$$LiBH_{4(s)} \rightarrow LiH_{(S)} + B_{(s)} + 3/2H_{2(g)}$$

$$LiBH_{4(s)} \rightarrow 5/6\ LiH_{(s)} + 1/12Li_2B_{12}H_{12(s)} + 13/12H_{2(g)}$$

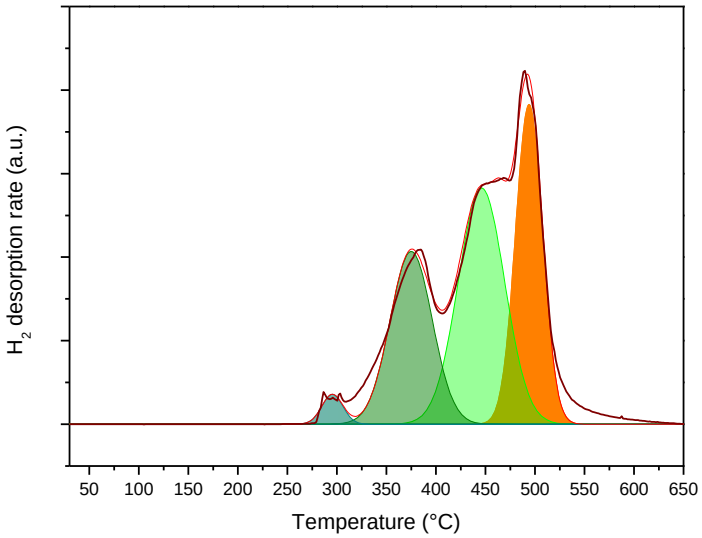

Figure 60: Signals related to the hydrogen desorption during a TPD-MS experiment.

From the deconvoluted curves we can identify $LiBH_4$ decomposition (green) and the $NaBH_4$ decomposition (orange).

This explains the behavior observed during the dehydrogenation/hydrogenation cycles. The cycling sorption capacities of the materials were investigated by experiments performed through a manometric apparatus. The hydrogen release was triggered by heating the sample under ~1.5 bar of hydrogen, from room temperature to 450 °C with a heating rate of 2 °C/min and holding the material under isothermal conditions for 10 hours. The rehydrogenation was performed by heating the sample under ~100 bar of hydrogen as the initial pressure. During the experiment the temperature was increased from room temperature to 400 °C with a heating rate of 5 °C/min and then kept at isothermal conditions for 10 hours. This dehydrogenation and rehydrogenation process was repeated 5 times.

The pure LiNa shows a drastic reduction of the hydrogen released between the first and second dehydrogenation cycle due to the formation of the stable $Li_2B_{12}H_{12}$ closoborane.

From the experimental data we can assume that only the first reaction ($LiBH_4 \rightarrow LiH + B + 3/2H_2$) is reversible and, based on the amount of hydrogen released during the manometric experiments, we may conclude that it occurs in a percentage of 60-70 % of the $LiBH_4$ decomposition. The bulk LiNa releases about 6.2 wt% of H_2, an amount that drops to 3.6 wt% already at the second dehydrogenation step and continues to decrease at each cycle until it reaches about 0.8 wt% of H_2 at the fifth hydrogenation/dehydrogenation cycle suggesting strong deactivation of the system (Figure 61).

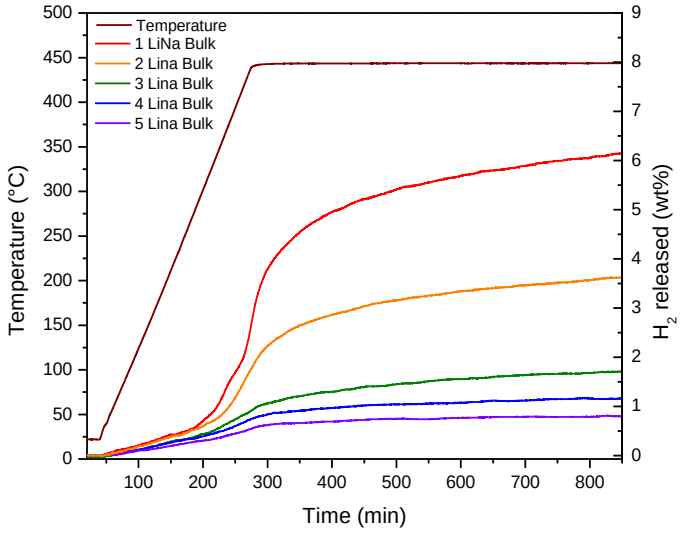

Figure 61: Hydrogen desorption cycles performed on the bulk LiNa from room temperature to 450°C.

4.14.2 LiNa in mesoporous CMK-3

The composite LiNa/CMK-3 was obtained by the nanoconfinement of the eutectic mixture of borohydrides trough a melt infiltration process, described in paragraph 4.6. The pore characteristics of the plain carbon scaffold were determined by N_2 adsorption/desorption isotherms at 77K. As mentioned before, the BET surface area of the pure carbon was 1250 m^2 and the total pore volume was 1.2 cm^3/g. Moreover, the pore size distribution, was narrow and centred at 4.6 nm. Melt infiltration in the carbon was performed by using a quantity of LiNa calculated to fill 60 % of the total pore volume. The obtained sample was analysed to determine the effectiveness of the infiltration.

At first, X-ray powder diffraction was applied (Figure 62), with the same instrument and procedure already explained in the paragraph 4.8.

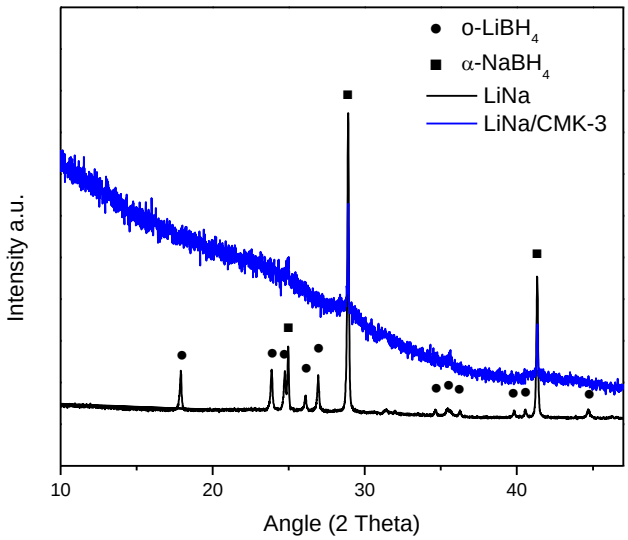

Figure 62: PXRD pattern of bulk LiNa eutectic mixture (black) and LiNa/CMK-3 composite material (blue). The peak symbols indicate the following phases: o-$LiBH_4$ (•), α-$NaBH_4$ (▪). Pattern of the LiNa/CMK-3 composite, where only the most intense $NaBH_4$ peaks are visible.

The analysis shows how after infiltration the strong $NaBH_4$ peaks are still visible, implying that infiltration was incomplete, however it should be noted that even a very small quantity of external crystal may give rise to the XRD pattern observed.

To further investigate whether the borohydrides have been infiltrated inside the pores, a porosimetric analysis was performed (Figure 63). The instrument and methods adopted for the determination of surface area, total pore volume and pore size distribution were the same as those used for the plain carbon. The results were normalized with respect to the pure carbon weight in order to avoid the “artificial” reduction of surface area and pore volume caused by the extra dead weight of the hydride phase.

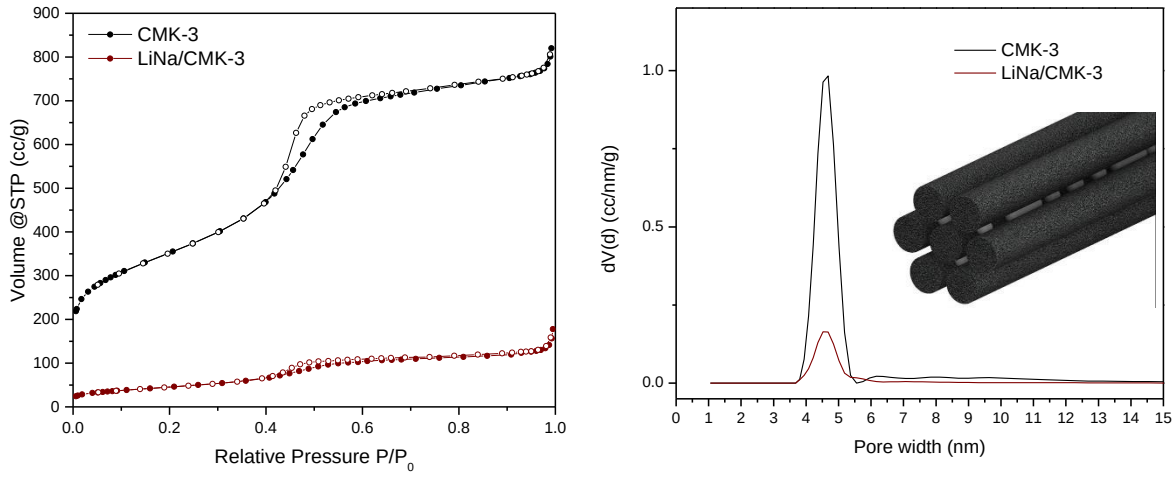

Figure 63: Left: N_2 Adsorption/desorption isotherms at 77 K on CMK-3 carbon (black line) and on the composite material LiNa/CMK-3 (red line). Right: pore size distribution of CMK-3 carbon (black) and of LiNa/CMK-3 (red) obtained through NLDFT calculations, showing a narrow distribution centred on diameters of about 4.5 nm. Inset: 3D model of infiltrated CMK-3.

From the comparison of the isotherms obtained by N_2 adsorption/desorption measurements we can observe a drastic reduction of the surface area for the LiNa/CMK-3 composite. In fact, the surface area decreased from 1250 m^2/g for the pure CMK-3 to 170 m^2/g for the composite. The total pore volume dropped from 1.2 cm^3/g to 0.21 cm^3/g, suggesting successful penetration of the material into the pores, and efficient filling the empty space. No changes in the pore size distribution were observed. This is explained by considering that the LiNa phase is non-wetting and therefore, after melt infiltration and solidification discrete LiNa particles are formed (see inset of Figure 63, right). Such particles reduce the accessible pore volume, but do not alter the size of the open pores.

Using the same apparatus and procedure as for the bulk material, thermal programmed desorption gas spectrometry (TPD-MS) experiments have also been performed on Lina/CMK-3 systems (Figure 64). The decomposition products were analysed in the temperature range between room temperature and 700 °C, with a constant Ar flow. Also in this experiment the instrument was programmed to detect m/z values corresponding to H_2, B_2H_6, Ar, N_2, O_2, H_2O, and CO_2 but, only hydrogen was detected during the whole experiment. The LiNa/CMK-3 composite releases hydrogen in a similar manner to the bulk LiNa and with a similar ratio between the signal intensities. However, the different reaction steps have been somehow merged as decomposition occurs at much lower

temperatures than the bulk material, with the main peaks located at 325 and 360 °C, highlighting the contribution from the carbon surface.

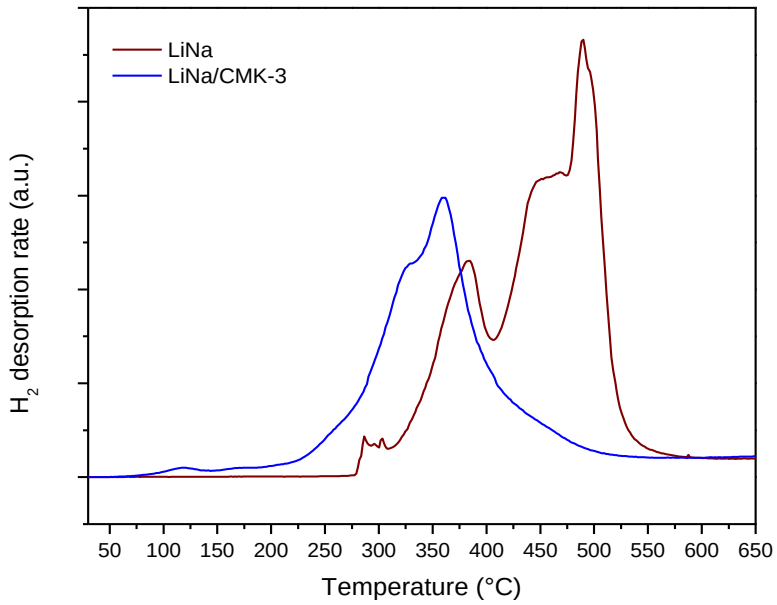

Figure 64: Temperature Programmed Desorption coupled with mass spectrometry (TPD/MS) results for LiNa (dark red) and LiNa/CMK-3 (blue).

Additionally, the sorption capacity and cyclability of the obtained materials were tested. As in the case of LiNa, the hydrogen release and uptake were evaluated with a custom manometric device. The experiment included a desorption phase, under an initial pressure of ~1.5 bar, where the sample was heated with a ramp of 2 °C/min from room temperature to 450 °C, maintained at the same temperature for 10 hours and then freely cooled to room temperature. This was followed by a rehydrogenation phase, under an initial pressure of ~100 bar of hydrogen. The sample was heated at a rate of 5 °C/min, from room temperature to 400 °C, and the temperature was held constant for 12 hours, before the sample was cooled back to room temperature. The dehydrogenation and hydrogenation procedures were repeated on the same sample 5 times.

Also in this case, we can assume that the pressure increase, associated with the gas desorption, is only due to the release of hydrogen, as shown by the TPD-MS experiment. In Figure 65 we see that from the first desorption about 7.3 wt% of H_2 was released in the first cycle, which drops to 4.2 wt% in the second dehydrogenation step but stabilizes around 3.5 wt% for cycles 3-5, revealing that at least a part of the infiltrated material retains its reversibility. The increased release during the first cycle can be attributed to partial decomposition of $NaBH_4$ below 450 °C. This kinetic

enhancement is probably due to nano-confinement and has also been detected in our TPD measurements.[334] However, the decomposed $NaBH_4$, could not be re-hydrogenated and the second cycle finally showed a similar release to the bulk and LiNa/CD samples (as shown below). In contrast to the case of CDs, the nanoconfinement in CMK-3 provides more protection and therefore a higher degree of reversibility, probably by minimizing the formation of closo-boranes.

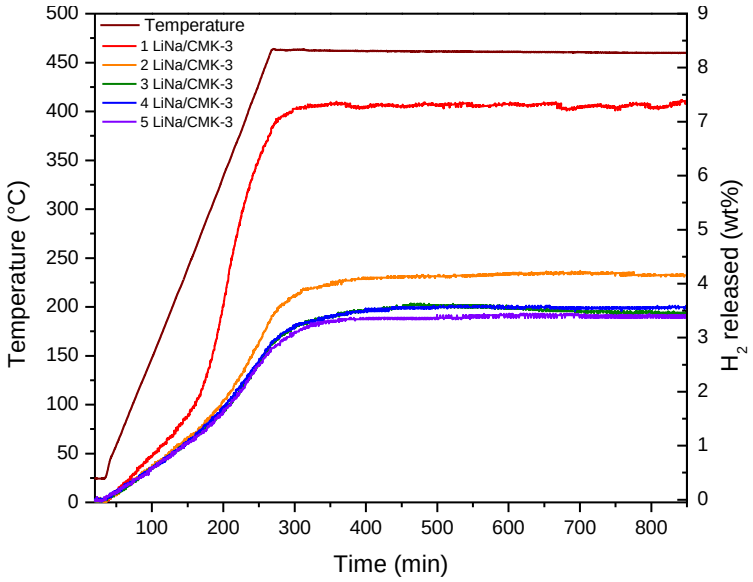

Figure 65: Hydrogen desorption cycles performed on the LiNa/CMK-3 composite from room temperature to 450°C.

After the cycling experiment, a TPD-MS analysis was performed on the same sample, which confirmed that only hydrogen is released from the decomposition, even after 5 dehydrogenations/ hydrogenation cycles.

4.14.3 LiNa on carbon aerogel

The second composite obtained through melt infiltration on a porous material was LiNa/CA-20. The carbon characteristics were determined via porosimetry, from N_2 adsorption/desorption isotherms at 77K. Knowing the total pore volume of CA-20 (TPV = 1.37 cm^3/g) the melt infiltration was performed with carbon and borohydrides calculated to fill 60 % of the total pore volume of the plain carbon according to the procedure described in paragraph 4.6.

To investigate the effectiveness of the infiltration, porosimetric analyses were performed. The instrument and methods adopted for the determination of surface area, total pore volume and pore size distribution were the same adopted for the carbon in pristine conditions but considering only the carbon mass as sample mass.

However, after 30 minutes of melt infiltration it seems that LiNa was not able to fill the carbon pores. For this reason, more infiltration attempts were performed. In the plot below (Figure 66) the isotherms at 77 K of pure CA-20 as well as CA-20 after 30 minutes (overlapping) and 3 hours infiltration.

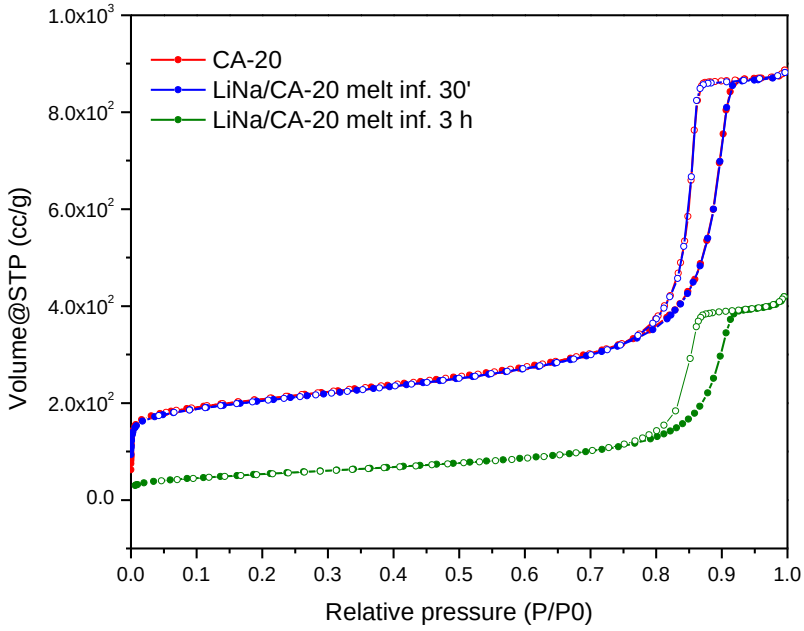

Figure 66: N_2 adsorption/desorption isotherms performed at 77 K on pure CA-20 (red), LiNa/CA-20 after a 30 minutes long melt infiltration (blue) and LiNa/CA-20 after a 3 hours long melt infiltration (green).

Using the same instrument and procedure adopted for the bulk material, thermal programmed desorption gas spectrometry (TPD-MS) experiments were performed on LiNa/CA-20 systems (Figure 67). The products of decomposition were analysed in a range of temperatures between 25 and 700 °C, with constant Ar flow under 1.4 bar, The m/z values corresponding to H_2, B_2H_6, Ar, N_2, O_2, H_2O, and CO_2 were scanned, with only H_2 detected during the entire experiment. LiNa/CA-20 releases hydrogen in three reaction steps, with a profile that shares some similarities with the bulk. The main peak

located at 350 °C, highlighting the carbon contribution in lowering the dehydrogenation temperatures.

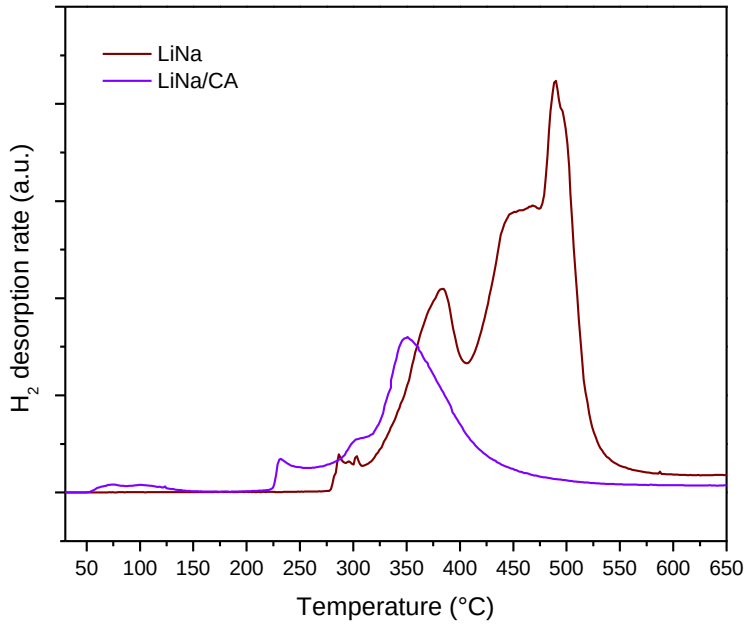

Figure 67: Temperature Programmed Desorption coupled with mass spectrometry (TPD/MS) results for LiNa (dark red) and LiNa/CA-20 (purple).

The sorption capacity and cyclability of the materials were also tested (Figure 68). As for the bulk LiNa, the experiments were performed with a custom manometric device. Desorption was monitored by keeping initially the sample at room temperature under a pressure of hydrogen around 1.5 bar. The sample was then heated with a ramp of 2 °C/ min from room temperature to 450 °C, and this temperature was maintained for 10 hours. The sample was then cooled freely to room temperature. The following rehydrogenation was performed under initial pressure of ~100 bar of hydrogen with the sample heated from room temperature to 400 °C with a heating rate of 5 °C/min. The temperature was kept constant for 12 hours before the sample was cooled back to room temperature. The dehydrogenation/rehydrogenation procedure was repeated 5 times. In the plot below we see that about 8.4 wt% of hydrogen is released during the first cycle, which drops to values between 3 and 4 wt% for the following four cycles, revealing an appreciable degree of reversibility. The important drop of hydrogenation capacity after the first cycle can be ascribed at the formation of stable closoboranes.

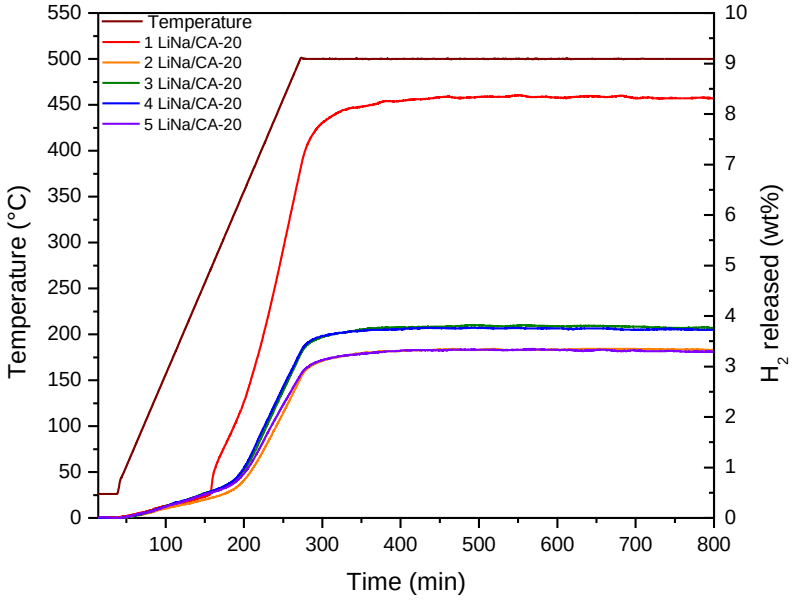

Figure 68: Hydrogen desorption cycles performed on the LiNa/CA-20 composite from room temperature to 450°C.

4.14.4 LiNa on non-porous graphitic carbon

In order to understand whether nanoconfinement plays a greater role in improving the sorption properties of the materials, rather than the interaction of the hydrides with the carbon surface of the scaffold, a non-porous carbon composite was synthesized.

The carbon used for our purposes were graphitic carbon disks. The composite material was synthesized and tested following the same procedure used for the infiltration of the borohydrides into the porous carbons (paragraph 4.6).

The surface area of the pure carbon disks and the corresponding composite with hydrides were evaluated by N_2 sorption isotherms at 77 K and calculated using the BET method. For both materials the surface area was found to be less than about 50 m^2/g, with the composite having a slightly lower surface area (Figure 69).

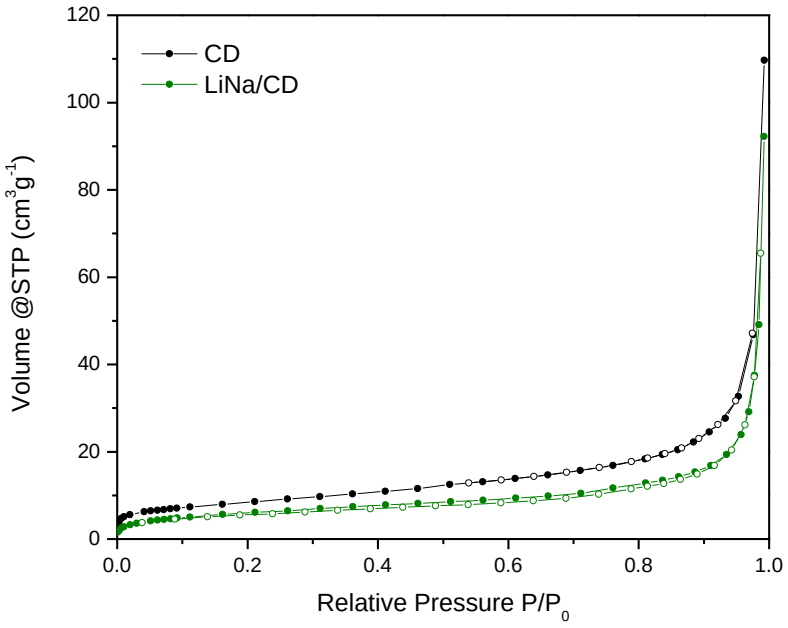

Figure 69: N_2 adsorption/desorption isotherms at 77 K of the pure CDs (black) and the LiNa/CD sample (green).

As in the case of the other materials, TPD-MS experiments were performed in order to investigate the effect of the carbon on the behaviour of the hydrides. Also in this case only hydrogen desorption was detected. The experimental results (Figure 70) show an active role of the CD in lowering the dehydrogenation temperatures of LiNa, which is also evident in the behavior of LiNa/CD that mainly decomposes at 340 and 440 °C. In the latter case we observed that despite the absence of nanoconfinement, the carbon matrix still plays a role in the destabilization of the material, however with a minor intensity than the CMK-3, probably due to the lower surface area of the carbon discs.

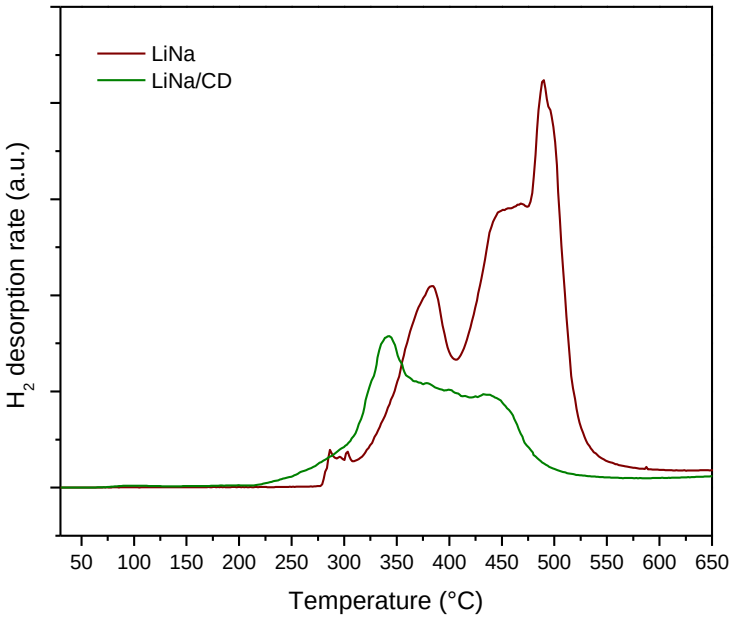

Figure 70: Temperature Programmed Desorption coupled with mass spectrometry (TPD/MS) results for LiNa (dark red) and LiNa/CD (green).

Taking into account only the mass of the active materials in the hydrogen sorption reaction, i.e. that of $LiBH_4$ and $NaBH_4$ and excluding the carbon, the LiNa/CD composite has a similar behaviour to the bulk during the first three cycles, releasing about 6 wt% of H_2 in the first, 4.2 wt% of H_2 in the second and 1.7 wt% during the third cycle. Nevertheless, the sample reaches a constant value of around 1.7 wt% of H_2 in the last three cycles (Figure 71).

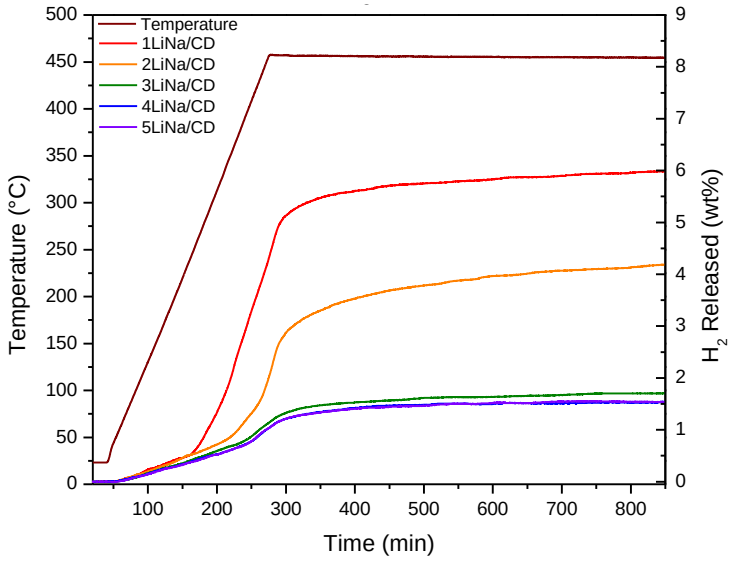

Figure 71: Hydrogen desorption cycles performed on the LiNa/CD composite from room temperature to 450°C.

Also in this case, similar to the nanoconfined materials, the presence of carbon provides a certain degree of reversibility of the dehydrogenation reaction. The minimal efficiency is probably due to the much lower surface area of the discs, allowing only partial surface interaction with the hydrides.

4.14.5 Comparison of the experimental results: LiNa

By comparing the XRD patterns of LiNa/CMK-3 and pure LiNa, a much lower peak intensity is observed however it is clear that some quantity of hydride has not been infiltrated. On the other hand, successful infiltration is confirmed by the pore network properties before and after the infiltration as derived from the N_2 adsorption/desorption isotherms at 77 K. The TPV of the CMK-3 is reduced from 1.2 cm^3/g to 0.21 cm^3/g with a loss of about the 82.5 % of the pore volume. It should be noted that the volume of the borohydride used was 60 % of the CMK-3 pore volume and thus in principle a corresponding reduction of the pore volume was expected. This difference can be attributed to pore blocking caused by the molten phase in a way that some extra closed porosity (inaccessible to N_2 molecules) is created. A similar picture is obtained by examining the dramatic decrease of the BET area of the carbon, from 1250 m^2 to only 170 m^2/g after the melt infiltration. This reduction is even more pronounced (86.5%) in accordance with the pore blocking mechanism. In brief, blocking of smaller pores reduces the BET area more than the pore volume as the surface to volume ratio increases with decreasing pore size. A similar situation is observed for the CA-20 sample.

The TPD-MS results allowed us to resolve the multiple decomposition stages particularly evident in the bulk LiNa, from about 280 °C until the last main dehydrogenation occurring at about 490 °C. Also the role of the carbons on the borohydrides decomposition is highlighted by the TPD-MS results (Figure 72). The presence of a high surface mesoporous carbon such as CMK-3 and CA-20, allows the decomposition to take place at temperatures even 130 °C lower than the bulk hydride mixture, in accordance with previous observations for carbon aerogels. [187] The relative intensity of the two main dehydrogenation signals is maintained, suggesting that all the reactive components are affected by the carbon presence. It is noteworthy that the pore size does not seem to play a predominant role in destabilization, since the results for CMK-3 (5 nm) and CA-20 (25 nm) are similar. We may therefore assume that nanosizing below a certain size cannot improve further the decomposition

kinetics/thermodynamics. In this respect the use of larger pore sizes might be preferable as they are usually connected with larger total pore volumes and thus allow higher loading of the borohydride phase. This in turn leads to lower scaffold dead weight penalty and thus more efficient storage systems. On the other hand, also the composite with the non-porous carbon (LiNa/CD) shows lower decomposition temperatures, with the dehydrogenation events occurring in a range of temperatures between the bulk and the LiNa/CMK or LiNa/CA-20 composites, suggesting an intermediate behavior. Contrary to what is generally believed, the decrease of the decomposition temperature suggests that even without nanoconfinement the carbon somehow provides a kinetic improvement to the decomposition reaction. The inferior performance of LiNa/CD compared to LiNa/CMK may perhaps be explained by the significantly lower surface area of the former.

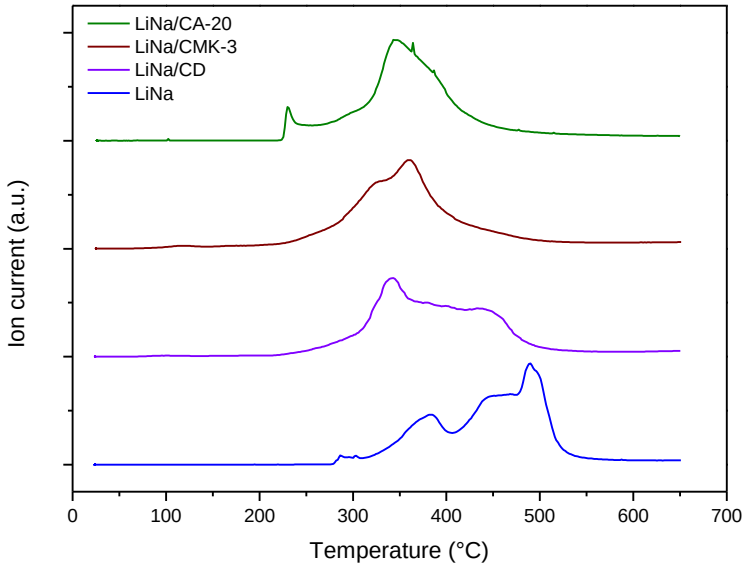

Figure 72: Temperature Programmed Desorption coupled with mass spectrometry (TPD/MS) compared results for LiNa/CA-20 (green), LiNa/CMK-3 (dark red), LiNa/CD (purple) and LiNa (blue).

A similar behavior is observed by the manometric study of the dehydrogenation/rehydrogenation of the samples. While the pure eutectic LiNa mixture decomposes at high temperatures and shows a non-reversible behavior, the carbon composites allow lower decomposition temperatures and provide the system with a certain degree of reversibility. For the case of LiNa/CMK-3 and LiNa/CA-20, it can be seen that after the first two cycles the amount of hydrogen exchanged is constant, with

a H_2 uptake of about 3.5-4 wt%. The carbon discs have a comparable effect on the LiNa but the reversible hydrogen uptake is very limited and doesn't exceed 1.7 wt% of H_2. Unlike the kinetic enhancement that was mainly attributed to the carbon surface, the stability of the system under cycling may be at least attributed also to confinement since the pore network provides a space where extended aggregation is difficult. The reversible part of the LiNa/CD can in this respect be associated with the part of the molten phase that is "bound" to the limited surface of the CDs avoiding thus agglomeration.

4.14.6 $LiBH_4$ – KBH_4 eutectic mixture

The second eutectic mixture studied, similarly to LiNa, was composed for the major fraction by $LiBH_4$, but mixed with KBH_4 instead of $NaBH_4$.

The mixture under analysis was prepared with a molar ratio of $LiBH_4$ and KBH_4 equal to 0.72: 0.28 and it is characterized by having an extremely low melting temperature: 105°C, the lowest among the binary systems with $LiBH_4$.

The eutectic mixture (denoted hereafter as LiK) was prepared following the procedure descripted by Ley et al. [188] starting from the pure borohydrides (Sigma-Aldrich 95%) and KBH_4 (Sigma-Aldrich 98%). Initially hand mixed with pestle and mortar, after mechanically milled in a planetary Fritch P4 mill. The powders were mixed in a tungsten carbide jar with internal volume of 80 ml using 10 mm balls of the same material. The ball milling was performed by milling the sample for 5 minutes at 400 rpm, followed by 2 minutes of pause in a programmed loop for a total milling time of 240 rpm. The sample preparation and the milling itself has been performed under Ar atmosphere in order to avoid any oxidation reaction.

The work on the hydrides was performed entirely in the laboratories of inano at the university of Aarhus, under the supervision of Prof T. R. Jensen.

The phases composition of the post-ball milling eutectic mixture was evaluated through powder X-Ray diffraction and as expected, the presence of $LiBH_4$, KBH_4 and $LiK(BH_4)_2$ has been detected in accordance with literature (Figure 73).[166]

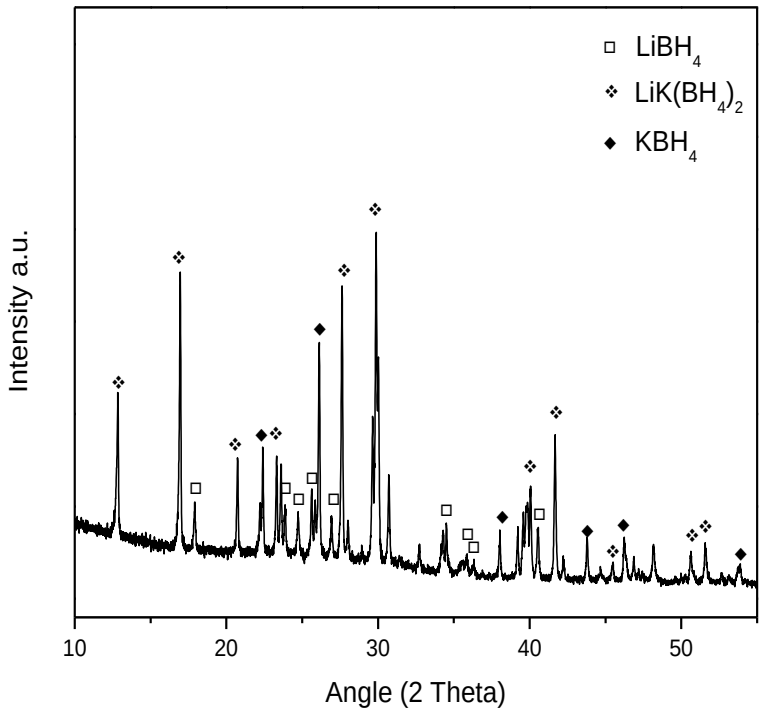

Figure 73: Powder XRD pattern of $LiBH_4$ and KBH_4 (LiK) after ball milling Highlighted peaks relative to: $LiBH_4$ (□), $LiK(BH_4)_2$ (❖) and KBH_4 (◆).

In order to simulate the behaviour of a melt infiltrated hydride, prior the experiment the eutectic mixture has been pre-melted. The ball milled borohydrides were melted in a stainless-steel reactor, where the sample was heated up from room temperature to 125 °C with a heating rate of 3 °C/min and left in isotherm for 30 minutes, the treatment was performed under an initial pressure of ~100 bar of high purity hydrogen (pure at 99.9999%).

The TPD-MS experiment was performed by heating the samples from room temperature to 700 °C with a heating rate of 5 °C/min, under a constant flow of Argon and back-pressure of ~1.4 bar, with the mass spectrometer programmed to detect H_2, B_2H_6, Ar, N_2, O_2, H_2O, CO_2 and NH_3.

From the decomposition of the sample only hydrogen and argon (the carrier gas) were detected. In Figure 74 is represented the ion current generated from the hydrogen that reached the spectrometer concurrently with the thermal decomposition of the sample. The pre-melted hydrides show a first minor release of H_2 near 290 °C, probably related with a phase transition that happens in pure $LiBH_4$ (~280 °C)[147], a main desorption

between 400 °C and 525 °C and a last H_2 release after 550°C in concordance with the literature.[147]

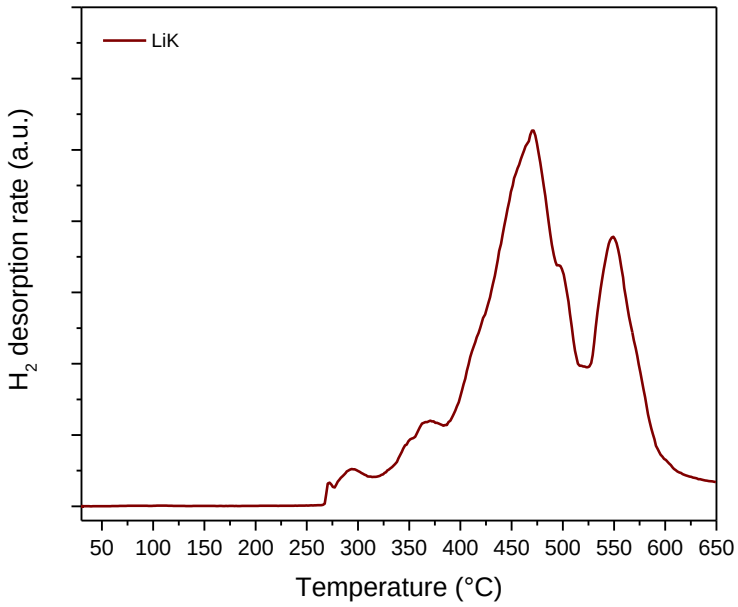

Figure74: TPD/MS results relative to the hydrogen released during the thermal decomposition of LiK.

In order to test the initial sorption capacities and the cyclability of the pure eutectic mixture, a series of dehydrogenation-rehydrogenation cycles have been performed. The experiment took place on a custom made manometric apparatus based on the Sievert's method. It should be noted that, since KBH_4 is not supposed to decompose (melting temperature > 600°C), the maximum amount of H_2 released from the bulk LiK mixture is 9.5 wt%. Moreover, the $LiBH_4$ decomposition is usually incomplete (producing LiH, B and H_2); a maximum of 7.2 wt% is expected in this case. Based on the results from the mass spectrometer it was assumed that the gas released is 100 % hydrogen.

The sample, located in a quartz holder, was heated in a stainless-steel reactor in order to trigger the material decomposition. The treatment involved a 3 °C/min heating ramp, from room temperature to 450 °C under ~1.5 bar of high purity hydrogen (purity 99.9999%), followed by 4 hours isotherm for the dehydrogenation of the material. The rehydrogenation of the material was performed under an initial hydrogen pressure of ~100 bar and the process was performed by heating the sample from room temperature to 400 °C with a rate of 5 °C/min and kept in isothermal conditions for 12 hours. The dehydrogenation-hydrogenation process was performed on the material 5 times, and for

all the cycles the sample was evacuated under dynamic vacuum before and after each sorption treatment.

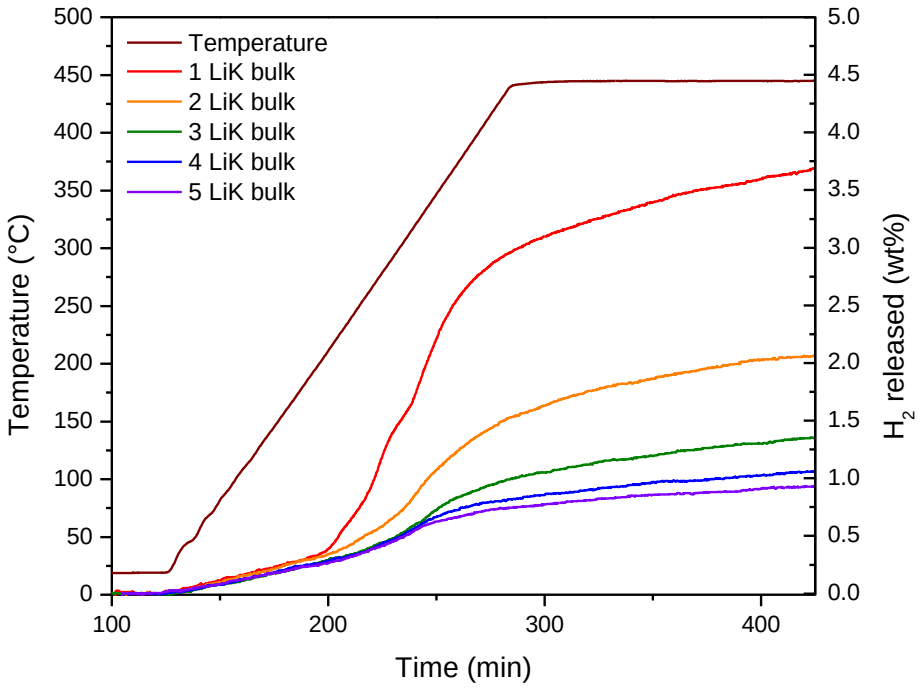

Figure 75: Hydrogen desorption cycles performed on the bulk LiK from room temperature to 450°C.

The 5 dehydrogenation cycles are reported in Figure 75. Pure LiK eutectic mixture released in the first dehydrogenation cycle about 3.6 wt%. However, this percentage drastically drops at every cycle and reaches about 0.9 wt% at the fifth dehydrogenation cycle, highlighting the irreversibility of the pure LiK system as already known.

4.14.7 LiK in mesoporous CMK-3

A composite material (LiK/CMK-3) was obtained by melt infiltrating the same eutectic mixture in CMK-3 mesoporous carbon. The characterization of the plain carbon was performed by N_2 adsorption/desorption isotherms at 77K and as reported before the BET area was 1250 m^2, the total pore volume 1.2 cm^3/g and the QSDFT pore size distribution was centred at 4.6 nm.

The synthesis of the composite material was performed by infiltrating in the carbon scaffold an amount of LiK (ρ = 0.86 g/cm^3) calculated to be the 60 % of the TPV of the CMK-3 carbon (1.2 cm^3/g). The infiltration was performed by manually mixing carbon

and LiK (weight ratio CMK-3 – LiK 1.59:1) to obtain a homogeneous mixture and then melting the hydrides in a stainless-steel reactor under hydrogen back-pressure. The melting process was performed by heating the carbon-hydrides mixture from room temperature to 125 °C with a heating rate of 3 °C/min and keeping the sample at isothermal conditions for 30 minutes, in order to let the melted hydrides penetrate into the pores of the scaffold. The samples were handled in glove box, under inert atmosphere of argon, while during the whole infiltration process, the sample in the reactor was kept under an initial backpressure of 100 bar of high purity hydrogen in order to avoid any decomposition reaction.

In order to evaluate quality and quantity of infiltration, a series of analyses have been performed. Power X-ray diffraction technique was used to evaluate the presence of crystalline material outside of the carbon scaffold after the infiltration. As shown in the pattern below (Figure 76), all the typical crystal peaks of the bulk borohydrides are not detectable in the composite material, proving that no crystalline borohydride is outside of the pores.

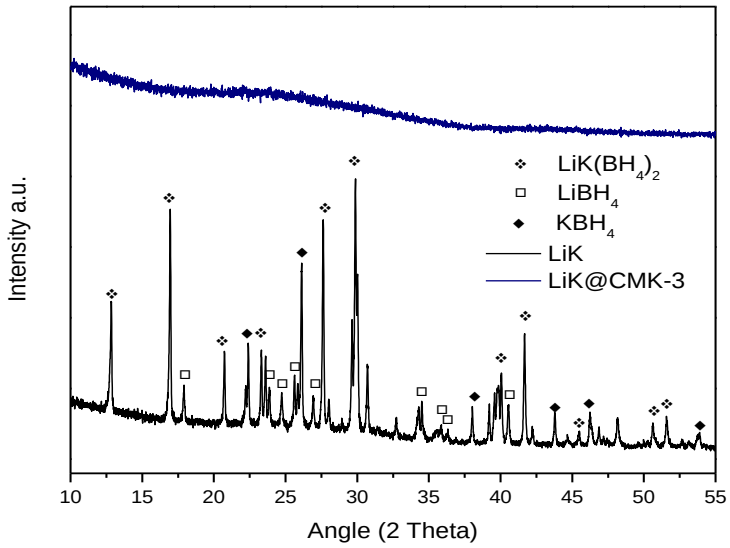

Figure 76: Bottom: powder X-ray diffraction pattern of the bulk LiK eutectic mixture after milling (black line); the typical peaks relative to: $LiK(BH_4)_2$ (❖),$LiBH_4$ (□) and KBH_4 (◆) are labelled Top: diffraction pattern of the composite material LiK/CMK-3.

The alteration of the porous structure of the carbon after melt infiltration was studied by N_2 adsorption/desorption isotherms at 77 K (Figure 77). The melt infiltration with LiK led to a significant change of the pore properties. Indeed, the LiK/CMK-3 material exhibited a BET area of 490 m^2/g and a TPV of 0.5 cm^3/g (both calculated on a pure carbon basis). As in the case of LiNa, the mean pore size remains unchanged. This is also explained by the non-wetting character of the LiK phase that forms discrete particles which reduce the accessible pore volume, but do not alter the size of the open pores (see inset of Figure 77b).

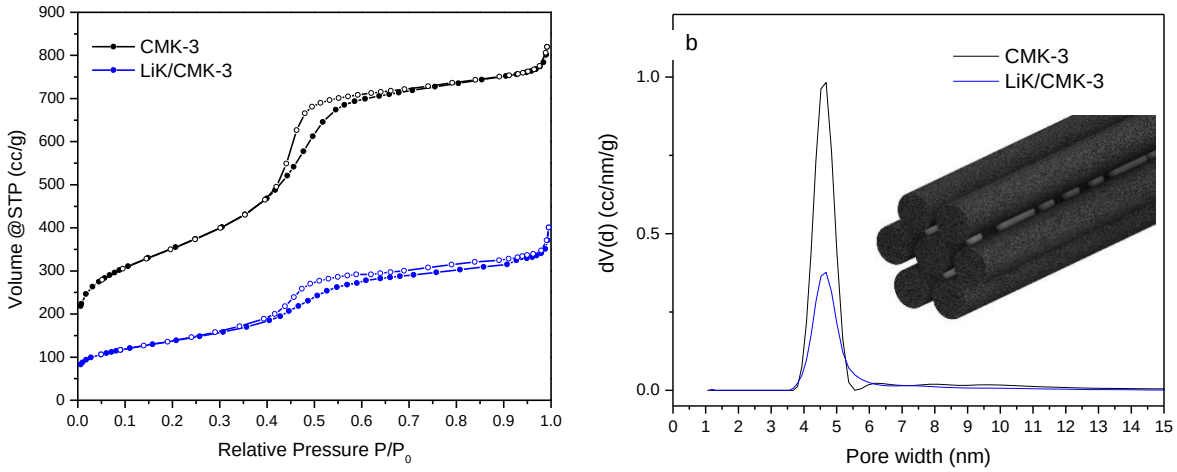

Figure 77: Left: N_2 adsorption/desorption isotherms at 77 K on CMK-3 carbon (black line) and on the composite material LiK/CMK-3 (blue line). Right: pore size distribution of CMK-3 carbon (black) and of LiK/CMK-3 (blue) obtained through NLDFT calculations, showing a narrow distribution centred on diameters of about 4.5 nm. Inset: 3D model of melt infiltrated CMK-3.

The nanoconfinement effect of on the desorption temperatures of the borohydrides has been tested with thermal programmed decomposition coupled with gas spectrometry (TPD-MS), with the aid of the same instrument and procedure used for the bulk material and described before. The sample was loaded in a quartz sample holder and heated from room temperature to 700 °C, with a rate of 5 °C/min under a constant flow of Ar and a backpressure of ~1.4 bar. The released gasses were analysed with the Mass Spectrometer programmed to detect the m/z values corresponding to H_2, B_2H_6, Ar, N_2, O_2, H_2O and CO_2; however only hydrogen was detected along with the carrier gas (Argon). The hydrogen release of the composite material, unlike bulk LiK, shows practically only one hydrogen desorption peak with smooth signals of side reactions at lower and higher temperature. The release of hydrogen starts at 180 °C, about 110 °C

lower than the bulk, with the main peak at 360 °C (~130 °C lower than pure LiK) (Figure 78).

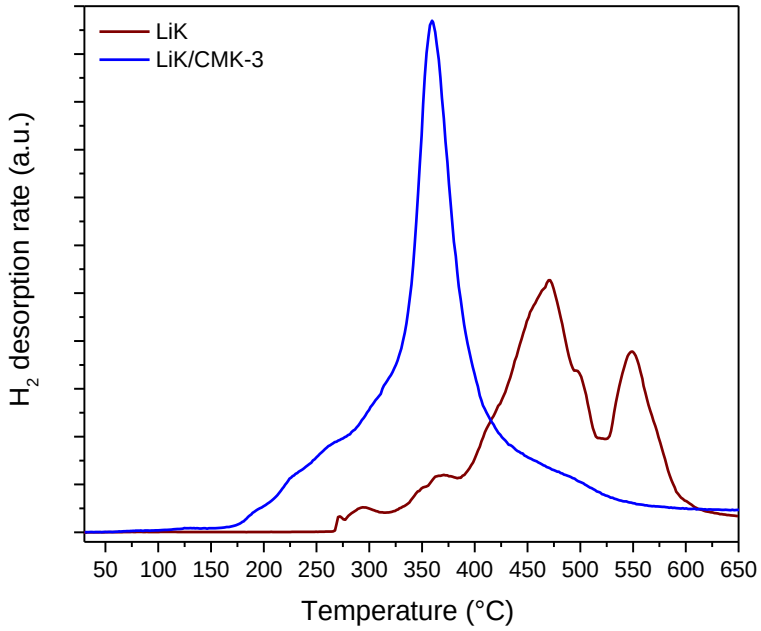

Figure 78: Temperature programmed desorption with mass spectrometry (TPD/MS) results for bulk LiK mixture (dark red) and LiK/CMK-3 composite (blue).

By following the same procedure applied to the bulk LiK, the cycling capacity of CMK-3 infiltrated LiK was also tested, revealing a much better performance than the bulk. As shown in Figure 79, the composite released about 6.7 wt% of hydrogen (calculated over the respective LiK mass) during the first dehydrogenation. Furthermore, in this case, the hydrogen released decreases drastically after the first dehydrogenation, but it stabilises right after the second cycle, releasing more than 2.6 wt% of hydrogen in all the subsequent cycles.

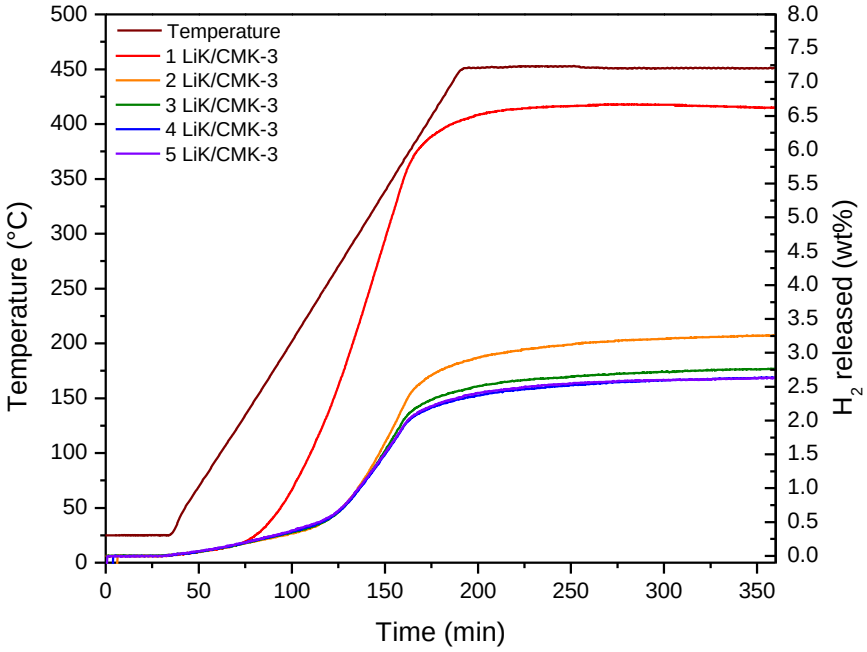

Figure 79: Hydrogen desorption cycles performed on the composite material LiK/CMK-3 from room temperature to 450°C.

4.14.8 LiK on carbon aerogel

The composite LiK/CA-20 was obtained through infiltrating LiK in the CA-20 carbon aerogel according to the method described in the section 4.6. The amount of hydrides and carbon were calculated in order to fill 60 % of the total pore volume of the carbon (TPV=1.37 cm^3/g).

Porosimetric analyses were performed on the composite material using the same methods adopted for the pure carbon. After 30 minutes of infiltration however, only a minor drop of pore volume is observed (LiK/CA-20 TPV= 1.25 cm^3/g) suggesting that a minor part of the hydride filled the pores (Figure 80).

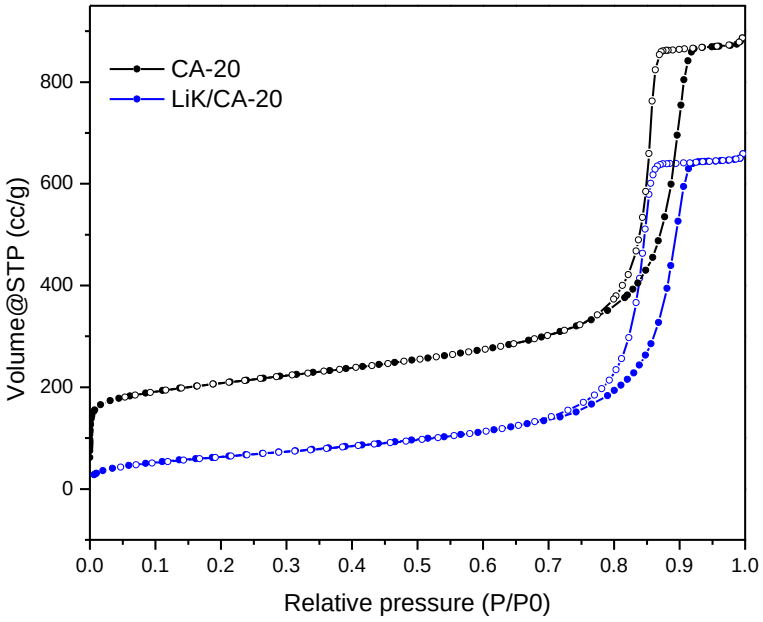

Figure 80: N_2 adsorption/desorption isotherms performed at 77 K on CA-20 (black) and LiK/CA-20 (blue)

Thermal programmed desorption gas spectrometry (TPD-MS) experiments have been performed on the LiK/CA-20 composite by using same apparatus and procedure as for the bulk material. In the same way the instrument was programmed to detect all the m/z values corresponding to H_2, B_2H_6, Ar, N_2, O_2, H_2O, and CO_2 in the range of temperatures between 25 and 700 °C. Also in this case, hydrogen was the only gas detected. With the material releasing H_2 at temperatures similar to those reported for the LiK/CMK-3 and about 100 °C lower than the bulk LiK (Figure 81).

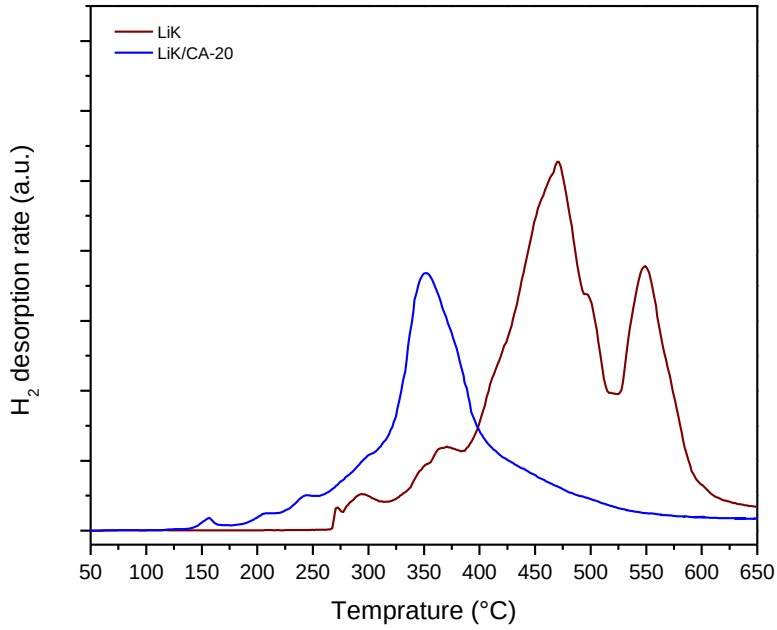

Figure 81: Temperature Programmed Desorption coupled with mass spectrometry (TPD/MS) results for LiK (dark red) and LiK/CA-20 (blue).

The sorption capacity and cyclability of the LiK/CA-20 composite were tested with a manometric device, described before. The dehydrogenation phase of the experiment was performed by heating the sample from room temperature to 450 °C under ~ 1.5 bar of initial pressure, the rehydrogenation was carried out by heating the sample to 400 °C under 100 bar of H_2. The outcome, reported in the plot below, shows the release of 7.7 wt% of hydrogen during the first dehydrogenation followed by a constant uptake of H_2 between 3 and 4 wt% during the following four cycles (Figure 82).

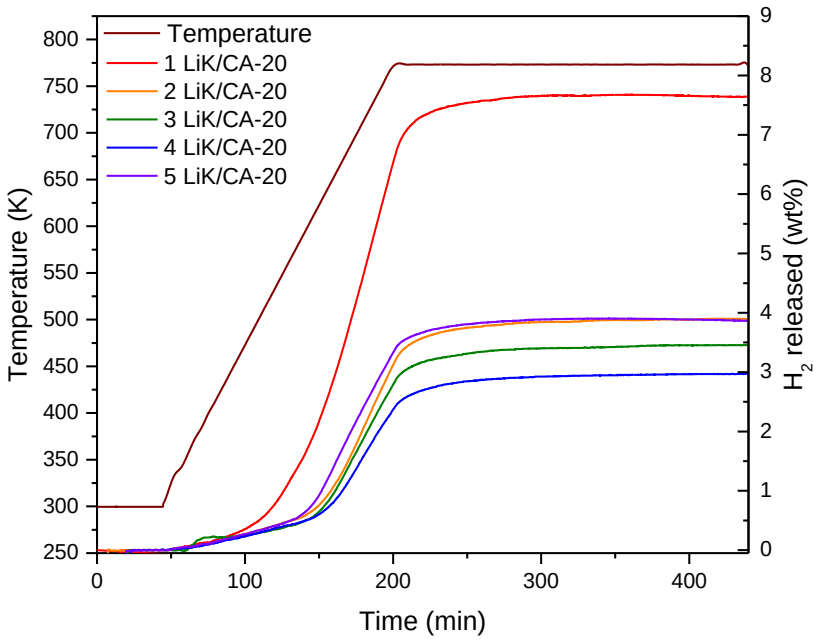

Figure 82: Hydrogen desorption cycles performed on the composite material LiK/CMK-3 from room temperature to 450°C

4.14.9 LiK on non-porous graphitic carbon

In order to understand if the drastic decrease of the dehydrogenation temperatures is due to the nanoconfinement and not to a catalytic effect related to the contact with the carbon surface a series of experiments using non-porous carbon was performed. For this purpose, commercial non-porous graphitic carbon disks were used to synthesize the LiK/CD composite materials using the same synthetic methods adopted for the LiK/CMK-3 and LiK/CA-20 samples.

The composite material was prepared by manually mixing carbon disks and hydrides with pestle and mortar until a homogeneous mixture was obtained. The composition of the mixture had the same mass ratio adopted in the LiK/CMK-3 preparation (carbon-LiK = 1.59:1). The mixture obtained was then heated in a stainless-steel reactor heating the sample to 125 °C for 30 minutes under a back pressure of 100 bar of hydrogen, in order to simulate the infiltration treatment.

The effects of the non-porous carbon on the hydrides were tested with TPD-MS experiment (Figure 83). The sample was heated from room temperature to 700 °C under a constant stream of argon. The only gas detected during the experiment was hydrogen. The thermal decomposition of the sample takes place in a multistep reaction, with the first minor dehydrogenations at about 240 and 270 °C, followed by a series of

the main decomposition events at 320, 365 and 430 °C. Overall, decomposition temperatures of about 150 °C lower than the bulk LiK were recorded.

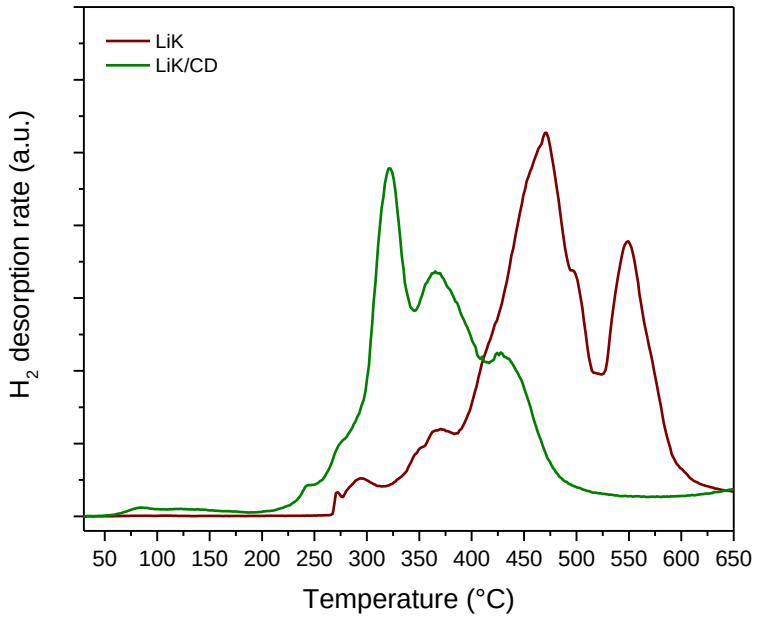

Figure 83: Temperature Programmed Desorption coupled with mass spectrometry (TPD/MS) results for LiK (dark red) and LiK/CD (green).

The cyclability of LiK/CD was tested with a series of dehydrogenation-rehydrogenation cycles in a manometric apparatus with the same procedure of the other LiK based materials. In order to trigger the dehydrogenation reaction, the samples were heated in a stainless-steel reactor with a 3 °C/min heating ramp, from room temperature to 450 °C under a backpressure of hydrogen (~1.5 bar) and then kept at the same temperature for about 4 hours. The rehydrogenation reaction was achieved by heating the samples with a fast rate of 5 °C/min up to 400 °C and keeping the same temperature for about 12 hours. As for all the samples, 5 cycles of hydrogenation/dehydrogenation were performed. Based on the TPD-MS results it can be safely assumed that only hydrogen is released. Even for the first dehydrogenation a lower amount of hydrogen (about 2.7 wt%) compared to LiK/CMK-3 and even the bulk material is released. Moreover, in close analogy with the bulk, the amount of hydrogen released at each cycle decrease; about 1.3 wt% at the second dehydrogenation, 1 wt% at the third to around 0.7 wt% at the fifth cycle (Figure 84). The behaviour observed lead to the conclusion that the presence of the non-porous carbon does not affect the reversibility of the system, suggesting thus that pore nanoconfinement can indeed enhance the LiK cyclability.

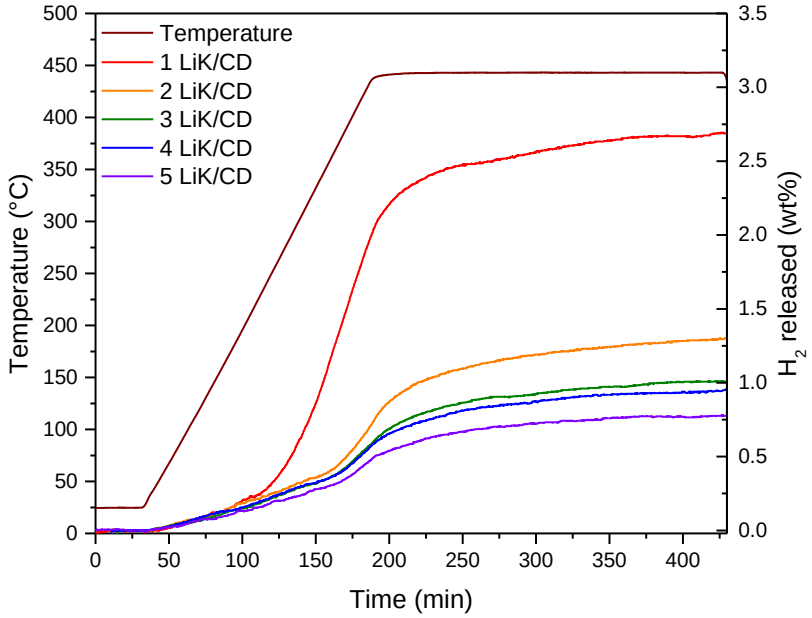

Figure 84: Kinetics of cycling of LiK/CD.

4.14.10 Comparison of the experimental results: LiK

The comparison of the PXRD patterns of the bulk LiK and the LiK/CMK-3 composite proves that the entire hydride permeated in the CMK-3 pores through capillarity. A further confirmation of the successful infiltration of the LiK material within the CMK-3 porous structure was provided by the study of the pore properties of the system before and after the melt infiltration. It should be noted at this point that the results presented have been normalized to pure carbon basis (i.e. the reduction of surface area and pore volume due to the “dead-weight” of LiK is not considered). Especially the reduction of the TPV by almost 58% in the case of the LiK/CMK-3 composite shows that almost the whole amount of LiK used permeated inside the carbon pores rendering part of the porous network inaccessible to N_2. The pore size distribution of the pristine and melt infiltrated CMK-3 carbon are centred on similar sizes suggesting that infiltration proceeds by pore filling (that blocks pores) rather than surface film development (that make the pores narrower). Partial pore blocking is also suggested by the minute yet observable hysteresis at higher pressures that is developed in the infiltrated sample.

The presence of carbon allows the sample to release hydrogen at much lower temperatures than the bulk. From the TPD-MS experiments both LiK/CD, LiK/CA-20 and LiK/CMK-3 show their main decomposition at a temperature about 150 °C lower

than the pure hydrides mixture. This behaviour is most probably of kinetic nature, and related to either a catalytic effect of the carbon surfaces on the hydrides or facilitated heat transfer through the sample due to the higher thermal conductivity of the carbon. The non-confined carbon composite maintains a multipeak pattern similar to the bulk, on the other hand, for the LiK-CMK-3 and LiK/CA-20 the decomposition reactions converge in one main dehydrogenation peak.

The manometric cycling have revealed additional information on the performance of the bulk and the carbon composites. The bulk also in these analyses shows a multi-stage release pattern, especially during the first dehydrogenation, which is lost in the carbon composites. During decomposition all the samples show an initial high hydrogen release followed by a second cycle with only a fraction of the initial gas released, suggesting the presence of an irreversible reaction involved. Taking into account that the wt% are referred to the only LiK weight, both bulk and the non-porous composite release a comparable amount of hydrogen (around 3 wt%) which drops to around 0.8 wt% at the fifth cycle. A much-improved behaviour is registered by the nanoconfined composite LiK/CMK-3 and LiK/CA-20 able to release about 7 wt% of hydrogen (calculated over the respective LiK mass) during the first dehydrogenation. Also in this case the hydrogen released decreases drastically after the first dehydrogenation, but it stabilises right after the second cycle, releasing around 3 wt% of hydrogen in the subsequent cycles.

The enhanced performance of the nanoconfined LiK may be associated with many factors, however the increased stability of the system is probably related with the protection offered by the porous network since particle aggregation is severely hindered by the pore walls. Additionally, while decomposing $LiBH_4$ releases gaseous and toxic diborane (B_2H_6) that at high temperatures further decomposes in B and H_2. Diborane can also react with $LiBH_4$ to generate stable closoboranes such as $Li_2B_{10}H_{10}$ and $Li_2B_{12}H_{12}$, with a direct negative effect on the overall capacity[335–337] as already mentioned. In this respect the improved reversibility of the LiK/CMK-3 and LiK/CA-20 system may be related to the fact that in nanopores the release of diborane is totally suppressed or drastically reduced. [338,339]

CHAPTER 5
CONCLUSIONS

The low melting temperature of the $LiBH_4/NaBH_4$ eutectic mixture allowed the nanoconfinement of the hydrides in 5 nm diameter carbon pores of a CMK-3 type carbon, 25 nm pores of CA-20 carbon aerogel as well as the synthesis of a borohydride/non-porous carbon composite. From both the porous and non-porous systems an improvement on the sorption-release properties over the pure hydrides was observed. All the carbon composites have a direct influence over the kinetics of decomposition with the effect being more obvious for the nanoconfined material. Moreover, the presence of carbon increased the reaction reversibility compared to the bulk material. The nanoconfined LiNa shows a consistent uptake of H_2 of about 3.5 wt% after five hydrogenation/dehydrogenation cycles. It is noteworthy that the cycling enhancement seems to be unrelated to the pore size of the scaffold, implying that below a certain pore size not further improvement is possible. A similar behaviour but with minor intensity is revealed by the composite material with non-porous carbon, which can exchange about 1.7 wt% of H_2 after five cycles. Overall, for the case of LiNa, the kinetic improvement observed for the carbon composite materials is probably associated with surface catalytic interactions, while reversibility is rather based on the confinement of the borohydride in nanosized pores.

The melt infiltration of the $LiBH_4/KBH_4$ eutectic mixture in an ordered mesoporous carbon of CMK-3 type (pore diameter ~5 nm) and a carbon aerogel (CA-20, pore diameter ~25 nm) led to the development of composite systems with improved hydrogen storage properties. Pore confinement resulted in a substantial decrease of the decomposition temperature (more than 100 °C) of the starting borohydride mixture. Quite interestingly, the composite systems also showed a constant uptake of H_2 around 3 wt% for at least 5 hydrogenation-dehydrogenation cycles, upturning to a significant degree the irreversibility of the dehydrogenation reaction of the bulk LiK mixture. This improved performance in terms of reversibility and kinetics may be associated with the combined effect of the catalytic action of the carbon surface, the nano-sizing of borohydride particles, or the limitation of irreversible side-reactions such as those leading to the formation of diboranes and closoboranes.

TABLE OF ABBREVIATIONS

BET	Brunauer – Emmett - Teller
CA	Carbon Aerogel
CD	Carbon Disks
CMC	Critical Micelle Concentration
CMK	Carbon Mesostructured from Korea
COF	Covalent Organic Framework
EISA	Evaporation Induced Self Assembly
FC	Fuel Cell
FTIR	Fourier-Transform Infrared spectroscopy
HCP	Hypercrosslinked Polymers
IUPAC	International Union of Pure and Applied Chemistry
LiK	$LiBH_4$ – KBH_4 eutectic mixture
LiNa	$LiBH_4$ – $NaBH_4$ eutectic mixture
MCN	Mesoporous Carbon Nanospheres
MOF	Metal Organic Framework
MS	Mass Spectrometry
MSC	Molecular Sieving Carbon
NASA	National Aeronautics and Space Administration
NIST	National Institute of Standards and Technology
NMR	Nuclear Magnetic Resonance
PIM	Polymer of Intrinsic Microporosity
PEO	Polyethylene oxide
PID	Proportional Integral Derivative
PPO	Polypropylene oxide
PTFE	Polytetrafluoroethylene
PVC	Polyvinyl chloride
PXRD	Powder X-Ray Diffraction
QSDFT	Quenched Solid Density Functional Theory
RPM	Revolutions Per Minute
SAXS	Small Angle X-ray Scattering
SBA	Santa Barbara Amorphous
SEM	Scanning Electron Microscope
TEOS	Tetraethyl orthosilicate
TPD	Temperature Programmed Desorption
TPV	Total Pore Volume

Bibliography

1. S. Bilgen. Structure and Environmental Impact of Global Energy Consumption. *Renewable and Sustainable Energy Reviews*, vol. 38, 2014, pp. 890–902.

2. A. E. Kontorovich, M. I. Epov, and L. V. Eder. Long-Term and Medium-Term Scenarios and Factors in World Energy Perspectives for the 21st Century. *Russian Geology and Geophysics*, vol. 55, nos. 5–6, 2014, pp. 534–543.

3. REN21. *Renewables 2015-Global Status Report*. 2015.

4. D. P. van Vuuren, E. Stehfest, D. E. H. J. Gernaat, J. C. Doelman, M. van den Berg, M. Harmsen, H. S. de Boer, L. F. Bouwman, V. Daioglou, O. Y. Edelenbosch, B. Girod, T. Kram, L. Lassaletta, P. L. Lucas, H. van Meijl, C. Müller, B. J. van Ruijven, S. van der Sluis, and A. Tabeau. Energy, Land-Use and Greenhouse Gas Emissions Trajectories under a Green Growth Paradigm. *Global Environmental Change*, vol. 42, 2017, pp. 237–250.

5. N. Apergis, and J. E. Payne. Renewable Energy Consumption and Economic Growth: Evidence from a Panel of OECD Countries. *Energy Policy*, vol. 38, no. 1, 2010, pp. 656–660.

6. S. Sen, S. Ganguly, A. Das, J. Sen, and S. Dey. Renewable Energy Scenario in India: Opportunities and Challenges. *Journal of African Earth Sciences*, vol. 122, no. June, 2016, pp. 25–31.

7. S. Sen, and S. Ganguly. Opportunities, Barriers and Issues with Renewable Energy Development – A Discussion. *Renewable and Sustainable Energy Reviews*, vol. 69, no. June 2015, 2017, pp. 1170–1181.

8. P. S. Georgilakis. Technical Challenges Associated with the Integration of Wind Power into Power Systems. *Renewable and Sustainable Energy Reviews*, vol. 12, no. 3, 2008, pp. 852–863.

9. D. Heide, L. von Bremen, M. Greiner, C. Hoffmann, M. Speckmann, and S. Bofinger. Seasonal Optimal Mix of Wind and Solar Power in a Future, Highly Renewable Europe. *Renewable Energy*, vol. 35, no. 11, 2010, pp. 2483–2489.

10. G. Giannakoudis, A. I. Papadopoulos, P. Seferlis, and S. Voutetakis. Optimum Design and Operation under Uncertainty of Power Systems Using Renewable Energy Sources and Hydrogen Storage. *International Journal of Hydrogen Energy*, vol. 35, no. 3, 2010, pp. 872–891.

11. S. Weitemeyer, D. Kleinhans, T. Vogt, and C. Agert. Integration of Renewable Energy Sources in Future Power Systems: The Role of Storage. *Renewable Energy*, vol. 75, 2015, pp. 14–20.

12. M. Ball, and M. Weeda. The Hydrogen Economy - Vision or Reality? *International Journal of Hydrogen Energy*, vol. 40, no. 25, 2015, pp. 7903–7919.

13. J. M. Ogden. Hydrogen: The Fuel of the Future? *Physics Today*, vol. 55, no. 4, 2002, p. 69.

14. A. Zuttel, A. Remhof, A. Borgschulte, and O. Friedrichs. Hydrogen: The Future Energy Carrier. *Philosophical Transactions of the Royal Society A: Mathematical, Physical and Engineering Sciences*, vol. 368, no. 1923, 2010, pp. 3329–3342.

15. G. Kopp, and J. L. Lean. A New, Lower Value of Total Solar Irradiance: Evidence and Climate Significance. *Geophysical Research Letters*, vol. 38, no. 1, 2011, pp. 1–7.

16. F. A. Cotton, and G. Wilkinson. Advanced Inorganic Chemistry: A Comprehensive Text. *Advanced Inorganic Chemistry*. 657–669. http://dx.doi.org/10.1016/j.jaap.2011.11.019.

17. T. Saito. *Inorganic Chemistry*. Kanagawa University, 2014, 6th Editio.

18. J. D. Lee. *Concise Inorganic Chemistry*. 1999, Fourth Edi, C. & Hall, ed.Chapman & Hall.

19. D. Perlov, and A. Vilenkin. Cosmology for the Curious. 2017, pp. 187–199.

20. J. W. Erisman, M. A. Sutton, J. Galloway, Z. Klimont, and W. Winiwarter. How a Century of Ammonia Synthesis Changed the World. *Nature Geoscience*, vol. 1, no. 10, 2008, pp. 636–639.

21. H. H. Storch, and A. R. Olson. The Synthesis of Ammonia from Its Elements in the Low-Voltage Arc. *Journal of the American Chemical Society*, vol. 45, no. 7, 1923, pp. 1605–1614.

22. R. R. Allen. Principles and Catalysts for Hydrogenation of Fats and Oils. *Journal of the American Oil Chemists' Society*, vol. 55, no. 11, 1978, pp. 792–795.

23. U. Romano, R. Tesel, M. M. Mauri, and P. Rebora. Synthesis of Dimethyl Carbonate from Methanol, Carbon Monoxide, and Oxygen Catalyzed by Copper Compounds. *Industrial and Engineering Chemistry Product Research and Development*, vol. 19, no. 3, 1980, pp. 396–403.

24. R. Pohl, A. Antognini, F. Nez, F. D. Amaro, F. Biraben, J. M. R. Cardoso, D. S. Covita, A. Dax, S. Dhawan, L. M. P. Fernandes, A. Giesen, T. Graf, T. W. Hänsch, P. Indelicato, L. Julien, C. Y. Kao, P. Knowles, E. O. Le Bigot, Y. W. Liu, J. A. M. Lopes, L. Ludhova, C. M. B. Monteiro, F. Mulhauser, T. Nebel, P. Rabinowitz, J. M. F. Dos Santos, L. A. Schaller, K. Schuhmann, C. Schwob, D. Taqqu, J. F. C. A. Veloso, and F. Kottmann. The Size of the Proton. *Nature*, vol. 466, no. 7303, 2010, pp. 213–216.

25. C. M. Kalamaras, and a. M. Efstathiou. Hydrogen Production Technologies: Current State and Future Developments. *Conference Papers in Energy*, vol. 2013, 2013, p. 9.

26. C. Ghergheleş, and V. Ghergheleş. Hydrogen - the Fuel of the Future? *Journal of Electrical and Electronics Engineering*, vol. 1, no. 1, 2008, pp. 51–53.

27. A. Kirubakaran, S. Jain, and R. K. Nema. A Review on Fuel Cell Technologies and Power Electronic Interface. *Renewable and Sustainable Energy Reviews*, vol. 13, no. 9, 2009, pp. 2430–2440.

28. A. Boudghene Stambouli, and E. Traversa. Fuel Cells, an Alternative to Standard Sources of Energy. *Renewable and Sustainable Energy Reviews*, vol. 6, no. 3, 2002, pp. 297–306.

29. M. Hirscher. *Handbook of Hydrogen Storage*. Wiley-VCH Verlag GmbH & Co. KGaA, Weinheim, Germany, 2010, M. Hirscher, ed.Michael Hirscher.

30. S. Niaz, T. Manzoor, and A. H. Pandith. Hydrogen Storage: Materials, Methods and Perspectives. *Renewable and Sustainable Energy Reviews*, vol. 50, 2015, pp. 457–469.

31. U.S. DRIVE. Target Explanation Document:Onboard Hydrogen Storage for Light-Duty Fuel Cell Vehicles. no. May, 2015, pp. 1–22.

32. A. Züttel. Materials for Hydrogen Storage. *Materials Today*, vol. 6, no. 9, 2003, pp. 24–33.

33. G. Wang, J. Zhou, S. Hu, S. Dong, and P. Wei. Investigations of Filling Mass with the Dependence of Heat Transfer during Fast Filling of Hydrogen Cylinders. *International Journal of Hydrogen Energy*, vol. 39, no. 9, 2014, pp. 4380–4388.

34. D. Chapelle, and D. Perreux. Optimal Design of a Type 3 Hydrogen Vessel: Part i - Analytic Modelling of the Cylindrical Section. *International Journal of Hydrogen Energy*, vol. 31, no. 5, 2006, pp. 627–638.

35. N. De Miguel, R. Ortiz Cebolla, B. Acosta, P. Moretto, F. Harskamp, and C. Bonato. Compressed Hydrogen Tanks for On-Board Application: Thermal Behaviour during Cycling. *International Journal of Hydrogen Energy*, vol. 40, no. 19, 2015, pp. 6449–6458.

36. J. P. Berro Ramirez, D. Halm, J. C. Grandidier, S. Villalonga, and F. Nony. 700 Bar Type IV High Pressure Hydrogen Storage Vessel Burst - Simulation and Experimental Validation. *International Journal of Hydrogen Energy*, vol. 40, no. 38, 2015, pp. 13183–13192.

37. A. Leon. Hydrogen Storage. In *Hydrogen Technology*, 2008, pp. 81–128.

38. B. Dawoud, E. Amer, and D. Gross. Experimental Investigation of an Adsorptive Thermal Energy Storage. *International journal of energy research*, vol. 31, no. August 2007, 2007, pp. 135–147.

39. G. Karagiorgis, C. N. Christodoulou, H. von Storch, G. Tzamalis, K. Deligiannis, D. Hadjipetrou, M. Odysseos, M. Roeb, and C. Sattler. Design, Development, Construction and Operation of a Novel Metal Hydride Compressor. *International Journal of Hydrogen Energy*, vol. 42, no. 17, 2017, pp. 12364–12374.

40. J. Dewar. Liquid Hydrogen. *Science*, vol. 11, no. 278, 1900, pp. 641–651.

41. S. Krasae-in, J. H. Stang, and P. Neksa. Development of Large-Scale Hydrogen Liquefaction Processes from 1898 to 2009. *International Journal of Hydrogen Energy*, vol. 35, no. 10, 2010, pp. 4524–4533.

42. S. S. Makridis. Hydrogen Storage and Compression. In *Methane and Hydrogen for Energy Storage*, 2016, pp. 1–28.

43. M. Rzepka, P. Lamp, and M. A. de la Casa-Lillo. Physisorption of Hydrogen on

Microporous Carbon and Carbon Nanotubes. *J. Phys. Chem. B.*, vol. 102, 1998, pp. 10894–10898.

44. R. A. Varin, T. Czujko, and Z. S. Wronski. *Nanomaterials for Solid State Hydrogen Storage*. 2009.

45. S. Hynek. Hydrogen Storage by Carbon Sorption. *International Journal of Hydrogen Energy*, vol. 22, no. 6, 1997, pp. 601–610.

46. A. C. Dillon, K. M. Jones, T. A. Bekkedahl, C. H. Kiang, D. S. Bethune, and M. J. Heben. Storage of Hydrogen in Single-Walled Carbon Nanotubes. *Nature*. 6623. Volume 386, 377–379.

47. M. Hirscher, and M. Becher. Hydrogen Storage in Carbon Nanotubes. *Journal of Nanoscience and Nanotechnology*, vol. 3, no. 1, 2003, pp. 3–17.

48. C. D. Wood, T. Bien, A. Trewin, N. Hongjun, D. Bradshaw, M. J. Rosseinsky, Y. Z. Khimyak, N. L. Campbell, R. Kirk, E. Stöckel, and A. I. Cooper. Hydrogen Storage in Microporous Hypercrosslinked Organic Polymer Networks. *Chemistry of Materials*, vol. 19, no. 8, 2007, pp. 2034–2048.

49. N. B. McKeown, and P. M. Budd. Polymers of Intrinsic Microporosity (PIMs): Organic Materials for Membrane Separations, Heterogeneous Catalysis and Hydrogen Storage. *Chemical Society Reviews*, vol. 35, no. 8, 2006, p. 675.

50. J. G. Vitillo, G. Ricchiardi, G. Spoto, and A. Zecchina. Theoretical Maximal Storage of Hydrogen in Zeolitic Frameworks. *Physical chemistry chemical physics : PCCP*, vol. 7, 2005, pp. 3948–3954.

51. B. Panella, and M. Hirscher. Hydrogen Physisorption in Metal-Organic Porous Crystals. *Advanced Materials*, vol. 17, no. 5, 2005, pp. 538–541.

52. H. Furukawa, N. Ko, Y. B. Go, N. Aratani, S. B. Choi, E. Choi, A. Ö. Yazaydin, R. Q. Snurr, M. O'Keeffe, J. Kim, and O. M. Yaghi. Ultrahigh Porosity in Metal-Organic Frameworks. *Science*, vol. 329, no. 5990, 2010, pp. 424–428.

53. D. P. Broom, C. J. Webb, K. E. Hurst, P. A. Parilla, T. Gennett, C. M. Brown, R. Zacharia, E. Tylianakis, E. Klontzas, G. E. Froudakis, T. A. Steriotis, P. N. Trikalitis, D. L. Anton, B. Hardy, D. Tamburello, C. Corgnale, B. A. van Hassel, D. Cossement, R. Chahine, and M. Hirscher. Outlook and Challenges for Hydrogen Storage in Nanoporous Materials. *Applied Physics A: Materials Science and*

Processing, vol. 122, no. 3, 2016, pp. 1–21.

54. A. Ahmed, S. Seth, J. Purewal, A. G. Wong-Foy, M. Veenstra, A. J. Matzger, and D. J. Siegel. Exceptional Hydrogen Storage Achieved by Screening Nearly Half a Million Metal-Organic Frameworks. *Nature Communications*, vol. 10, no. 1, 2019.

55. A. Ahmed, and D. J. Siegel. Predicting Hydrogen Storage in MOFs via Machine Learning. *Patterns*, vol. 2, no. 7, 2021, p. 100291.

56. O. K. Farha, C. E. Wilmer, I. Eryazici, B. G. Hauser, P. A. Parilla, K. ONeill, A. A. Sarjeant, S. T. Nguyen, R. Q. Snurr, and J. T. Hupp. Designing Higher Surface Area Metal-Organic Frameworks: Are Triple Bonds Better than Phenyls? *Journal of the American Chemical Society*, vol. 134, no. 24, 2012, pp. 9860–9863.

57. Z. Chen, K. O. Kirlikovali, P. Li, and O. K. Farha. Reticular Chemistry for Highly Porous Metal-Organic Frameworks: The Chemistry and Applications. *Accounts of Chemical Research*, vol. 55, no. 4, 2022, pp. 579–591.

58. Y. Li, and R. T. Yang. Gas Adsorption and Storage in Metal-Organic Framework MOF-177. *Langmuir*, vol. 23, no. 26, 2007, pp. 12937–12944.

59. K. Koh, J. D. Van Oosterhout, S. Roy, A. G. Wong-Foy, and A. J. Matzger. Exceptional Surface Area from Coordination Copolymers Derived from Two Linear Linkers of Differing Lengths. *Chemical Science*, vol. 3, no. 8, 2012, pp. 2429–2432.

60. A. Züttel. Hydrogen Storage Methods. *Naturwissenschaften*, vol. 91, no. 4, 2004, pp. 157–172.

61. P. Englezos. Clathrate Hydrates. *Industrial & Engineering Chemistry Research*, vol. 32, no. 7, 1993, pp. 1251–1274.

62. W. L. Vos, L. W. Finger, R. J. Hemley, and H. K. Mao. Novel H_2-H_2O Clathrates at High Pressures. *Physical Review Letters*, vol. 71, no. 19, 1993, pp. 3150–3153.

63. W. L. Mao, and H. -k. Mao. Hydrogen Storage in Molecular Compounds. *Proceedings of the National Academy of Sciences*, vol. 101, no. 3, 2004, pp. 708–710.

64. L. J. Florusse, C. J. Peters, J. Schoonman, K. C. Hester, C. A. Koh, S. F. Dec, K. N. Marsh, and E. D. Sloan. Stable Low-Pressure Hydrogen Clusters Stored in a Binary Clathrate Hydrate. *Science*, vol. 306, no. 5695, 2004, pp. 469–471.

65. Y. H. Hu, and E. Ruckenstein. Clathrate Hydrogen Hydrate - A Promising Material for Hydrogen Storage. *Angewandte Chemie - International Edition*, vol. 45, no. 13, 2006, pp. 2011–2013.

66. H. Lee, J. W. Lee, D. Y. Kim, J. Park, Y. T. Seo, H. Zeng, I. L. Moudrakovskr, C. I. Ratcliffe, and J. A. Ripmeester. Tuning Clathrate Hydrates for Hydrogen Storage. *Nature*, vol. 434, no. 7034, 2005, pp. 743–746.

67. H. P. Veluswamy, R. Kumar, and P. Linga. Hydrogen Storage in Clathrate Hydrates: Current State of the Art and Future Directions. *Applied Energy*, vol. 122, 2014, pp. 112–132.

68. K. T. Møller, T. R. Jensen, E. Akiba, and H. wen Li. Hydrogen - A Sustainable Energy Carrier. *Progress in Natural Science: Materials International*, vol. 27, no. 1, 2017, pp. 34–40.

69. I. P. Jain, C. Lal, and A. Jain. Hydrogen Storage in Mg: A Most Promising Material. *International Journal of Hydrogen Energy*, vol. 35, no. 10, 2010, pp. 5133–5144.

70. B. Sakintuna, F. Lamari-Darkrim, and M. Hirscher. Metal Hydride Materials for Solid Hydrogen Storage: A Review. *International Journal of Hydrogen Energy*, vol. 32, no. 9, 2007, pp. 1121–1140.

71. H. Falahati, and D. P. J. Barz. Evaluation of Hydrogen Sorption Models for AB_5-Type Metal Alloys by Employing a Gravimetric Technique. *International Journal of Hydrogen Energy*, vol. 38, no. 21, 2013, pp. 8838–8851.

72. M. Dornheim. Tailoring Reaction Enthalpies of Hydrides. *Handbook of Hydrogen Storage: New Materials for Future Energy Storage*, 2010, pp. 184–214.

73. M. C. Georgiadis, E. S. Kikkinides, S. S. Makridis, K. Kouramas, and E. N. Pistikopoulos. Design and Optimization of Advanced Materials and Processes for Efficient Hydrogen Storage. *Computers and Chemical Engineering*, vol. 33, no. 5, 2009, pp. 1077–1090.

74. E. M. Borzone, A. Baruj, M. V. Blanco, and G. O. Meyer. Dynamic Measurements of Hydrogen Reaction with $LaNi_{5-x}Sn_x$ Alloys. *International Journal of Hydrogen Energy*, vol. 38, no. 18, 2013, pp. 7335–7343.

75. G. Principi, F. Agresti, A. Maddalena, and S. Lo Russo. The Problem of Solid

State Hydrogen Storage. *Energy*, vol. 34, no. 12, 2009, pp. 2087–2091.

76. K. D. Ćirić, A. Kocjan, A. Gradišek, V. J. Koteski, A. M. Kalijadis, V. N. Ivanovski, Z. V. Laušević, and D. L. Stojić. A Study on Crystal Structure, Bonding and Hydriding Properties of Ti-Fe-Ni Intermetallics - Behind Substitution of Iron by Nickel. *International Journal of Hydrogen Energy*, vol. 37, no. 10, 2012, pp. 8408–8417.

77. K. Young, D. F. Wong, S. Yasuoka, J. Ishida, J. Nei, and J. Koch. Different Failure Modes for V-Containing and V-Free AB_2 Metal Hydride Alloys. *Journal of Power Sources*, vol. 251, 2014, pp. 170–177.

78. R. V. Denys, B. Riabov, V. A. Yartys, R. G. Delaplane, and M. Sato. Hydrogen Storage Properties and Structure of $La_{1-x}Mg_x(Ni_{1-y}Mn_y)_3$ Intermetallics and Their Hydrides. *Journal of Alloys and Compounds*, vols. 446–447, 2007, pp. 166–172.

79. M. Anik, B. Baksan, T. Ö. Orbay, N. Küçükdeveci, A. B. Aybar, R. C. Özden, H. Gaşan, and N. Koç. Hydrogen Storage Characteristics of Ti_2Ni Alloy Synthesized by the Electro-Deoxidation Technique. *Intermetallics*, vol. 46, 2014, pp. 51–55.

80. X. Zhao, J. Zhou, X. Shen, M. Yang, and L. Ma. Structure and Electrochemical Hydrogen Storage Properties of A 2B-Type Ti-Zr-Ni Alloys. *International Journal of Hydrogen Energy*, vol. 37, no. 6, 2012, pp. 5050–5055.

81. J. Breternitz, and D. H. Gregory. The Search for Hydrogen Stores on a Large Scale; a Straightforward and Automated Open Database Analysis as a First Sweep for Candidate Materials. *Crystals*, vol. 5, no. 4, 2015, pp. 617–633.

82. N. Settouti, and H. Aourag. Structural and Mechanical Properties of Alkali Hydrides Investigated by the First-Principles Calculations and Principal Component Analysis. *Solid State Sciences*, vol. 58, 2016, pp. 30–36.

83. R. A. S. Charles E. Messer , Edwin B. Damon , P. Calvin Maybury , John Mellor, C. E. Messer, E. B. Damon, P. C. Maybury, J. Mellor, and R. A. Seales. Solid–Liquid Equilibrium in the Lithium Lithium Hydride System. *The Journal of Physical Chemistry*, vol. 62, no. 2, 1958, pp. 220–222.

84. Y. Jia, C. Sun, S. Shen, J. Zou, S. S. Mao, and X. Yao. Combination of Nanosizing and Interfacial Effect: Future Perspective for Designing Mg-Based Nanomaterials for Hydrogen Storage. *Renewable and Sustainable Energy*

Reviews, vol. 44, 2015, pp. 289–303.

85. R. Bardhan, A. M. Ruminski, A. Brand, and J. J. Urban. Magnesium Nanocrystal-Polymer Composites: A New Platform for Designer Hydrogen Storage Materials. *Energy & Environmental Science*, vol. 4, no. 12, 2011, p. 4882.

86. A. Zaluska, L. Zaluski, and J. O. Ström-Olsen. Nanocrystalline Magnesium for Hydrogen Storage. *Journal of Alloys and Compounds*, vol. 288, nos. 1–2, 1999, pp. 217–225.

87. M. Paskevicius, D. a. Sheppard, and C. E. Buckley. Thermodynamic Changes in Mechanochemically Synthesized Magnesium Hydride Nanoparticles. *Journal of the American Chemical Society*, vol. 132, no. 14, 2010, pp. 5077–5083.

88. C. Milanese, A. Girella, S. Garroni, G. Bruni, V. Berbenni, P. Matteazzi, and A. Marini. Synergetic Effect of C (Graphite) and Nb_2O_5 on the H_2 Sorption Properties of the Mg-MgH_2 System. *International Journal of Hydrogen Energy*, vol. 35, no. 17, 2010, pp. 9027–9037.

89. M. Cabo, S. Garroni, E. Pellicer, C. Milanese, A. Girella, A. Marini, E. Rossinyol, S. Suriñach, and M. D. Baró. Hydrogen Sorption Performance of MgH2 Doped with Mesoporous Nickel- and Cobalt-Based Oxides. *International Journal of Hydrogen Energy*, vol. 36, no. 9, 2011, pp. 5400–5410.

90. M. Dornheim, S. Doppiu, G. Barkhordarian, U. Boesenberg, T. Klassen, O. Gutfleisch, and R. Bormann. Hydrogen Storage in Magnesium-Based Hydrides and Hydride Composites. *Scripta Materialia*, vol. 56, no. 10, 2007, pp. 841–846.

91. S. Orimo, Y. Nakamori, J. R. Eliseo, A. Züttel, and C. M. Jensen. Complex Hydrides for Hydrogen Storage. *Chemical Reviews*, vol. 107, no. 10, 2007, pp. 4111–4132.

92. B. Bogdanović, and M. Schwickardi. Ti-Doped Alkali Metal Aluminium Hydrides as Potential Novel Reversible Hydrogen Storage Materials. *Journal of Alloys and Compounds*, vols. 253–254, 1997, pp. 1–9.

93. J. Graetz, J. J. Reilly, V. A. Yartys, J. P. Maehlen, B. M. Bulychev, V. E. Antonov, B. P. Tarasov, and I. E. Gabis. Aluminum Hydride as a Hydrogen and Energy Storage Material: Past, Present and Future. *Journal of Alloys and Compounds*, vol. 509, no. SUPPL. 2, 2011, pp. S517–S528.

94. A. E. Finholt, A. C. Bond, and H. I. Schlesinger. Lithium Aluminum Hydride, Aluminum Hydride and Lithium Gallium Hydride, and Some of Their Applications in Organic and Inorganic Chemistry 1. *Journal of the American Chemical Society*, vol. 69, no. 5, 1947, pp. 1199–1203.

95. Y. Wang, G. K. Pálsson, H. Raanaei, and B. Hjörvarsson. The Influence of Amorphous Al_2O_3 Coating on Hydrogen Uptake of Materials. *Journal of Alloys and Compounds*, vol. 464, nos. 1–2, 2008, pp. 13–16.

96. G. Sandrock, J. Reilly, J. Graetz, W. M. Zhou, J. Johnson, and J. Wegrzyn. Alkali Metal Hydride Doping of α-AlH3 for Enhanced H2 Desorption Kinetics. *Journal of Alloys and Compounds*, vol. 421, nos. 1–2, 2006, pp. 185–189.

97. I. E. Gabis, A. P. Baraban, V. G. Kuznetsov, D. I. Elets, M. A. Dobrotvorskii, and A. P. Voyt. A Mechanism of Ultraviolet Activation of the α-AlH_3 Decomposition. *International Journal of Hydrogen Energy*, vol. 39, no. 28, 2014, pp. 15844–15850.

98. M. Fichtner, and O. Fuhr. Synthesis and Structures of Magnesium Alanate and Two Solvent Adducts. *Journal of Alloys and Compounds*, vol. 345, nos. 1–2, 2002, pp. 286–296.

99. J. Huot, S. Boily, V. Güther, and R. Schulz. Synthesis of Na3AlH6 and Na_2LiAlH_6 by Mechanical Alloying. *Journal of Alloys and Compounds*, vol. 283, nos. 1–2, 1999, pp. 304–306.

100. H. Morioka, K. Kakizaki, S. C. Chung, and A. Yamada. Reversible Hydrogen Decomposition of KAlH4. *Journal of Alloys and Compounds*, vol. 353, nos. 1–2, 2003, pp. 310–314.

101. H. W. Li, S. Orimo, Y. Nakamori, K. Miwa, N. Ohba, S. Towata, and A. Züttel. Materials Designing of Metal Borohydrides: Viewpoints from Thermodynamical Stabilities. *Journal of Alloys and Compounds*, vols. 446–447, no. January 2017, 2007, pp. 315–318.

102. I. P. Jain, P. Jain, and A. Jain. Novel Hydrogen Storage Materials: A Review of Lightweight Complex Hydrides. *Journal of Alloys and Compounds*, vol. 503, no. 2, 2010, pp. 303–339.

103. S. G. Shore, and R. W. Parry. The Crystalline Compound Ammonia-Borane,

H_3NBH_3. *Journal of the American Chemical Society*, vol. 77, no. 22, 1955, pp. 6084–6085.

104. A. Staubitz, A. P. M. Robertson, and I. Manners. Ammonia-Borane and Related Compounds as Dihydrogen Sources. *Chemical Reviews*, vol. 110, no. 7, 2010, pp. 4079–4124.

105. C. F. Hoon, and E. C. Reynhardt. Molecular Dynamics and Structures of Amine Boranes of the Type R_3N- BH_3: I. X-Ray Investigation of H_3N-BH_3 at 295 K and 110 K. *Journal of Physics C: Solid State Physics*, vol. 16, 1983, pp. 6129–6136.

106. M. Chandra, and Q. Xu. A High-Performance Hydrogen Generation System: Transition Metal-Catalyzed Dissociation and Hydrolysis of Ammonia-Borane. *Journal of Power Sources*, vol. 156, no. 2, 2006, pp. 190–194.

107. S. Frueh, R. Kellett, C. Mallery, T. Molter, W. S. Willis, C. King'Ondu, and S. L. Suib. Pyrolytic Decomposition of Ammonia Borane to Boron Nitride. *Inorganic Chemistry*, vol. 50, no. 3, 2011, pp. 783–792.

108. S. Orimo, Y. Nakamori, G. Kitahara, K. Miwa, N. Ohba, S. Towata, and A. Züttel. Dehydriding and Rehydriding Reactions of $LiBH_4$. *Journal of Alloys and Compounds*, vols. 404–406, no. SPEC. ISS., 2005, pp. 427–430.

109. R. Levine, and W. Conard Fernelius. The Chemistry of the Alkali Amides. III. *Chemical Reviews*, vol. 54, no. 3, 1954, pp. 449–573.

110. A. W. Titherlet, and G. Lussac. XLV.- Sodium, Potassium and Lithium Amides. *Journal of the Chemical Society, Transactions*, vol. 65, 1894, pp. 504–522.

111. H. Y. Leng, T. Ichikawa, S. Hino, and N. Hanada. New Metal - N - H System Composed of $Mg(NH_2)_2$ and LiH for Hydrogen Storage. *J. Phys. Chem. B*, vol. 108, no. 26, 2004, pp. 8763–8765.

112. Y. Nakamori, G. Kitahara, and S. Orimo. Synthesis and Dehydriding Studies of Mg-N-H Systems. *Journal of Power Sources*, vol. 138, nos. 1–2, 2004, pp. 309–312.

113. P. Chen, Z. Xiong, J. Luo, J. Lin, and K. L. Tan. Interaction of Hydrogen with Metal Nitrides and Imides. *Nature*, vol. 420, no. 6913, 2002, pp. 302–304.

114. S. Isobe, T. Ichikawa, K. Tokoyoda, N. Hanada, H. Leng, H. Fujii, and Y. Kojima. Evaluation of Enthalpy Change Due to Hydrogen Desorption for Lithium

Amide/Imide System by Differential Scanning Calorimetry. *Thermochimica Acta*, vol. 468, nos. 1–2, 2008, pp. 35–38.

115. J. B. Yang, X. D. Zhou, Q. Cai, W. J. James, and W. B. Yelon. Crystal and Electronic Structures of LiNH2. *Applied Physics Letters*, vol. 88, no. 4, 2006, pp. 1–3.

116. D. H. Gregory. Lithium Nitrides, Imides and Amides as Lightweight, Reversible Hydrogen Stores. *Journal of Materials Chemistry*, no. 20, 2008, pp. 2321–2330.

117. F. E. Pinkerton. Decomposition Kinetics of Lithium Amide for Hydrogen Storage Materials. *Journal of Alloys and Compounds*, vol. 400, nos. 1–2, 2005, pp. 76–82.

118. F. E. Pinkerton. Decomposition Kinetics of Lithium Amide and Its Implications for Hydrogen Storage. *Materials Research*, vol. 837, no. 2, 2005, pp. 1–6.

119. M. P. Balogh, C. Y. Jones, J. F. Herbst, L. G. Hector, and M. Kundrat. Crystal Structures and Phase Transformation of Deuterated Lithium Imide, Li_2ND. *Journal of Alloys and Compounds*, vol. 420, nos. 1–2, 2006, pp. 326–336.

120. F. Dolci, E. Napolitano, E. Weidner, S. Enzo, P. Moretto, M. Brunelli, T. Hansen, M. Fichtner, and W. Lohstroh. Magnesium Imide: Synthesis and Structure Determination of an Unconventional Alkaline Earth Imide from Decomposition of Magnesium Amide. *Inorganic Chemistry*, vol. 50, no. 3, 2011, pp. 1116–1122.

121. H. Jacobs, and R. Juza. Darstellung Und Eigenschaften von Magnesiumamid Und -Imid. *Journal of Inorganic and General Chemistry*, vol. 370, nos. 5–6, 1969, pp. 254–261.

122. T. A. T. Seip, R. A. Olsen, and O. M. Løvvik. Surfaces and Clusters of Mg(NH2)2 Studied by Density Functional Theory Calculations. *J. Phys. Chem. C*, vol. 113, 2009, pp. 21648–21656.

123. F. E. Pinkerton. Decomposition Kinetics of Lithium Amide for Hydrogen Storage Materials. *Journal of Alloys and Compounds*, vol. 400, nos. 1–2, 2005, pp. 76–82.

124. Y. Nakamori, and S. I. Orimo. Destabilization of Li-Based Complex Hydrides. *Journal of Alloys and Compounds*, vol. 370, nos. 1–2, 2004, pp. 271–275.

125. Z. Xiong, G. Wu, J. Hu, and P. Chen. Ternary Imides for Hydrogen Storage. *Advanced Materials*, vol. 16, no. 17, 2004, pp. 1522–1525.

126. J. Hu, Y. Liu, G. Wu, Z. Xiong, and P. Chen. Structural and Compositional Changes during Hydrogenation/Dehydrogenation of the Li-Mg-N-H System. *Journal of Physical Chemistry C*, vol. 111, no. 49, 2007, pp. 18439–18443.

127. F. Dolci, E. Weidner, M. Hoelzel, T. Hansen, P. Moretto, C. Pistidda, M. Brunelli, M. Fichtner, and W. Lohstroh. In-Situ Neutron Diffraction Study of Magnesium Amide / Lithium Hydride Stoichiometric Mixtures with Lithium Hydride Excess. *International Journal of Hydrogen Energy*, vol. 35, no. 11, 2010, pp. 5448–5453.

128. E. Weidner, E. Weidner, F. Dolci, F. Dolci, J. Hu, J. Hu, W. Lohstroh, W. Lohstroh, T. Hansen, T. Hansen, D. J. Bull, D. J. Bull, M. Fichtner, and M. Fichtner. Hydrogenation Reaction Pathway in $Li_2Mg(NH)_2$. *The Journal of Physical Chemistry C*, vol. 113, no. 35, 2009, pp. 15772–15777.

129. Y. Liu, C. Liang, Z. Wei, Y. Jiang, M. Gao, H. Pan, and Q. Wang. Hydrogen Storage Reaction over a Ternary Imide $Li_2Mg_2N_3H_3$. *Physical chemistry chemical physics : PCCP*, vol. 12, no. 13, 2010, pp. 3108–11.

130. H. I. Schlesinger, R. T. Sanderson, and A. B. Burg. A Volatile Compound of Aluminum, Boron and Hydrogen. *Journal of the American Chemical Society*, vol. 61, no. 2, 1939, p. 536.

131. H. I. Schlesinger, and H. C. Brown. Metallo Borohydrides. III. Lithium Borohydride. *Journal of the American Chemical Society*, vol. 62, no. 12, 1940, pp. 3429–3435.

132. H. I. Schlesinger, C. Brown, B. Abraham, A. . Bond, N. Davidson, A. E. Finholt, J. R. Gilbreath, H. Hoekstra, L. Horvitz, E. K. Hyde, J. J. Katz, J. Knight, R. A. Lad, D. L. Mayfield, L. Rapp, D. M. Ritter, A. M. Schwartz, I. Sheft, L. D. Tuck, and A. O. Walker. New Developments in the Chemistry of Diborane and the Borohydrides. I. General Summary. vol. 219, 1953, pp. 186–190.

133. B. Richter, D. B. Ravnsbæk, N. Tumanov, Y. Filinchuk, and T. R. Jensen. Manganese Borohydride; Synthesis and Characterization. *Dalton Transactions*, vol. 44, no. 9, 2015, pp. 3988–3996.

134. P. Zanella, L. Crociani, N. Masciocchi, and G. Giunchi. Facile High-Yield Synthesis of Pure, Crystalline $Mg(BH_4)_2$. *Inorganic Chemistry*, vol. 46, no. 22, 2007, pp. 9039–9041.

135. R. Černý, Y. Filinchuk, H. Hagemann, and K. Yvon. Magnesium Borohydride:

Synthesis and Crystal Structure. *Angewandte Chemie - International Edition*, vol. 46, no. 30, 2007, pp. 5765–5767.

136. J. Huot, D. B. Ravnsbæk, J. Zhang, F. Cuevas, M. Latroche, and T. R. Jensen. Mechanochemical Synthesis of Hydrogen Storage Materials. *Progress in Materials Science*, vol. 58, no. 1, 2013, pp. 30–75.

137. D. Ravnsbœk, Y. Filinchuk, Y. Cerenius, H. J. Jakobsen, F. Besenbacher, J. Skibsted, and T. R. Jensen. A Series of Mixed-Metal Borohydrides. *Angewandte Chemie - International Edition*, vol. 48, no. 36, 2009, pp. 6659–6663.

138. M. Paskevicius, L. H. Jepsen, P. Schouwink, R. Černý, D. B. Ravnsbæk, Y. Filinchuk, M. Dornheim, F. Besenbacher, and T. R. Jensen. Metal Borohydrides and Derivatives-Synthesis, Structure and Properties. *Chemical Society Reviews*, vol. 46, no. 5, 2017, pp. 1565–1634.

139. Y. Nakamori, K. Miwa, A. Ninomiya, H. Li, N. Ohba, S. I. Towata, A. Züttel, and S. I. Orimo. Correlation between Thermodynamical Stabilities of Metal Borohydrides and Cation Electronegativites: First-Principles Calculations and Experiments. *Physical Review B - Condensed Matter and Materials Physics*, vol. 74, no. 4, 2006, pp. 1–9.

140. D. Harrison, and T. Thonhauser. Suppressing Diborane Production during the Hydrogen Release of Metal Borohydrides: The Example of Alloyed $Al(BH_4)_3$. *International Journal of Hydrogen Energy*, vol. 41, no. 5, 2016, pp. 3571–3578.

141. A. Zuttel, S. Rentsch, P. Fischer, P. Wenger, P. Sudan, P. Mauron, and C. Emmenegger. Hydrogen Storage Properties of LiBH4. *Journal of Alloys and Compounds*, vols. 356–357, 2003, pp. 515–520.

142. O. Friedrichs, A. Borgschulte, S. Kato, F. Buchter, R. Gremaud, A. Remhof, and A. Züttel. Low-Temperature Synthesis of $LiBH_4$ by Gas-Solid Reaction. *Chemistry - A European Journal*, vol. 15, no. 22, 2009, pp. 5531–5534.

143. H. C. Brown, Y. M. Choi, and S. Narasimhan. Inorg. Chem. 1981, 20, 2350-2352. *Inorg. Chem.*, vol. 20, no. 12, 1981, pp. 4454–4456.

144. J. Soulie, G. Renaudin, R. Černý, and K. Yvon. Lithium Boro-Hydride $LiBH_4$ I. Crystal Structure. *Journal of Alloys and Compounds*, vol. 346, 2002, pp. 200–205.

145. M. R. Hartman, J. J. Rush, T. J. Udovic, R. C. Bowman, and S. J. Hwang.

Structure and Vibrational Dynamics of Isotopically Labeled Lithium Borohydride Using Neutron Diffraction and Spectroscopy. *Journal of Solid State Chemistry*, vol. 180, no. 4, 2007, pp. 1298–1305.

146. Y. Filinchuk, D. Chernyshov, A. Nevidomskyy, and V. Dmitriev. High-Pressure Polymorphism as a Step towards Destabilization of $LiBH_4$. *Angewandte Chemie - International Edition*, vol. 47, no. 3, 2008, pp. 529–532.

147. M. Paskevicius, M. B. Ley, D. A. Sheppard, T. R. Jensen, and C. E. Buckley. Eutectic Melting in Metal Borohydrides. *Physical Chemistry Chemical Physics*, vol. 15, no. 45, 2013, pp. 19774–19789.

148. A. Zuttel, P. Wenger, S. Rentsch, P. Sudan, P. Mauron, and C. Emmenegger. $LiBH_4$ a New Hydrogen Storage Material. *Journal of Power Sources*, vol. 118, nos. 1–2, 2003, pp. 1–7.

149. C. Li, P. Peng, D. W. Zhou, and L. Wan. Research Progress in $LiBH_4$ for Hydrogen Storage: A Review. *International Journal of Hydrogen Energy*, vol. 36, no. 22, 2011, pp. 14512–14526.

150. A. Jain, H. Miyaoka, and T. Ichikawa. Destabilization of Lithium Hydride by the Substitution of Group 14 Elements: A Review. *International Journal of Hydrogen Energy*, vol. 41, no. 14, 2016, pp. 5969–5978.

151. D. M. F. Santos, and C. A. C. Sequeira. Sodium Borohydride as a Fuel for the Future. *Renewable and Sustainable Energy Reviews*, vol. 15, no. 8, 2011, pp. 3980–4001.

152. P. Martelli, R. Caputo, A. Remhof, P. Mauron, A. Borgschulte, and A. Züttel. Stability and Decomposition of $NaBH_4$. *The Journal of Physical Chemistry C*, vol. 114, no. 15, 2010, pp. 7173–7177.

153. W. Büchner, H. Niederprüm, B. Ag, W. Germany, A.- Sodiumborohydride, and I. Nabh. Sodium Borohydride and Amine-Boranes, Commercially Important Reducing Agents. *Pure & Appl. Chem.*, vol. 49, 1977, pp. 733–743.

154. Y. Kojima, and T. Haga. Recycling Process of Sodium Metaborate to Sodium Borohydride. *International Journal of Hydrogen Energy*, vol. 28, no. 9, 2003, pp. 989–993.

155. M. T. Kelly, and J. V Ortega. Review of Chemical Processes for the Synthesis of

Sodium Borohydride. *Millennium cell Inc.*, no. August, 2004, p. DOE.

156. S. Suda, N. Morigasaki, Y. Iwase, and Z. P. Li. Production of Sodium Borohydride by Using Dynamic Behaviors of Protide at the Extreme Surface of Magnesium Particles. *Journal of Alloys and Compounds*, vols. 404–406, no. SPEC. ISS., 2005, pp. 643–647.

157. Ç. Çakanyildirim, and M. Gürü. Processing of $NaBH_4$ from NaBO2 with MgH2 by Ball Milling and Usage as Hydrogen Carrier. *Renewable Energy*, vol. 35, no. 9, 2010, pp. 1895–1899.

158. R. L. Davis, and C. H. L. Kennard. Structure of Sodium Tetradeuteroborate, $NaBD_4$. *Journal of Solid State Chemistry*, vol. 59, no. 3, 1985, pp. 393–396.

159. R. S. Kumar, and A. L. Cornelius. Structural Transitions in $NaBH_4$ under Pressure. *Applied Physics Letters*, vol. 87, no. 26, 2005, pp. 1–3.

160. P. Fischer, and A. Züttel. Order-Disorder Phase Transition in $NaBD_4$. *Materials Science Forum*, vols. 443–444, 2004, pp. 287–290.

161. H. I. Schlesinger, H. C. Brown, A. E. Finholt, J. R. Gilbreath, H. R. Hoekstra, and E. K. Hyde. Sodium Borohydride, Its Hydrolysis and Its Use as a Reducing Agent and in the Generation of Hydrogen. *Journal of the American Chemical Society*, vol. 75, no. 1, 1953, pp. 215–219.

162. M. Paskevicius, M. B. Ley, D. A. Sheppard, R. Jensen, and C. E. Buckley. Eutectic Melting in Metal Borohydrides. *Physical Chemistry Chemical Physics*, vol. 15, no. 43, 2013, pp. 19774–19789.

163. H. I. Schlesinger, H. C. Brown, H. R. Hoekstra, and L. R. Rapp. Reactions of Diborane with Alkali Metal Hydrides and Their Addition Compounds. New Syntheses of Borohydrides. Sodium and Potassium Borohydrides. *Journal of the American Chemical Society*, vol. 75, no. 1, 1953, pp. 199–204.

164. Z. P. Li, B. H. Liu, N. Morigasaki, and S. Suda. Preparation of Potassium Borohydride by a Mechano-Chemical Reaction of Saline Hydrides with Dehydrated Borate through Ball Milling. *Journal of Alloys and Compounds*, vol. 354, nos. 1–2, 2003, pp. 243–247.

165. M. D. Banus, and D. P. Ingalls. Potassium Borohydride Manufacture. *Industrial and Engineering Chemistry*, vol. 49, no. 10, 1957, pp. 166–1672.

166. K. C. Kim, and D. S. Sholl. Crystal Structures and Thermodynamic Investigations of $LiK(BH_4)_2$, KBH_4, and $NaBH_4$ from First-Principles Calculations. *J. Phys. Chem. C*, vol. 114, 2010, pp. 678–686.

167. P. Vajeeston, P. Ravindran, A. Kjekshus, and H. Fjellvåg. Structural Stability of Alkali Boron Tetrahydrides ABH_4(A = Li, Na, K, Rb, Cs) from First Principle Calculation. *Journal of Alloys and Compounds*, vol. 387, nos. 1–2, 2005, pp. 97–104.

168. R. S. Kumar, E. Kim, and A. L. Cornelius. Structural Phase Transitions in the Potential Hydrogen Storage Compound KBH 4 under Compression. *The Journal of Physical Chemistry C*, vol. 112, no. 22, 2008, pp. 8452–8457.

169. Ö. Şahin, H. Dolaş, and M. Özdemir. The Effect of Various Factors on the Hydrogen Generation by Hydrolysis Reaction of Potassium Borohydride. *International Journal of Hydrogen Energy*, vol. 32, no. 13, 2007, pp. 2330–2336.

170. M. Au, A. R. Jurgensen, W. A. Spencer, D. L. Anton, F. E. Pinkerton, S. J. Hwang, C. Kim, and R. C. Bowman. Stability and Reversibility of Lithium Borohydrides Doped by Metal Halides and Hydrides. *Journal of Physical Chemistry C*, vol. 112, no. 47, 2008, pp. 18661–18671.

171. S. Garroni, C. Pistidda, M. Brunelli, G. B. M. Vaughan, S. Suriñach, and M. D. Baró. Hydrogen Desorption Mechanism of $2NaBH_4 + MgH_2$ Composite Prepared by High-Energy Ball Milling. *Scripta Materialia*, vol. 60, no. 12, 2009, pp. 1129–1132.

172. C. Pistidda, G. Barkhordarian, A. Rzeszutek, S. Garroni, C. B. Minella, M. D. Baró, P. Nolis, R. Bormann, T. Klassen, and M. Dornheim. Activation of the Reactive Hydride Composite $2NaBH_4$+ MgH_2. *Scripta Materialia*, vol. 64, no. 11, 2011, pp. 1035–1038.

173. C. Milanese, S. Garroni, A. Girella, G. Mulas, V. Berbenni, G. Bruni, S. Suriñach, M. D. Baró, and A. Marini. Thermodynamic and Kinetic Investigations on Pure and Doped $NaBH_4$-MgH_2 System. *Journal of Physical Chemistry C*, vol. 115, no. 7, 2011, pp. 3151–3162.

174. C. B. Minella, C. Pistidda, S. Garroni, P. Nolis, M. D. Baró, O. Gutfleisch, T. Klassen, R. Bormann, and M. Dornheim. $Ca(BH_4)_2 + MgH_2$: Desorption Reaction and Role of Mg on Its Reversibility. *Journal of Physical Chemistry C*, vol. 117, no.

8, 2013, pp. 3846–3852.

175. R. M. Adams. Preparation of Diborane. *Adv. Chem.*, vol. 32, 1961, pp. 60–68.

176. E. M. Dematteis, E. Roedern, E. R. Pinatel, M. Corno, T. R. Jensen, and M. Baricco. A Thermodynamic Investigation of the $LiBH_4$-$NaBH_4$ System. *RSC Adv.*, vol. 6, 2016, pp. 60101–60108.

177. A. Ampoumogli, T. Steriotis, P. Trikalitis, E. G. Bardaji, M. Fichtner, A. Stubos, and G. Charalambopoulou. Synthesis and Characterisation of a Mesoporous Carbon/Calcium Borohydride Nanocomposite for Hydrogen Storage. *International Journal of Hydrogen Energy*, vol. 37, no. 21, 2012, pp. 16631–16635.

178. A. Ampoumogli, G. Charalambopoulou, P. Javadian, B. Richter, T. R. Jensen, and T. Steriotis. Hydrogen Desorption and Cycling Properties of Composites Based on Mesoporous Carbons and a $LiBH_4$–$Ca(BH_4)_2$ Eutectic Mixture. *Journal of Alloys and Compounds*, vol. 645, no. 1, 2015, pp. S480–S484.

179. H.-S. Lee, S. Hwang, H. K. Kim, Y. Lee, J. Park, J. Yu, and Y. W. Cho. In Situ NMR Study on the Interaction between $LiBH_4$–$Ca(BH_4)_2$ and Mesoporous Scaffolds. *The Journal of Physical Chemistry Letters*, vol. 3, no. 20, 2012, pp. 2922–2927.

180. H. S. Lee, Y. S. Lee, J. Y. Suh, M. Kim, J. S. Yu, and Y. W. Cho. Enhanced Desorption and Absorption Properties of Eutectic $LiBH_4$-$Ca(BH_4)_2$ Infiltrated into Mesoporous Carbon. *Journal of Physical Chemistry C*, vol. 115, no. 40, 2011, pp. 20027–20035.

181. S. Sartori, K. D. Knudsen, F. S. Hage, R. H. Heyn, E. G. Bardaji, Z. Zhao-Karger, M. Fichtner, and B. C. Hauback. Influence of Nanoconfinement on Morphology and Dehydrogenation of the $Li^{11}BD_4$-$Mg(^{11}BD_4)_4$ System. *Nanotechnology*, vol. 23, no. 25, 2012.

182. P. Javadian, and T. R. Jensen. Enhanced Hydrogen Reversibility of Nanoconfined $LiBH_4$-$Mg(BH_4)_2$. *International Journal of Hydrogen Energy*, vol. 39, no. 18, 2014, pp. 9871–9876.

183. Z. Zhao-Karger, R. Witter, E. G. Bardají, D. Wang, D. Cossement, and M. Fichtner. Altered Reaction Pathways of Eutectic $LiBH_4$–$Mg(BH_4)_2$ by Nanoconfinement. *Journal of Materials Chemistry A*, vol. 1, no. 10, 2013, p. 3379.

184. S. Sartori, K. D. Knudsen, Z. Zhao-Karger, E. G. Bardaij, M. Fichtner, and B. C. Hauback. Small-Angle Scattering Investigations of Mg-Borohydride Infiltrated in Activated Carbon. *Nanotechnology*, vol. 20, no. 50, 2009, p. 505702.

185. P. Javadian, C. Zlotea, C. M. Ghimbeu, M. Latroche, and T. R. Jensen. Hydrogen Storage Properties of Nanoconfined $LiBH_4$ – Mg_2NiH_4 Reactive Hydride Composites. *The Journal of Physical Chemistry C*, vol. 119, no. 11, 2015, pp. 5819–5826.

186. S. Thiangviriya, P. Plerdsranoy, N. Wiset, P. Javadian, T. R. Jensen, and R. Utke. Hydrogen Sorption and Reaction Mechanisms of Nanoconfined $2LiBH_4$ - $NaAlH_4$. *Journal of Alloys and Compounds*, vol. 633, 2015, pp. 484–493.

187. P. Javadian, D. A. Sheppard, C. E. Buckley, and T. R. Jensen. Hydrogen Storage Properties of Nanoconfined $LiBH_4$ -$NaBH_4$. *International Journal of Hydrogen Energy*, vol. 40, no. 43, 2015, pp. 14916–14924.

188. M. B. Ley, E. Roedern, and T. R. Jensen. Eutectic Melting of $LiBH_4$-KBH_4. *Physical chemistry chemical physics : PCCP*, vol. 16, no. 44, 2014, pp. 24194–24199.

189. E. A. Nickels, M. O. Jones, W. I. F. David, S. R. Johnson, R. L. Lowton, M. Sommariva, and P. P. Edwards. ..Tuning the Decomposition Temperature in Complex Hydrides: Synthesis of a Mixed Alkali Metal Borohydride. *Angewandte Chemie - International Edition*, vol. 47, no. 15, 2008, pp. 2817–2819.

190. H. Hagemann, V. D'Anna, J. P. Rapin, R. Černý, Y. Filinchuk, K. C. Kim, D. S. Sholl, and S. F. Parker. New Fundamental Experimental Studies on α-$Mg(BH_4)_2$ and Other Borohydrides. *Journal of Alloys and Compounds*, vol. 509, no. SUPPL. 2, 2011, pp. 2010–2012.

191. E. G. Bardají, Z. Zhao-Karger, N. Boucharat, A. Nale, M. J. Van Setten, W. Lohstroh, E. Rahm, M. Catti, and M. Fichtner. $LiBH_4$-$Mg(BH_4)_2$: A Physical Mixture of Metal Borohydrides as Hydrogen Storage Material. *Journal of Physical Chemistry C*, vol. 115, no. 13, 2011, pp. 6095–6101.

192. E. Roedern, B. R. S. Hansen, M. B. Ley, and T. R. Jensen. Effect of Eutectic Melting, Reactive Hydride Composites, and Nanoconfinement on Decomposition and Reversibility of LiBH4-KBH4. *Journal of Physical Chemistry C*, vol. 119, no. 46, 2015, pp. 25818–25825.

193. H. Gleiter. Nanostructured Materials: Basic Concepts and Microstructure. *Acta Materialia*, vol. 48, no. 1, 2000, pp. 1–29.

194. L. Zaluski, A. Zaluska, and J. O. Ström-Olsen. Nanocrystalline Metal Hydrides. *Journal of Alloys and Compounds*, vols. 253–254, 1997, pp. 70–79.

195. V. Berube, G. Chen, and M. S. Dresselhaus. Impact of Nanostructuring on the Enthalpy of Formation of Metal Hydrides. *International Journal of Hydrogen Energy*, vol. 33, no. 15, 2008, pp. 4122–4131.

196. M. Fichtner. Properties of Nanoscale Metal Hydrides. *Nanotechnology*, vol. 20, no. 20, 2009, p. 204009.

197. D. L. Zhang. Processing of Advanced Materials Using High-Energy Mechanical Milling. *Progress in Materials Science*, vol. 49, nos. 3–4, 2004, pp. 537–560.

198. C. Suryanarayana. Mechanical Alloying and Milling. *Progress in Materials Science*, vol. 46, nos. 1–2, 2001, pp. 1–184.

199. C. C. Koch. Synthesis of Nanostructured Materials by Mechanical Milling: Problems and Opportunities. *Nanostructured materials*, vol. 9, nos. 1–8, 1997, pp. 13–22.

200. N. T. K. Thanh, N. Maclean, and S. Mahiddine. Mechanisms of Nucleation and Growth of Nanoparticles in Solution. *Chemical Reviews*, vol. 114, no. 15, 2014, pp. 7610–7630.

201. M. Fichtner. Nanoconfinement Effects in Energy Storage Materials. *Physical Chemistry Chemical Physics*, vol. 13, no. 48, 2011, p. 21186.

202. C. Zlotea, and M. Latroche. Role of Nanoconfinement on Hydrogen Sorption Properties of Metal Nanoparticles Hybrids. *Colloids and Surfaces A: Physicochemical and Engineering Aspects*, vol. 439, 2013, pp. 117–130.

203. T. K. Nielsen, F. Besenbacher, and T. R. Jensen. Nanoconfined Hydrides for Energy Storage. *Nanoscale*, vol. 3, no. 5, 2011, pp. 2086–2098.

204. M. H. Sun, S. Z. Huang, L. H. Chen, Y. Li, X. Y. Yang, Z. Y. Yuan, and B. L. Su. Applications of Hierarchically Structured Porous Materials from Energy Storage and Conversion, Catalysis, Photocatalysis, Adsorption, Separation, and Sensing to Biomedicine. *Chemical Society Reviews*, vol. 45, no. 12, 2016, pp. 3479–3563.

205. E. Koohsaryan, and M. Anbia. Nanosized and Hierarchical Zeolites: A Short Review. *Cuihua Xuebao/Chinese Journal of Catalysis*, vol. 37, no. 4, 2016, pp. 447–467.

206. J. Rouquerolt, D. Avnir, C. W. Fairbridge, D. H. Everett, J. H. Haynes, N. Pernicone, J. D. F. Ramsay, K. S. W. Sing, and K. K. Unger. Recommendations for the Characterization of Porous Solids. *Pure & Appl. Chem.*, vol. 66, no. 8, 1994, pp. 1739–1758.

207. P. Liu, and G.-F. Chen. *Porous Materials Processing and Applications*. 2014.

208. B. D. Zdravkov, J. J. Čermák, M. Šefara, and J. Janků. Pore Classification in the Characterization of Porous Materials: A Perspective. *Central European Journal of Chemistry*, vol. 5, no. 2, 2007, pp. 385–395.

209. D. J. Collins, and H.-C. Zhou. Nano/Microporous Materials: Hydrogen-Storage Materials. *Encyclopedia of Inorganic Chemistry*, 2009, pp. 1–7.

210. S. R. Tennison. Phenolic-Resin-Derived Activated Carbons. *Applied Catalysis A: General*, vol. 173, no. 2, 1998, pp. 289–311.

211. A. Pacula, and R. Mokaya. Synthesis and High Hydrogen Storage Capacity of Zeolite-Like Carbons Nanocast Using As-Synthesized Zeolite Templates. *J. Phys. Chem. C*, vol. 112, no. 7, 2008, pp. 2764–2769.

212. H. Kabbour, T. Baumann, J. Satcher, a Saulnier, and C. Ahn. Toward New Candidates for Hydrogen Storage: High Surface Area Carbon Aerogels. *Chem. Mater.*, vol. 18, no. 26, 2006, pp. 6085–7.

213. H. Wang, Q. Gao, and J. Hu. High Hydrogen Storage Capacity of Porous Carbons Prepared by Using Activated Carbon. *Journal of the American Chemical Society*, vol. 131, no. 20, 2009, pp. 7016–7022.

214. C. Liu, Y. Y. Fan, M. Liu, H. T. Cong, H. M. Cheng, and M. S. Dresselhaus. 01-Hydrogen Storage in Single-Walled Carbon Nanotubes at Room Temperature. *Science*, vol. 286, no. November, 1999, p. 1127.

215. E. T. Thostenson, Z. Ren, and T.-W. Chou. Advances in the Science and Technology of Carbon Nanotubes and Their Composites: A Review. *Composites Science and Technology*, vol. 61, no. 13, 2001, pp. 1899–1912.

216. G. Gulino, R. Vieira, J. Amadou, P. Nguyen, M. J. Ledoux, S. Galvagno, G. Centi,

and C. Pham-Huu. C2H6as an Active Carbon Source for a Large Scale Synthesis of Carbon Nanotubes by Chemical Vapour Deposition. *Applied Catalysis A: General*, vol. 279, nos. 1–2, 2005, pp. 89–97.

217. M. G. Nijkamp, J. E. M. J. Raaymakers, A. J. van Dillen, and K. P. de Jong. Hydrogen Storage Using Physisorption – Materials Demands. *Applied Physics A Materials Science & Processing*, vol. 72, no. 5, 2001, pp. 619–623.

218. D. J. Collins, and H. C. Zhou. Hydrogen Storage in Metal-Organic Frameworks. *Journal of Materials Chemistry*, vol. 17, no. 30, 2007, pp. 3154–3160.

219. M. Hirscher, and B. Panella. Hydrogen Storage in Metal-Organic Frameworks. *Scripta Materialia*, vol. 56, no. 10, 2007, pp. 809–812.

220. A. G. Wong-Foy, A. J. Matzger, and O. M. Yaghi. Exceptional H2 Saturation Uptake in Microporous Metal-Organic Frameworks. *Journal of the American Chemical Society*, vol. 128, no. 11, 2006, pp. 3494–3495.

221. L. Reguera, J. Balmaseda, L. F. Del Castillo, and E. Reguera. Hydrogen Storage in Porous Cyanometalates: Role of the Exchangeable Alkali Metal. *Journal of Physical Chemistry C*, vol. 112, no. 14, 2008, pp. 5589–5597.

222. G. M. Tom, W. Morris, M. H. Weston, P. E. Fuller, P. W. Siu, C. R. Murdock, J. P. Siegfried, and O. K. Farha. Utilization of Metal-Organic Frameworks for the Management of Gases Used in Ion Implantation. *2016 21st International Conference on Ion Implantation Technology (IIT)*, 2016, pp. 1–4.

223. A. Soleimani Dorcheh, and M. H. Abbasi. Silica Aerogel; Synthesis, Properties and Characterization. *Journal of Materials Processing Technology*, vol. 199, no. 1, 2008, pp. 10–26.

224. P. Kortesuo, M. Ahola, S. Karlsson, I. Kangasniemi, A. Yli-Urpo, and J. Kiesvaara. Silica Xerogel as an Implantable Carrier for Controlled Drug Delivery - Evaluation of Drug Distribution and Tissue Effects after Implantation. *Biomaterials*, vol. 21, no. 2, 2000, pp. 193–198.

225. S. D. W., K. D. Keefer, D. W. Schaefer, K. D. Keefer, S. D. W., and K. D. Keefer. Structure of Random Porous Materials: Silica Aerogel. *Physical Review Letters*, vol. 56, no. 20, 1986, pp. 2199–2202.

226. P. Wiltzius, F. S. Bates, S. B. Dierker, and G. D. Wignall. Structure of Porous

Vycor Glass. *Physical Review A*, vol. 36, no. 6, 1987, pp. 2991–2994.

227. J. S. Beck, J. C. Vartuli, W. J. Roth, M. E. Leonowicz, C. T. Kresge, K. D. Schmitt, C. T. W. Chu, D. H. Olson, E. W. Sheppard, S. B. McCullen, J. B. Higgins, and J. L. Schlenker. A New Family of Mesoporous Molecular Sieves Prepared with Liquid Crystal Templates. *Journal of the American Chemical Society*, vol. 114, no. 27, 1992, pp. 10834–10843.

228. D. W. Bruce, D. O'Hare, and R. I. Walton. *Porous Materials*. Wiley, 2010.

229. C. T. Kresge, M. E. Leonowicz, W. J. Roth, J. C. Vartuli, and J. S. Beck. Ordered Mesoporous Molecular Sieves Synthesized by a Liquid-Crystal Template Mechanism. *Nature*, vol. 359, 1992, pp. 710–712.

230. K. Schumacher, M. Grun, and K. K. Unger. Novel Synthesis of Spherical MCM-48. *Microporous and Mesoporous Materials*, vol. 27, nos. 2–3, 1999, pp. 201–206.

231. J. Y. Zhang, Z. Luz, and D. Goldfarb. EPR Studies of the Formation Mechanism of the Mesoporous Materials MCM-41 and MCM-50. *J. Phys. Chem. B*, vol. 101, no. 36, 1997, pp. 7087–7094.

232. A. J. Schwanke, R. Balzer, and S. Pergher. Microporous and Mesoporous Materials from Natural and Inexpensive Sources. In *Handbook of Ecomaterials*, 2017, pp. 3379–3399.

233. M. J. Kim, and R. Ryoo. Synthesis and Pore Size Control of Cubic Mesoporous Silica SBA-1. *Chemistry of Materials*, vol. 11, no. 2, 1999, pp. 487–491.

234. H. M. A. Hunter, A. E. Garcia-Bennett, I. J. Shannon, W. Zhou, and P. A. Wright. Particle Morphology and Microstructure in the Mesoporous Silicate SBA-2. *Journal of Materials Chemistry*, vol. 12, no. 1, 2002, pp. 20–23.

235. Q. Huo, R. Leon, P. M. Petroff, and G. D. Stucky. Mesostructure Design with Gemini Surfactants: Supercage Formation in a Three-Dimensional Hexagonal Array. *Science*, vol. 268, no. 5215, 1995, pp. 1324–1327.

236. M. Kruk, and M. Jaroniec. Characterization of the Porous Structure of SBA-15. no. 9, 2000, pp. 1961–1968.

237. T. W. Kim, R. Ryoo, M. Kruk, K. P. Gierszal, M. Jaroniec, S. Kamiya, and O. Terasaki. Tailoring the Pore Structure of SBA-16 Silica Molecular Sieve through the Use of Copolymer Blends and Control of Synthesis Temperature and Time.

Journal of Physical Chemistry B, vol. 108, no. 31, 2004, pp. 11480–11489.

238. S. A. Bagshaw, E. Prouzet, and T. J. Pinnavaia. Templating Mesoporous Molecular Sieves by Nonionic by Polyethylene Ocide Surfactants. *Science*, vol. 269, no. 5228, 1995, pp. 1242–1244.

239. F. S. H. C. and R. R. Kleitz. Cubic Ia3d Large Mesoporous Silica: Synthesis and Replication to Platinum Nanowires, Carbon Nanorods and Carbon Nanotubes. *Chemical communications*, no. 17, 2003, pp. 2136–2137.

240. S. D. Shen, Y. Q. Li, F. H. Wu, J. Fan, B. Tu, F. G. Tao, and D. Y. Zhao. Synthesis of a Novel Cubic Highly Ordered Mesoporous Silica Templated with Tri-Headgroup Quaternary Ammonium Surfactant. *Kao Teng Hsueh Hsiao Hua Heush Hsueh Pao/ Chemical Journal of Chinese Universities*, vol. 23, no. 3, 2002, pp. 2212–2213.

241. C. Yu, Y. Yu, and D. Zhao. Highly Ordered Large Caged Cubic Mesoporous Silica Structures Templated by Triblock PEO-PBO-PEO Copolymer. *Chemical Communications*, no. 7, 2000, pp. 575–576.

242. S. A. El-Safty. Review on the Key Controls of Designer Copolymer-Silica Mesophase Monoliths (HOM-Type) with Large Particle Morphology, Ordered Geometry and Uniform Pore Dimension. *Journal of Porous Materials*, vol. 15, no. 4, 2008, pp. 369–387.

243. S. A. El-Safty, and T. Hanaoka. Fabrication of Crystalline, Highly Ordered Three-Dimensional Silica Monoliths (HOM-n) with Large, Morphological Mesopore Structures. *Advanced Materials*, vol. 15, no. 22, 2003, pp. 1893–1899.

244. S. a. El-Safty, and T. Hanaokat. Microemulsion Liquid Crystal Templates for Highly Ordered Three-Dimensional Mesoporous Silica Monoliths with Controllable Mesopore Structures. *Chemistry of Materials*, vol. 16, no. 3, 2004, pp. 384–400.

245. S. Inagaki, Y. Fukushima, and K. Kuroda. Synthesis of Highly Ordered Mesoporous Materials from a Layered Polysilicate. *Chemical Communications*, no. 8, 1993, p. 680.

246. M. Kruk, and L. Cao. Pore Size Tailoring in Large-Pore SBA-15 Silica Synthesized in the Presence of Hexane. *Langmuir*, vol. 23, no. 13, 2007, pp. 7247–7254.

247. Z. A. Alothman. A Review: Fundamental Aspects of Silicate Mesoporous Materials. *Materials*, vol. 5, no. 12, 2012, pp. 2874–2902.

248. E. W. S. J. C. Vartuli, K. D. Schmitt, C. T. Kresge, W. J. Roth, M. E. Leonowicz, S. B. McCullen, S. D. Hellring, J. S. Beck, J. L. Schlenker, D. H. Olson. Effect of Surfactant / Silica Molar Ratios on the Formation of Mesoporous Molecular Sieves : Inorganic. *Chemistry of Materials*, vol. 6, 1994, pp. 2317–2326.

249. J. N. Israelachvili, D. J. Mitchell, and B. W. Ninham. Theory of Self-Assembly of Hydrocarbon Amphiphiles into Micelles and Bilayers. *Journal of the Chemical Society, Faraday Transactions 2: Molecular and Chemical Physics*, 1976, pp. 1525–1568.

250. D. J. Mitchell, and B. W. Ninham. Micelles, Vesicles and Microemulsions. *Journal of the Chemical Society, Faraday Transactions 2: Molecular and Chemical Physics*, vol. 77, no. 4, 1981, pp. 601–629.

251. C. J. Brinker, Y. F. Lu, A. Sellinger, and H. Y. Fan. Evaporation Induced Self-Assembly: Nanostructures Made Easy. *Advanced Materials*, vol. 11, no. 7, 1999, pp. 579–585.

252. Q. Huo, D. I. Margolese, U. Ciesla, P. Feng, T. E. Gier, P. Sieger, R. Leon, P. M. Petroff, F. Schüth, and G. D. Stucky. Generalized Synthesis of Periodic Surfactant/Inorganic Composite Materials. *Nature*, vol. 368, no. 6469, 1994, pp. 317–321.

253. D. Zhao, Q. Huo, J. Feng, B. F. Chmelka, and G. D. Stucky. Nonionic Triblock and Star Diblock Copolymer and Oligomeric Surfactant Syntheses of Highly Ordered, Hydrothermally Stable, Mesoporous Silica Structures. *J. Am. Chem. Soc.*, vol. 120, no. 24, 1998, pp. 6024–6036.

254. P. Schmidt-Winkel, P. Yang, D. I. Margolese, B. F. Chmelka, and G. D. Stucky. Fluoride-Induced Hierarchical Ordering of Mesoporous Silica in Aqueous Acid-Syntheses. *Advanced Materials*, vol. 11, no. 4, 1999, pp. 303–307.

255. P. T. Tanev, and T. J. Pinnavaia. Mesoporous Silica Molecular Sieves Prepared by Ionic and Neutral Surfactant Templating: A Comparison of Physical Properties. *Chemistry of Materials*, vol. 8, no. 8, 1996, pp. 2068–2079.

256. D. Zhao, J. Feng, Q. Huo, N. Melosh, G. H. Fredrickson, B. F. Chmelka, and G.

D. Stucky. Triblock Copolymer Syntheses of Mesoporous Silica with Periodic 50 to 300 Angstrom Pores. *Science*, vol. 279, no. 5350, 1998, pp. 548–552.

257. H. P. Lin, and C. Y. Mou. Structural and Morphological Control of Cationic Surfactant-Templated Mesoporous Silica. *Accounts of Chemical Research*, vol. 35, no. 11, 2002, pp. 927–935.

258. S. Hitz, and R. Prins. Influence of Template Extraction on Structure, Activity, and Stability of MCM-41 Catalysts. *Journal of Catalysis*, vol. 168, no. 2, 1997, pp. 194–206.

259. M. Imperor-Clerc, P. Davidson, and A. Davidson. Existence of a Microporous Corona around the Mesopores of Silica-Based SBA-15 Materials Templated by Triblock Copolymers. *Journal of the American Chemical Society*, vol. 122, no. 48, 2000, pp. 11925–11933.

260. A. Pitto-Barry, and N. P. E. Barry. Pluronic® Block-Copolymers in Medicine: From Chemical and Biological Versatility to Rationalisation and Clinical Advances. *Polymer Chemistry*, vol. 5, no. 10, 2014, pp. 3291–3297.

261. G. Wanka, H. Hoffmann, and W. Ulbricht. Phase Diagrams and Aggregation Behavior of Poly(Oxyethylene)-Poly(Oxypropylene)-Poly(Oxyethylene) Triblock Copolymers in Aqueous Solutions. *Macromolecules*, vol. 27, no. 15, 1994, pp. 4145–4159.

262. Y. Su, J. Wang, and H. Liu. Formation of a Hydrophobic Microenvironment in Aqueous PEO - PPO - PEO Block Copolymer Solutions Investigated by Fourier Transform Infrared Spectroscopy. *Journal of Physical Chemistry*, vol. 106, 2002, pp. 11823–11828.

263. C. Yu, B. Tian, J. Fan, G. D. Stucky, and D. Zhao. Salt Effect in the Synthesis of Mesoporous Silica Templated by Non-Ionic Block Copolymers. *Chemical Communications*, vol. 24, 2001, pp. 2726–2727.

264. X. Cui, W. C. Zin, W. J. Cho, and C. S. Ha. Nonionic Triblock Copolymer Synthesis of SBA-15 above the Isoelectric Point of Silica (PH = 2-5). *Materials Letters*, vol. 59, no. 18, 2005, pp. 2257–2261.

265. S. Ruthstein, J. Schmidt, E. Kesselman, Y. Talmon, and D. Goldfarb. Resolving Intermediate Solution Structures during the Formation of Mesoporous SBA-15.

Journal of the American Chemical Society, vol. 128, no. 10, 2006, pp. 3366–3374.

266. F. Bérubé, and S. Kaliaguine. Calcination and Thermal Degradation Mechanisms of Triblock Copolymer Template in SBA-15 Materials. *Microporous and Mesoporous Materials*, vol. 115, no. 3, 2008, pp. 469–479.

267. V. Malgras, Q. Ji, Y. Kamachi, T. Mori, F. K. Shieh, K. C. W. Wu, K. Ariga, and Y. Yamauchi. Templated Synthesis for Nanoarchitectured Porous Materials. *Bulletin of the Chemical Society of Japan*, vol. 88, no. 9, 2015, pp. 1171–1200.

268. B. Sakintuna, and Y. Yürüm. Templated Porous Carbons: A Review Article. *Industrial and Engineering Chemistry Research*, vol. 44, no. 9, 2005, pp. 2893–2902.

269. K. Miura, J. Hayashi, and K. Hashimoto. Production of Molecular Sieving Carbon through Carbonization of Coal Modified by Organic Additives. *Carbon*, vol. 29, nos. 4–5, 1991, pp. 653–660.

270. A. B. Fuertes, and T. A. Centeno. Carbon Molecular Sieve Membranes from Polyetherimide. *Microporous and Mesoporous Materials*, vol. 26, nos. 1–3, 1998, pp. 23–26.

271. F. Cheng, J. Liang, J. Zhao, Z. Tao, and J. Chen. Biomass Waste-Derived Microporous Carbons with Controlled Texture and Enhanced Hydrogen Uptake. *Chemistry of Materials*, vol. 20, no. 5, 2008, pp. 1889–1895.

272. T. Kyotani, Z. Ma, and A. Tomita. Template Synthesis of Novel Porous Carbons Using Various Types of Zeolites. *Carbons*, vol. 41, 2003, pp. 1451–1459.

273. T. Kyotani. Control of Pore Structure in Carbon. *Carbon*, vol. 38, no. 2, 2000, pp. 269–286.

274. R. Ryoo, S. H. Joo, and S. Jun. Synthesis of Highly Ordered Carbon Molecular Sieves via Template-Mediated Structural Transformation. *The Journal of Physical Chemistry B*, vol. 103, no. 37, 1999, pp. 7743–7746.

275. J. Lee, S. Yoon, T. Hyeon, M. Oh, K. Bum, S. M. Oh, and K. B. Kim. Synthesis of a New Mesoporous Carbon and Its Application to Electrochemical Double-Layer Capacitors. *Chemical Communications*, vol. 21, 1999, pp. 2177–2178.

276. J. Lee, S. Yoon, S. M. Oh, C. H. Shin, and T. Hyeon. Development of a New Mesoporous Carbon Using an HMS Aluminosilicate Template. *Advanced*

Materials, vol. 12, no. 5, 2000, pp. 359–362.

277. S. Jun, S. H. Joo, R. Ryoo, and M. Kruk. Synthesis of New, Nanoporous Carbon with Hexagonally Ordered Mesostructure. *J. Am. Chem. Soc.*, vol. 122, no. 43, 2000, pp. 10712–10713.

278. B. Tian, S. Che, Z. Liu, X. Liu, W. Fan, T. Tatsumi, O. Terasaki, and D. Zhao. Novel Approaches to Synthesize Self-Supported Ultrathin Carbon Nanowire Arrays Templated by MCM-41. *Chemical communications (Cambridge, England)*, no. 21, 2003, pp. 2726–2727.

279. Y. Xia, and R. Mokaya. Generalized and Facile Synthesis Approach to N-Doped Highly Graphitic Mesoporous Carbon Materials. *Chemistry of Materials*, vol. 17, no. 6, 2005, pp. 1553–1560.

280. T. W. Kim, R. Ryoo, K. P. Gierszal, M. Jaroniec, L. A. Solovyov, Y. Sakamoto, and O. Terasaki. Characterization of Mesoporous Carbons Synthesized with SBA-16 Silica Template. *Journal of Materials Chemistry*, vol. 15, no. 15, 2005, pp. 1560–1571.

281. A. Ampoumogli, G. Charalambopoulou, P. Javadian, B. Richter, T. R. Jensen, and T. Steriotis. Hydrogen Desorption and Cycling Properties of Composites Based on Mesoporous Carbons and a LiBH4–Ca(BH4)2 Eutectic Mixture. *Journal of Alloys and Compounds*, vol. 645, 2015, pp. S480–S484.

282. A. A. Zakhidov, R. H. Baughman, Z. Iqbal, C. Cui, I. Khayrullin, S. O. Dantas, J. Marti, and V. G. Ralchenko. Carbon Structures with Three-Dimensional Periodicity at Optical Wavelengths. *Science*, vol. 282, no. 5390, 1998, pp. 897–899.

283. S. A. Johnson, S. A. Johnson, P. J. Ollivier, and T. E. Mallouk. Ordered Mesoporous Polymers of Tunable Pore Size from Colloidal Silica Templates. vol. 963, no. 1999, 2014, pp. 10–13.

284. S. Zhang, L. Chen, S. Zhou, D. Zhao, and L. Wu. Facile Synthesis of Hierarchically Ordered Porous Carbon via in Situ Self-Assembly of Colloidal Polymer and Silica Spheres and Its Use as a Catalyst Support. *Chemistry of Materials*, vol. 22, no. 11, 2010, pp. 3433–3440.

285. J. Lee, J. Kim, and T. Hyeon. Recent Progress in the Synthesis of Porous Carbon

Materials. *Advanced Materials*, vol. 18, no. 16, 2006, pp. 2073–2094.

286. C. Liang, Z. Li, and S. Dai. Mesoporous Carbon Materials: Synthesis and Modification. *Angewandte Chemie - International Edition*, vol. 47, no. 20, 2008, pp. 3696–3717.

287. Z. Weishauptová, T. Suchý, and V. Machovič. Relation between Mechanical Properties and Pyrolysis Temperature of Phenol Formaldehyde Resin. *Ceramics - Silikaty*, vol. 56, no. 1, 2012, pp. 40–49.

288. S. T. Tso, and J. A. Pask. Reaction of Glasses with Hydrofluoric Acid Solution. *Journal of the American Ceramic Society*, vol. 65, no. 7, 1982, pp. 360–362.

289. S. A. Greenberg. The Depolymerization of Silica in Sodium Hydroxide Solutions. *Journal of Physical Chemistry*, vol. 61, no. 7, 1957, pp. 960–965.

290. C. Liang, K. Hong, G. A. Guiochon, J. W. Mays, and S. Dai. Synthesis of a Large-Scale Highly Ordered Porous Carbon Film by Self-Assembly of Block Copolymers. *Angewandte Chemie - International Edition*, vol. 43, 2004, pp. 5785–5789.

291. Y. Deng, T. Yu, Y. Wan, Y. Shi, Y. Meng, D. Gu, L. Zhang, Y. Huang, C. Liu, X. Wu, and D. Zhao. Ordered Mesoporous Silicas and Carbons with Large Accessible Pores Templated from Amphiphilic Diblock Copolymer Poly(Ethylene Oxide)-b-Polystyrene. *Journal of the American Chemical Society*, vol. 129, no. 6, 2007, pp. 1690–7.

292. Y. Fang, D. Gu, Y. Zou, Z. Wu, F. Li, R. Che, Y. Deng, B. Tu, and D. Zhao. A Low-Concentration Hydrothermal Synthesis of Biocompatible Ordered Mesoporous Carbon Nanospheres with Tunable and Uniform Size. *Angewandte Chemie - International Edition*, vol. 49, no. 43, 2010, pp. 7987–7991.

293. Y. Liang, R. Fu, and D. Wu. Reactive Template-Induced Self-Assembly to Ordered Mesoporous Polymeric and Carbonaceous Materials. *ACS nano*, vol. 7, no. 2, 2013, pp. 1748–54.

294. Y. Wan, Y. Shi, and D. Zhao. Designed Synthesis of Mesoporous Solids via Nonionic-Surfactant-Templating Approach. *Chemical communications (Cambridge, England)*, no. 9, 2007, pp. 897–926.

295. L. Song, D. Feng, N. J. Fredin, K. G. Yager, R. L. Jones, Q. Wu, D. Zhao, and B.

D. Vogt. Challenges in Fabrication of Mesoporous Carbon Films with Ordered Cylindrical. vol. 4, no. 1, 2010, pp. 189–198.

296. Y. Meng, D. Gu, F. Zhang, Y. Shi, L. Cheng, D. Feng, Z. Wu, Z. Chen, Y. Wan, A. Stein, D. Zhao, R. V April, V. Re, M. Recei, and V. July. A Family of Highly Ordered Mesoporous Polymer Resin and Carbon Structures from Organic - Organic Self-Assembly. *Chem. Mater.*, vol. 18, no. 4, 2006, pp. 4447–4464.

297. G. J. A. A. Soler-Illia, P. C. Angelomé, M. C. Fuertes, A. Calvo, A. Wolosiuk, A. Zelcer, M. G. Bellino, and E. D. Martínez. Mesoporous Hybrid and Nanocomposite Thin Films. A Sol-Gel Toolbox to Create Nanoconfined Systems with Localized Chemical Properties. *Journal of Sol-Gel Science and Technology*, vol. 57, no. 3, 2011, pp. 299–312.

298. T.-Y. Ma, L. Liu, and Z.-Y. Yuan. Direct Synthesis of Ordered Mesoporous Carbons. *Chem. Soc. Rev.*, vol. 42, no. 9, 2013, pp. 3977–4003.

299. P. Gao, A. Wang, X. Wang, and T. Zhang. Synthesis of Highly Ordered Ir-Containing Mesoporous Carbon Materials by Organic-Organic Self-Assembly. *Chemistry of Materials*, vol. 20, no. 5, 2008, pp. 1881–1888.

300. Y. Huang, H. Cai, D. Feng, D. Gu, Y. Deng, B. Tu, H. Wang, P. a Webley, and D. Zhao. One-Step Hydrothermal Synthesis of Ordered Mesostructured Carbonaceous Monoliths with Hierarchical Porosities. *Chemical communications*, 2008, pp. 2641–2643.

301. L. Liu, F. Y. Wang, G. S. Shao, and Z. Y. Yuan. A Low-Temperature Autoclaving Route to Synthesize Monolithic Carbon Materials with an Ordered Mesostructure. *Carbon*, vol. 48, no. 7, 2010, pp. 2089–2099.

302. R. Ryoo, and S. H. Joo. Nanostructured Carbon Materials Synthesized from Mesoporous Silica Crystals by Replication. *Studies in Surface Science and Catalysis*, vol. 148, 2004, pp. 241–260.

303. S. Jun, Sang Hoon Joo, R. Ryoo, M. Kruk, M. Jaroniec, Z. Liu, T. Ohsuna, and O. Terasaki. ..Synthesis of New, Nanoporous Carbon with Hexagonally Ordered Mesostructure. *Journal of the American Chemical Society*, vol. 122, no. 43, 2000, pp. 10712–10713.

304. S. Bernard, and P. Miele. Polymer-Derived Ordered Mesoporous Silicon-Boron-

Carbon-Nitrogen (Si/B/C/N) Ceramics. *Journal of Ceramic Science and Technology*, vol. 4, no. 2, 2013, pp. 113–122.

305. J. H. Lee, and S. J. Park. Abs Recent Advances in Preparations and Applications of Carbon Aerogels: A Review. *Carbon*, vol. 163, 2020, pp. 1–18.

306. L. Zuo, Y. Zhang, L. Zhang, Y. E. Miao, W. Fan, and T. Liu. Polymer/Carbon-Based Hybrid Aerogels: Preparation, Properties and Applications. *Materials*, vol. 8, no. 10, 2015, pp. 6806–6848.

307. R. W. Pekala. Organic Aerogels from the Polycondensation of Resorcinol with Formaldehyde. *Journal of materials science*, vol. 24, no. 9, 1989, pp. 3221–3227.

308. R. W. Pekala, C. T. Alviso, and J. D. LeMay. Organic Aerogels: Microstructural Dependence of Mechanical Properties in Compression. *Journal of Non-Crystalline Solids*, vol. 125, nos. 1–2, 1990, pp. 67–75.

309. N. H. N. Do, T. P. Luu, Q. B. Thai, D. K. Le, N. D. Q. Chau, S. T. Nguyen, P. K. Le, N. Phan-Thien, and H. M. Duong. Heat and Sound Insulation Applications of Pineapple Aerogels from Pineapple Waste. *Materials Chemistry and Physics*, vol. 242, 2020, p. 122267.

310. J. Feng, S. T. Nguyen, Z. Fan, and H. M. Duong. Advanced Fabrication and Oil Absorption Properties of Super-Hydrophobic Recycled Cellulose Aerogels. *Chemical Engineering Journal*, vol. 270, 2015, pp. 168–175.

311. R. J. White, N. Brun, V. L. Budarin, J. H. Clark, and M. M. Titirici. Always Look on the “Light” Side of Life: Sustainable Carbon Aerogels. *ChemSusChem*, vol. 7, no. 3, 2014, pp. 670–689.

312. S. A. Al-muhtaseb, and J. A. Ritter. Preparation and Properties of Resorcinol-Formaldehyde Organic and Carbon Gels. *Advanced Materials*, vol. 15, no. 2, 2003, pp. 101–114.

313. T. Li, M. Cao, J. Liang, X. Xie, and G. Du. Mechanism of Base-Catalyzed Resorcinol-Formaldehyde and Phenol-Resorcinol-Formaldehyde Condensation Reactions: A Theoretical Study. *Polymers*, vol. 9, no. 9, 2017, p. 426.

314. L. Hu, R. He, H. Lei, and D. Fang. Carbon Aerogel for Insulation Applications: A Review. *International Journal of Thermophysics*, vol. 40, no. 4, 2019, pp. 1–25.

315. D. Wu, R. Fu, S. Zhang, M. S. Dresselhaus, and G. Dresselhaus. Preparation of

Low-Density Carbon Aerogels by Ambient Pressure Drying. *Carbon*, vol. 42, no. 10, 2004, pp. 2033–2039.

316. N. Liu, S. Zhang, R. Fu, M. S. Dresselhaus, and G. Dresselhaus. Carbon Aerogel Spheres Prepared via Alcohol Supercritical Drying. *Carbon*, vol. 44, no. 12, 2006, pp. 2430–2436.

317. H. Tamon, H. Ishizaka, T. Yamamoto, and T. Suzuki. Preparation of Mesoporous Carbon by Freeze Drying. *Carbon*, vol. 37, no. 12, 1999, pp. 2049–2055.

318. U. Fischer, R. Saliger, V. Bock, R. Petricevic, and J. Fricke. Carbon Aerogel as Electrode Material in Supercapacitors. *Journal of Porous Materials*, vol. 4, 1997, pp. 281–285.

319. M. Aghabararpour, M. Naderi, S. Motahari, and M. Najafi. A Study on Resorcinol Formaldehyde Carbon Aerogel/Epoxy Nanocomposites: The Effect of Carbon Aerogel Pyrolysis Time. *Journal of Polymer Research*, vol. 26, no. 59, 2019, pp. 1–8.

320. G. Le Caër, P. Delcroix, S. Bégin-Colin, and T. Ziller. High-Energy Ball-Milling of Alloys and Compounds. *Hyperfine Interactions*, vols. 141–142, nos. 1–4, 2002, pp. 63–72.

321. A. Zolriasatein, A. Shokuhfar, F. Safari, and N. Abdi. Comparative Study of SPEX and Planetary Milling Methods for the Fabrication of Complex Metallic Alloy Nanoparticles. *Micro & Nano Letters*, vol. 13, no. 4, 2018, pp. 448–451.

322. E. Roedern, B. R. S. Hansen, M. B. Ley, and T. R. Jensen. Supp Effect of Eutectic Melting, Reactive Hydride Composites, and Nanoconfinement on Decomposition and Reversibility of LiBH4-KBH4. *Journal of Physical Chemistry C*, vol. 119, no. 46, 2015, pp. 25818–25825.

323. QuantachromeCorp. Quantachrome Instruments Gas Sorption Show. https://www.youtube.com/watch?v=sqGJsIVCvq8.

324. M. Thommes, K. Kaneko, A. V. Neimark, J. P. Olivier, F. Rodriguez-Reinoso, J. Rouquerol, and K. S. W. Sing. Physisorption of Gases, with Special Reference to the Evaluation of Surface Area and Pore Size Distribution (IUPAC Technical Report). *Pure and Applied Chemistry*, vol. 87, nos. 9–10, 2015, pp. 1051–1069.

325. S. Lowell, and J. E. Shields. *Powder Surface Area and Porosity*. Springer

Netherlands, Dordrecht, 1984.

326. A. Ampoumogli. *Development, Characterization and Evaluation of Porous Composite Materials for Hydrogen Storage*. University of Crete, 2017.

327. Y. Liu, D. Reed, C. Paterakis, L. Contreras, M. Baricco, and D. Book. Study of the Decomposition of a 0.62LiBH4–0.38NaBH4 Mixture. *International Journal of Hydrogen Energy*, vol. 42, no. 35, 2017, pp. 22480–22488.

328. T. D. Humphries, G. N. Kalantzopoulos, I. Llamas-Jansa, J. E. Olsen, and B. C. Hauback. Reversible Hydrogenation Studies of NaBH4 Milled with Ni-Containing Additives. *Journal of Physical Chemistry C*, vol. 117, no. 12, 2013, pp. 6060–6065.

329. J. Mao, and D. H. Gregory. Recent Advances in the Use of Sodium Borohydride as a Solid State Hydrogen Store. *Energies*, vol. 8, 2015, pp. 430–453.

330. P. A. Orłowski, and W. Grochala. Effect of Vanadium Catalysts on Hydrogen Evolution from NaBH4. *Solids*, vol. 3, no. 2, 2022, pp. 295–310.

331. J. Mao, Z. Guo, I. P. Nevirkovets, H. K. Liu, and S. X. Dou. Hydrogen De-/Absorption Improvement of NaBH 4 Catalyzed by Titanium-Based Additives. *Journal of Physical Chemistry C*, vol. 116, no. 1, 2012, pp. 1596–1604.

332. S. I. Orimo, Y. Nakamori, N. Ohba, K. Miwa, M. Aoki, S. I. Towata, and A. Züttel. Experimental Studies on Intermediate Compound of LiBH4. *Applied Physics Letters*, vol. 89, no. 2, 2006, pp. 87–90.

333. D. Reed, and D. Book. In-Situ Raman Study of the Thermal Decomposition of LiBH4. *Mater. Res. Soc. Symp. Proc.*, vol. 1216, 2010, pp. 2–8.

334. A. Ampoumogli, T. Steriotis, P. Trikalitis, D. Giasafaki, E. G. Bardaji, M. Fichtner, and G. Charalambopoulou. Nanostructured Composites of Mesoporous Carbons and Boranates as Hydrogen Storage Materials. *Journal of Alloys and Compounds*, vol. 509, no. 2, 2011, pp. S705–S708.

335. K. Hoang, and C. G. Van De Walle. Mechanism for the Decomposition of Lithium Borohydride. *International Journal of Hydrogen Energy*, vol. 37, no. 7, 2012, pp. 5825–5832.

336. O. Friedrichs, A. Remhof, S. J. Hwang, and A. Zuttel. Role of Li2B12H12 for the Formation and Decomposition of LiBH4. *Chem. Mater.*, vol. 22, no. 10, 2010, pp.

3265–3268.

337. S. Hwang, R. C. Bowman, J. J. W. Reiter, J. Rijssenbeek, G. L. Soloveichik, J. Zhao, H. Kabbour, and C. C. Ahn. NMR Confirmation for Formation of [B12H12]2- Complexes during Hydrogen Desorption from Metal Borohydrides. *J. Phys. Chem. C*, vol. 112, no. 9, 2008, pp. 3164–3169.

338. A. Surrey, C. Bonatto Minella, N. Fechler, M. Antonietti, H. Grafe, and L. Schultz. Improved Hydrogen Storage Properties of LiBH4 via Nanoconfinement in Micro- and Mesoporous Aerogel-like Carbon. *International Journal of Hydrogen Energy*, vol. 41, no. 12, 2016, pp. 5540–5548.

339. X. Liu, D. Peaslee, C. Z. Jost, T. F. Baumann, and E. H. Majzoub. Systematic Pore-Size Effects of Nanoconfinement of LiBH4: Elimination of Diborane Release and Tunable Behavior for Hydrogen Storage Applications. *Chemistry of Materials*, vol. 23, no. 5, 2011, pp. 1331–1336.